AFGL-TR-84-0116

INVESTIGATIONS OF HIGH RESOLUTION IMAGING THROUGH THE EARTH'S ATMOSPHERE USING SPECKLE INTERFEROMETRY

E. K. Hege
P. A. Strittmatter
N. J. Woolf

Steward Observatory
University of Arizona
Tucson, AZ 85721

Final Report
1 February 1982 - 31 January 1984

7 March 1984

Approved for public release; distribution unlimited

AIR FORCE GEOPHYSICS LABORATORY
AIR FORCE SYSTEMS COMMAND
UNITED STATES AIR FORCE
HANSCOM AFB, MASSACHUSETTS 01731

This report has been reviewed by the ESD Public Affairs Office (PA) and is releasable to the National Technical Information Service (NTIS).

The technical report has been reviewed and is approved for publication.

Richard R. Radick
Contract Manager

S.L. Keil
Branch Chief

FOR THE COMMANDER

R.C. Sagalyn
Division Director

Qualified requestors may obtain additional copies from the Defense Technical Information Center. All others should apply to the National Technical Information Service.

If your address has changed, or if you wish to be removed from the mailing list, or if the addressee is no longer employed by your organization, please notify AFGL/DAA, Hanscom AFB, MA 01731. This will assist us in maintaining a current mailing list.

Do not return copies of this report unless contractual obligations or notices on a specific document require that it be returned.

REPORT DOCUMENTATION PAGE

1a. REPORT SECURITY CLASSIFICATION: Unclassified	1b. RESTRICTIVE MARKINGS
2a. SECURITY CLASSIFICATION AUTHORITY	3. DISTRIBUTION/AVAILABILITY OF REPORT: Approved for public release; distribution unlimited
2b. DECLASSIFICATION/DOWNGRADING SCHEDULE	
4. PERFORMING ORGANIZATION REPORT NUMBER(S)	5. MONITORING ORGANIZATION REPORT NUMBER(S): AFGL-TR-84-0116
6a. NAME OF PERFORMING ORGANIZATION: Steward Observatory; 6b. OFFICE SYMBOL (If applicable)	7a. NAME OF MONITORING ORGANIZATION: Air Force Geophysics Laboratory
6c. ADDRESS (City, State and ZIP Code): University of Arizona, Tucson, AZ 85721	7b. ADDRESS (City, State and ZIP Code): Hanscom AFB, Massachusetts 01731, Monitor/R.R.Radick/PHS
8a. NAME OF FUNDING/SPONSORING ORGANIZATION; 8b. OFFICE SYMBOL (If applicable)	9. PROCUREMENT INSTRUMENT IDENTIFICATION NUMBER: F19628-82-K-0025
8c. ADDRESS (City, State and ZIP Code)	10. SOURCE OF FUNDING NOS.

PROGRAM ELEMENT NO.	PROJECT NO.	TASK NO.	WORK UNIT NO.
61102F	2311	G3	CH

11. TITLE (Include Security Classification): (Over)

12. PERSONAL AUTHOR(S): E.K. Hege, P.A.Strittmatter, and N.J. Woolf

13a. TYPE OF REPORT	13b. TIME COVERED	14. DATE OF REPORT (Yr., Mo., Day)	15. PAGE COUNT
Final Report	FROM 1 Feb 82 TO 31 Jan 84	7 March 1984	123

16. SUPPLEMENTARY NOTATION: (from back)

17. COSATI CODES		
FIELD	GROUP	SUB. GR.

18. SUBJECT TERMS (Continue on reverse if necessary and identify by block number): Speckle Interferometry, Image Reconstruction, Optical Interferometry, Phased Optical Arrays, MMT, Diffraction Limited Imaging, Speckle Imaging.

19. ABSTRACT (Continue on reverse if necessary and identify by block number)

Speckle interferometry is a post-detection image processing technique for producing diffraction limited image data using large astronomical telescopes in the presence of Earth's turbulent atmosphere which otherwise limits the imaging resolution. The Steward Observatory digital video speckle interferometry system consists of subsystems for a) video digitization of intensified, magnified, focal-plane images, b) Fourier transform (or autocorrelation) signal processing, and c) image analysis to produce the final interpreted results. Speckle interferometry has now been shown capable of yielding diffraction images for objects as faint as visual magnitude 16.

20. DISTRIBUTION/AVAILABILITY OF ABSTRACT	21. ABSTRACT SECURITY CLASSIFICATION
UNCLASSIFIED/UNLIMITED ☒ SAME AS RPT. ☒ DTIC USERS ☐	Unclassified

22a. NAME OF RESPONSIBLE INDIVIDUAL	22b. TELEPHONE NUMBER (Include Area Code)	22c. OFFICE SYMBOL
R.R.Radick		PHS

DD FORM 1473, 83 APR — EDITION OF 1 JAN 73 IS OBSOLETE.

Block 11 (Contd)

Investigations of High Resolution Imaging Through the Earth's Atmosphere Using Speckle Interferometry

Block 19 (Contd)

Objectives of present developments are to improve a) the resolution (by using the Multiple Mirror Telescope with its 6.9m optical aperture), b)the accuracy of the derived results (by implementing better photon detection and recording devices), and c) the efficiency and speed of the reduction algorithms which extract the information (by means of high-speed digital signal-processing hardware).

Experience gained with the present systems has shown the need for a) improved detectors (to provide better spatial resolution, geometric fidelity, quantum efficiency and dynamic range), b) real-time signal processing (to permit the primary data compression to be accomplished at the telescope while the observations progress), and c) image processing systems (to efficiently reduce the speckle interferometric results).

The work includes a growing effort in speckle image reconstruction using a combination of amplitude processing, various phase retrieval methods, holographic methods, and shift-and-add methods. The techniques have been applied to observations of Earth-orbiting satellites, asteroids, Pluto/Charon, binary stars, bright supergiant stars, active galactic nuclei, and quasi-stellar objects (QSOs). The results of the analysis of these observations have revealed both the capabilities and the limitations of the present systems.

Among the demonstrated capabilities are a) observations of structure as faint as m_v=19 in an m_v=16 system, b) observations of structure at the diffraction limit of the Multiple Mirror Telescope, c) astrometric observations, d) mapping of faint envelopes around bright supergiants, and e) measurements of sizes of Earth-orbiting satellites.

Among limitations of this system, the most severe by far is the extremely limited signal processing throughput, in which the primary signal processing time ranges up to 100 times that required for the observations at the telescope, and lack of a general purpose array processing capability for image analysis. The next most severe problem is lack of a suitable low distortion, high quantum efficiency, high resolution detector.

For future applications of this technique, larger optical baselines will be required. We have studied some possibilities for both ground-based and space-deployed arrays with optical baselines of 100 meters.

TABLE OF CONTENTS

1. INTRODUCTION

During the past several years there has been a rapid development in techniques for achieving high resolution imaging through the earth's atmosphere using large ground based telescopes. Especially promising among these techniques is that of speckle interferometry with which spatial resolution gains of $\sim 10^2$ over that normally permitted by the earth's atmosphere have been demonstrated. The technique has been demonstrated to work on both artificial satellites and celestial objects. It has furthermore been applied to rather faint sources ($m_v > 16$). Speckle interferometry thus has considerable potential application both to military and astronomical targets.

1.1 Speckle Interferometry at Steward Observatory

Speckle interferometry (Labeyrie 1970, 1978) is a post-detection image processing technique for producing diffraction limited images using large astronomical telescopes in the presence of Earth's turbulent atmosphere which otherwise limits the imaging resolution. The Steward Observatory digital video speckle interferometry system (Hubbard et al. 1979, Hege et al. 1980, Hege et al 1982a) consists of three basic subsystems: a) video digitization of an intensified, magnified, focal-plane image; b) Fourier transform (or vector autocorrelation) signal processing; and c) image analysis to produce the final interpreted results. Speckle interferometry has now been shown capable of yielding diffraction limited information (including images) on objects as faint as visual magnitude 16.

Developments in progress at Steward Observatory are aimed at improving a) the resolution, (by using the Multiple Mirror Telescope with its 6.9m optical aperture), b) the accuracy of the derived results (by implementing better photon detection and recording devices) and c) the efficiency and speed of the reduction algorithms which extract the information (by means of high-speed digital signal-processing hardware).

Experience gained with the present systems has shown the need for a) improved detectors (to provide better spatial resolution and geometric fidelity as well as better quantum efficiency, linearity, and dynamic range), b) real-time signal processing (to permit the primary data compression to be accomplished at the telescope while the observations progress), and c) image processing systems (to efficiently reduce the speckle interferometric results).

A number of Steward Observatory scientists are involved in high angular resolution studies using speckle interferometry in both optical and infrared. The work also includes a growing effort in speckle image reconstruction using a combination of amplitude processing (Fienup 1980), various phase retrieval methods (Knox and Thompson 1974, Cocke 1980, Walker 1982,

Nisenson and Papaliolios 1983), holographic methods (Weigelt 1978, Beckers et al. 1982, 1983a, Christou (1983) and shift-and-add methods (Bates and Cady 1980, Bagnuolo 1982). This work is presently done using the very limited capabilities of a Grinnell digital video memory system for video digitization and the observatory minicomputers (Data General Nova and Eclipse class) for both the signal processing and the image processing functions. Nevertheless, the techniques have been applied successfully to observations of asteroids (body axes and pole determination, Drummond et al. 1984), the Pluto-Charon system (an observation near minimum separation leading to refinement of the orbit, Hege et al. 1982b), and the $15^m.7$ QSO PG1115+080 (the resolution of component A into two nearly equal, unresolved - $<0''.1$ - components) as well as to observations of bright supergiants (images of Alpha Orionis in H and CaII, Goldberg et al. 1982, images of H envelopes around Alpha Herculis and Alpha Orionis, Beckers, et al. 1983b, speckle spectroscopic observations of Alpha Tauri showing a larger diameter in a TiO band, Freeman (1984) and binary stars (resolution of the orientation of and relative magnitudes of Capella, Bagnuolo (1984). These observations and results have revealed both the capabilities of the techniques and the limitations of the present systems.

Among the demonstrated capabilities are included a) observations of structure as faint as $m_v = 19$ in an $m_v = 16$ system, b) observations of structure at the diffraction limit of the Multiple Mirror Telescope, c) astrometric observations, d) mapping of faint envelopes around bright supergiants, and e) measurements of sizes of Earth orbiting satellites.

Among limitations of this system, the most severe by far are the extremely limited signal processing throughput, in which the primary signal processing time ranges up to 100 times that required for the observations at the telescope, and lack of a general purpose array processing capability for image analysis. We anticipate upgrading of observatory computational capabilities to include array-processing image analysis systems.

1.2 Speckle Interferometry Signal Processing

Labeyrie first pointed out that the short exposure images of the seeing perturbed telescope image contained information on the structure of the source up to resolutions corresponding to the diffraction limit of the telescope. In classical speckle interferometry, the short exposure images (specklegrams) are recorded and then processed to yield the autocorrelation (AC) or power spectrum (PS) of the object. Thus the n^{th} specklegram $i_n(x,y)$ of the object is

$$i_n(x,y) = o(x,y) * p_n(x,y) \qquad (1.1)$$

where $p_n(x,y)$ is the point-spread function of the atmosphere plus instrument for the n^{th} specklegram. Taking Fourier transforms of

many specklegrams and averaging thus yields

$$\langle |I_n(u,v)|^2 \rangle = |O(u,v)|^2 \langle |P_n(u,v)|^2 \rangle \qquad (1.2)$$

which may be inverted to yield the power spectrum of the object $PS_o = |O(u,v)|^2$ for those spatial frequencies for which $\langle |P_n(u,v)|^2 \rangle$ is non-zero. In normal circumstances $\langle |P_n(u,v)|^2 \rangle$ is non-zero to the diffraction limit of the telescope and is determined by making interspersed observations of a point source calibrator. This much is common to all speckle techniques, and in a sense represents the ideal case. In practice many other corrections, depending upon detector and observing conditions, are required: examples are correction of geometric distortion, removal of sampling bias, etc.

A calibrated speckle interferometric observation requires

(i) integration of individual frame power spectra, $\langle |I_n(u,v)|^2 \rangle$, defined by 1.2; or equivalently integration of individual frame autocorrelation functions.

(ii) standardization of each observation with corresponding measurements of an unresolved point source, $\langle |I_{on}(u,v)|^2 \rangle$, suitably interspersed to accurately sample variable seeing conditions.

(iii) measurement of the detector transfer function $|D(u,v)|^2$.

The resulting object power spectrum can then be estimated by computing (see Hege, et al. 1982a or AFGL-TR-82-0136, p. 24)

$$|O(u,v)|^2 = \frac{\{\langle |I_n(u,v)|^2 \rangle / |D(u,v)|^2 - N\}}{\{\langle |I_{on}(u,v)|^2 / |D(u,v)|^2 - N_o\}} \qquad (1.3)$$

where N and N_o are the noise bias associated with the object and standard power spectra, respectively produced by the image sampling process. The detector transfer funtion (DTF) is measured by integrating the individual frame power spectra for random events detected subsequent to illumination of the detector with uniform, low intensity light.

The present detector system is an intensified plumbicon camera with both analogue and photon counting modes. It is in regular use at the 2.3m and KPNO 4m telescopes and at the MMT. It produces digitized (8 bit), frame subtracted (to supress detector lag), data at standard video rates corresponding to approximately 60Mbits/sec at full resolution (sufficient to sample the diffraction limit of the MMT over a reasonable field of view). Our present system cannot accommodate this rate

digitally but uses a video recorder to archive data at a duty cycle of unity at the telescope on objects of all brightnesses. In this mode several (at least 2) passes of the video tape are required to capture all of the data digitally on 9-track magtape for subsequent reduction. For fainter objects, a photon counting mode has been implemented which allows photon addresses to be recorded digitally in real time at the telescope at rates of up to about 500 photons/frame corresponding to 0.5 Mbits/sec.

In order to properly calibrate for the usually variable seeing conditions, switching between object and calibrator is carried out as frequently as practical (about 1 minute intervals). The primary reduction thus consists of summed PSs or ACs of about 10^3 frames alternately for object and calibrator for as long as required to attain the necessary S/N. Corrections for detector distortion must be carried out on each frame prior to autocorrelation or power spectrum calculation; rejection of frames because of anomalously poor seeing or pointing errors can be done at the same time. Bias corrections must be carried out subsequently. All of this takes from 10 to 100 times longer than the original observation for reduction in our present systems.

The resultant AC or PS files are then ready for further analysis, usually a model fitting procedure analogous to that carried out with VLBI data in the early development of that technique. These procedures are also iterative and therefore computationally intensive.

1.3 Scientific Investigations with Speckle Interferometry

At Steward Observatory these techniques are being used by Beckers, Cocke, Drummond, Hege, Strittmatter and Woolf at optical wavelengths on a wide variety of astronomical problems. Work in progress presently includes:

i) Asteroids. Numerous measurements have been made of the instantaneous projected dimensions of asteroids in the brightness range 8^m to 13^m. More recently a systematic study of asteroids showing short term, large amplitude, periodic (about 6 hr) light variations has been undertaken. The data are modeled with an appropriately illuminated (terminator corresponding to solar phase angle) triaxial ellipsoid. A sequence of observations distributed through the rotation period is analysed to derive the dimensions of the asteroid and the direction of its spin axis in space. Results for the asteroid Eros are now in press. They took more than a year to produce owing to the high degree of processing required and the inadequacy of our present minicomputers to the task. Data on several other asteroids, including Pallas, Herculina and Metis, await analysis.

ii) Pluto/Charon. A series of observations has been carried out on this 14^m system with a view to improving the determination of the orbital parameters, to investigate evidence for albedo variegation, and to provide direct measurements of the diameter,

brightness and albedo of the planet and satellite. First results appeared in Icarus (Hege et al. 1982b) but considerable quantities of further data are in the process of reduction and analysis.

iii) Red Supergiants. Standard speckle observations have been carried out in a number of different passbands on α Ori, α Sco, o Cet, α Her, 119 Tau, α Tau and others (including some one-dimensional observations using the full 6.9m resolution in a two-mirror MMT configuration). The KPNO 4m data on α Ori have been partially reduced and show evidence of extended structure in the light of H_α and CaII 845.2nm out to about .25 arc seconds (10 stellar radii). Tentative evidence for similar structure, albeit at much lower relative intensity, has been obtained in certain continuum bands. A more detailed interpretation of these results awaits reduction of the remaining data for both the above passbands and for several others corresponding to different atomic or molecular transitions.

iv) The Triple (quintuple?) QSO. Observations of the triple QSO 1115+08 have been made, using a single 1.8m mirror of the MMT under nearly ideal (0.6 arcseconds seeing) conditions. The results (Hege et al. 1981) clearly demonstrated that the 16^m brightest component consists of two components, unresolved at the limit of the aperture, with a separation of 0.54 arcseconds. This work also showed the speckle holographic effect in the A-C and A-B cross correlations, namely the presence of direct images of the bright component at positions corresponding to cross correlation with the fainter 18^m and 19^m components.

v) Earth Orbiting Satellites. A measurement in one-dimension, using the B-E mirror pair of the Multiple Mirror Telescope, of FLTSATCOM1 yielded a diameter, at that arbitrarily chosen (verticle) position angle, of 4.9 ± 2.0 meters for that synchronous orbit object.

The above sample of observational programs gives some indication of the range of high angular resolution measurements that are being addressed with speckle interferometry and of the computational problems associated therewith.

1.4 Speckle Image Reconstruction

Under this contract, and in a related Air Force project AFOSR-82-0020, we conducted a program of high angular resolution imaging using the techniques of speckle interferometry and image reconstruction. We produced deconvolved (by aperture point spread function) image data for bright binaries, phaseless (by Fienup method) image reconstructions of an earth-approaching asteoid (Eros) and of a resolved supergiant (Betelgeuse), and differential image reconstructions (essentially holographic deconvolutions) of the atmospheres surrounding nearby red supergiant stars. We evaluated, by comparisons using real astronomical data, several methods for diffraction limited recon-

struction of speckle image data including both the blind deconvolution methods of Fienup and of Bates; the phase retrieval method of Knox and Thompson as applied to both bright and faint object observations; and various variations on shift-and-add methods, as well as appropriate combinations of two or more of these methods.

The limitation to power spectrum information is in some applications a serious one; direct image information is clearly preferable. For this purpose it is necessary to obtain both the phase and the amplitude of the Fourier components. Among the variety of techniques which hold promise is the Fienup (1979) technique which seeks to derive phase information from the Fourier amplitudes alone. Direct phase information can, however, be obtained from individual specklegrams using the Knox-Thompson (1974) algorithm (or variations thereon) or by the image plane shift-and-add techniques (again including many variations) developed by Hunt et al. (1982) and Bates and Fright (1983) Lynds, Worden and Harvey (1976). These methods do not produce accurate images, as the results are superimposed upon a broad "seeing" background. Nevertheless, they provide phase information for either direct use or for input to the Fienup (1980) or related: (i.e. Bates and Fright 1983 or Walker 1982) procedures.

All of these methods, however, require substantial computation in addition to the AC (PS) calculations described above. For this reason little has been achieved in practice, although trial computations on α Ori and the earth-approaching asteroid Eros, have been most encouraging. A high-speed, digital FFT, signal processing system would permit very significant advances to be made with these techniques.

A new speckle interferometric method was developed by Beckers (1982) and Hege (- also supported by NSF AST-8113212) and represents a variation on the holographic technique originally proposed by Weigelt (1978). With this differential speckle interferometer, the source is measured simultaneously at adjacent wavelengths, both in the continuum and in an atomic or molecular transition. In certain cases the object is (nearly) unresolved at one wavelength but extended at the other (e.g. the envelopes of red supergiants or the nucleus of a Seyfert such as NGC 1068 in the continuum vs in the lines). Direct frame by frame deconvolution (with appropriate Wiener filtering) then yields an image transform. The method is again computer intensive and its application has likewise been limited by the low throughput of our existing system.

1.5 Infrared Speckle Interferometry

We note also that a very active program of IR speckle interferometry is being carried out at Steward Observatory by D. W. McCarthy (1982a). The basic problem is similar to optical work, but for the moment is carried out using a single detector, scanning the image across a focal plane slit. While the number

of resolution elements is smaller at these longer wavelengths, and demands on computer capacity are less, this program nonetheless would also benefit from enhanced computational capabilities, especially in its image reconstruction aspects.

Among the scientific achievements of that program are i) detection of numerous very cool companions to nearby stars, ii) successful analysis of the IR structure in the nucleus of NGC 1068, and iii) successful image reconstruction of the Becklin Neugebauer object.

1.6 The Multiple Mirror Telescope

The recent successful co-phasing of all six optical beams of the MMT gives the University of Arizona the highest resolution imaging telescope in the world with an effective aperture of 6.86m. The closest competitor is the 6m telescope in the USSR. Although the MMT aperture (pupil) is not completely filled, the complex Fourier transform of the image does contain image amplitude and phase informaion (albeit not uniformly) for all frequencies transmitted by a 6.86 m aperture.

1.7 Background to the Steward Observatory Air Force Work

The following brief history of the University of Arizona speckle interferometry project and related work is presented to emphasize the nature and context of this research.

In 1976, the University of Arizona began a program (AFGL Contract F19628-77-C-0063) to develop image reconstruction techniques for large telescopes. Upon initial successes (AFGL-TR-78-1067) the contract was renewed (AFGL F19628-78-C-0058) during which diffraction limited image data were obtained for an Earth orbiting satellite (Space Division Report SD-TR-82-46) and diffraction limited images of astronomical objects were produced (AFGL-TR-82-0136). Methods for producing diffraction limited images were reviewed in Space Division Report SD-TR-82-45.

The success of that work led to the present AFGL contract F19628-82-K-0025 to continue our investigations of high resolution speckle imaging techniques through the Earth's atmosphere. In particular, we have now investigated the ultility of the 6.86m aperture provided by the Multiple Mirror Telescope for high angular resolution imaging work and for application to problems of space object identification. We have, so far demonstrated (a) MMT speckle interferometry on celestial objects, (b) the ability to track earth orbiting satellites, and (c) two-beam measurements (diameters) of synchronous orbit satellites. We have recently acquired data on celestial objects using all six beams simultaneously co-phased. We expect ultimately to produce a diffraction limited image of a synchronous orbit satellite such as FLTSATCOM or TDRSS. This work also has direct value in assessing the advantages/problems etc. of future very high resolution dilute aperture systems.

2. THE PROPOSED WORK

In this project we continued, for two further years, the image reconstruction programs being carried out under USAF auspices at Steward Observatory. The principal goals of the program were, to

(i) demonstrate use of the MMT for full speckle interferometry applications; the MMT offers the highest spatial resolution capability for the lowest cost of any telescope in the world.

(ii) upgrade the instrumentation so that on-line reduction capability can be demonstrated; this rapid evaluation of results is especially important for USAF application and is necessary for fine-tuning the phasing of the MMT. A design study for an on-line, full-frame, real-time data reduction system is included.

(iii) develop the reduction and analysis algorithms necessary to carry out image modelling and/or reconstruction from the recorded speckle data.

(iv) carry out observing programs designed to evaluate the above developments, to provide size and shape data on a modest number of artificial satellites and to derive structural information on various classes of astronomical objects including asteroids, stars, galactic nuclei and QSOs.

The work was carried out using the facilities of Steward Observatory (SO), the Multiple Mirror Telescope Observatory (MMTO), and the Kitt Peak National Observatory (KPNO) 4m telescope.

2.1 The Starting Point.

During the previous contract periods, substantial progress had been achieved in all aspects of the program. With support from USAF/AFGL and in collaboration with AF scientists at the Sacramento Peak Observatory, we had

(i) improved the SO/AFGL speckle camera for use at any conventional telescope by provision of micro-processor controlled Risley prisms, shutter mechanisms, etc.

(ii) developed a video camera detector system for data acquisition, having essentially 100 percent duty cycle and 512 x 256 pixel interlaced field. The data are recorded on a video cassette recorder (VCR).

(iii) implemented a data reduction system at the SO computer center which provides digital records of the data either from direct A/D conversions from the video tapes (the analogue mode) or by threshholding (the photon counting mode). In the latter mode, successive frames are subtracted so that only new events

are recorded.

(iv) analysed the instrumental response function of the system and demonstrated that substantial gains could be made by implementation of a true event centroiding mode. A preliminary design of the necessary logic hardware had been completed.

(v) developed improved data reduction programs to remove the effects of detector sampling (DTF) in the derived auto-correlation functions or power spectra. This step had resulted in a substantial improvement in our ability to derive unambiguous information on source structure.

(vi) carried out studies of seeing at the MMT which demonstrated that substantial improvements in effective seeing could be made by removing the low spatial frequency distortions (tilts) across the individual 1.8m apertures. This finding (partial wave front correction) has considerable potential impact on speckle (and other) interferometry with large telescopes and/or baselines in that it should significantly enhance the high spatial frequency MTF of the system.

(vii) demonstrated at the 2.3m telescope and the MMT that artificial satellites can be tracked to sufficient accuracy. Speckle interferometric measurements of a high altitude Russian communication satellite (Molniya type) were made and yielded useful size and shape data even though the resolution was near the intrinsic limit of the 2.3m telescope (~ 0.05 arcsec). These results had demonstrated the potential use of larger (higher resolution) ground based telescopes for military purposes.

(viii) began a series of scientific observations using speckle interferometry at the 2.3 and 4 meter telescopes and, finally, the MMT. Preliminary results had been obtained for a wide range of objects of astronomical and Air Force interest.

(ix) started a project to develop and implement methods for image reconstruction. Some success had been achieved for binary stars using the Cocke phase unwrapping technique, the Fienup method and direct deconvolution approaches (Knox-Thompson).

2.2 The Project Objectives.

Parallel programs of instrumental improvements and developments of image reconstruction methods were required. Our efforts concentrated on implementation of a final MMT coherent beam combiner and an MMT optimized speckle camera, improvements in the geometrical and efficiency properties of the detector system, and the provision of faster and more flexible reduction and analysis systems.

2.2.1 MMT Beam Combiner

Experiments conducted during the previous contract periods indicated that

(i) the Lagrange conditions must be adequately satisfied. This implies beam combination with errors in reduced aperture placements no more than 1 percent and path length equalization to better than that given by the coherence length (i.e. ~ 5μm in some applications).

(ii) independent adjustments must be provided to optimize individual parameters (focus, tilt, path length and aperture projection).

(iii) the final instrument must be polarization neutral. I.e. the combination of telescope plus instrument must produce no net polarization.

(iv) light losses must be minimized since observing time to achieve a given signal to noise depends quadratically on the net DQE.

(v) wavefront tilt correction should be incorporated. Beams produced by the individual 1.8m sub-apertures should produce images which overlap essentially all the time.

These conditions should be met in such a way that a speckle camera can be attached to the present MMT focal plane. Light from the object should pass through the MMT Top Box TV Coalignment System to permit wavefront tilt correction to be carried out in real time with field stars (correction time ~ Ø.5s m_v ~ 17m). The adjustment optics should be reflecting to minimize losses. The entire unit should be an additional module to be inserted in, and compatible with, the existing MMT Top Box.

2.2.2 Instrument Improvements

Analysis of the requirements for calibrated speckle interferometry discussed in Section 1.2 demonstrated the need for the following improvements to the SO/AFGL speckle interferometry system:

(i) Minimum Distortion Detector. The SO/AFGL camera uses a four-stage image intensifier assembled at SO at minimum cost using Varo inverter tubes. This results in substantial pin cushion distortion and an associated change in resolution and intensity contrast. As a consequence, there is substantial distortion and calibrations must be made in software. Additional difficulties arise in photon counting mode due to systematic spatial variations of the pulse height distributions.

(ii) Improve TV Camera Stability. At present, the TV camera is clocked independently of the Video-memory resulting in frame to frame synchronization problems which to some extent compromise the performance of the subtractions of background and phosphor glow build-up. To correct this both the camera and the memory must function on a common external clock.

(iii) Eliminate Analogue Video Recording. The performance of the camera is compromised by distortion and reduction in resolution associated with the video tape recording system which is used to gather data at the telescope prior to reduction. To avoid this problem it is necessary to digitize the data at the telescope which involves considerable data compression (i.e. expense) if the duty cycle of the system is not to be compromised. Such digitization is also necessary if preliminary on-line analysis is to be possible. In the longer term, any USAF applications of speckle techniques would require essentially on-line reduction.

(iv) Event Detection Logic. At the low light levels typical of work on artificial satellites and most astronomical sources, the event detection mode is the appropriate way to proceed. For this mode, it is a great advantage from the points of view of sampling, signal to noise and speed of reduction to centroid and utilize each detected photon-event. The SO/AFGL detector is to our knowledge unique among intensifier/TV systems in that it already provides for frame to frame subtraction to preclude repeated counting of a single event; this is essential in speckle work if frame to frame correlation is to be minimized.

(v) On-line Real-time Data Reductions. On-line data reductions capabilities are essential for two reasons:

1. Real-time fringe-contrast detection is needed for optimal phasing of the various interferometric paths in the MMT. It is expected that shifts in the telescpe configuration with time (flexures induced by temperature drifts and thermal gradients) and elevation (gravitationally induced flexure) will inevitably require readjustment of the interferometer. Since each of five independently phasable telescopes must be compared to the sixth to be used as a reference, it is essential that this capability to quickly and accurately make these adjustments be implemented.

2. The ability to produce a size and shape estimate immediately upon completion of an observation with no further investment of time for off-line computations is of particular relevance for Air Force applications.

2.2.3 Algorithm Development

Parallel software improvements necessary to support the hardware developments included

(i) Event Centroiding Algorithms. Software realizations of centroid determining algorithms are necessary to determine an appropriate design for the hardware implementations.

(ii) Optimized Code for computing autocorrelation functions from event address lists, is required to allow the immediate implementation of 128 x 128 autocorrelation functions computed from a sub-matrix of the 480 x 512 detector format in existing observatory minicomputers.

(iii) Real-time Algorithms. Suitably optimized algorithms for real-time execution are required. These in turn require a complete, real-time processor capable of implementing on-line the processing expressed in eq. (1.3), for speckle interferometry, including both hardware and software for both analogue and photon-counting modes.

2.2.4 Image Reconstruction

Phase information is necessary to produce true images from the diffraction limited imge power spectra produced by our system. We have had some success with methods initially developed by Fienup. The question remains of how much additional phase information, beyond the seeing corrected image autocorrelation function and the constraints on physical images, is required to make that method (or the blind deconvolution method proposed by Bates) converge to a unique image.

Our experience in previous contract work was with Fienup algorithms, with no initial phase information. These are generally very slow to converge, and do not seem to give consistent results. Both Knox-Thompson and phase-wrapping schemes should give the necessary phase information to allow unambiguous image restoration, especially in conjunction with Fienup methods. Other schemes, including maximum entropy, and the use of the Bochner-Khinchin theorem to guide the phase restoration procedures should be tried.

2.2.5 An Observational Program

Most of the scientific observations were to be made at the 2.3 m telescope, but once the new coherent beam combiner was operational, the program was to be transferred to the MMT. Other large telescopes such as the KPNO 4m were also to be used when appropriate.

(i) Artificial Satellites. During this contract period some slow moving satellites were to be observed to demonstrate on-line capabilities in this area. The 2.3m telescope was not designed to track accurately at high rates (compared to sidereal) so that such observations, limited to rates of order 120 arcsec/sec are of little interest. Our proposal for those observations was not funded.

MMT satellite tracking capabilities, with 8 times the 2.3 m telescope tracking rate, and three times the angular resolution, are more attractive for this purpose. One-dimensional measurements, made initially with the two-beam experimental beam-combiner, measured the angular size of a trial satellite. We have not attempted a full image reconstruction.

Satellite orbital data is available to us through Dr. Eric Jensen of Aerospace Corporation.

(ii) Solar System Objects. The study of surface features of outer solar system planets is of considerable importance to astronomy. The purpose is to follow, where possible, the evolution of cloud structures, vortices, etc., in order to develop an understanding of the atmospheric structure and dynamics. For planets such as Pluto, even diameter and simple shape information such as already obtained, is of value in order to continue the study of the orbital parameters of the satellite. Similarly, for the satellites of the outer planets, direct information on size, shape, etc. is still required. A subject of continued interest to us is the size distribution and possible duplicity of asteroids suggested by present data. This work is supported by NASA (NAGW-224) in a parallel effort. Speckle interferometry still offers the most direct approach for settling this question and has been refined by Drummond and Cocke to determine the orientation of an asteroid's spin axis (pole) and to locate prominent bright or dark spots.

(iii) Astronomical Objects. Our plans for astronomical investigations included continued studies of surface features on supergiant stars, measurements of binary star orbits, search for dust shells around cool stars in which mass loss is taking place, synoptic studies of the evolution of ejecta from novae, studies of the nuclei of Seyfert galaxies and the emission regions around QSO's and a search for gravitational lens effects and gravitational nuclei (black holes) in elliptical galaxies. This program correlates with work also being carried out by Beckers and Hege for NSF (AST-8113212) using differential speckle interferometry techniques.

3. THE MULTIPLE MIRROR TELESCOPE AS A PHASED TELESCOPE

We summarize here the experiments which have used the Multiple Mirror Telescope (MMT) subapertures as a phased array in the optical, infrared, and submillimeter spectrum regions. Those experiments exploit the unique, very high angular resolution of the MMT being equivalent to that of a conventional telescope 6.86 m in diameter. The operation of the MMT as a phased array is not only important for obtaining high angular resolution but also for obtaining the high detection sensitivity which results from the better discrimination against the sky emission background for infrared diffraction limited images. We describe work done in converting the MMT into a phased telescope.

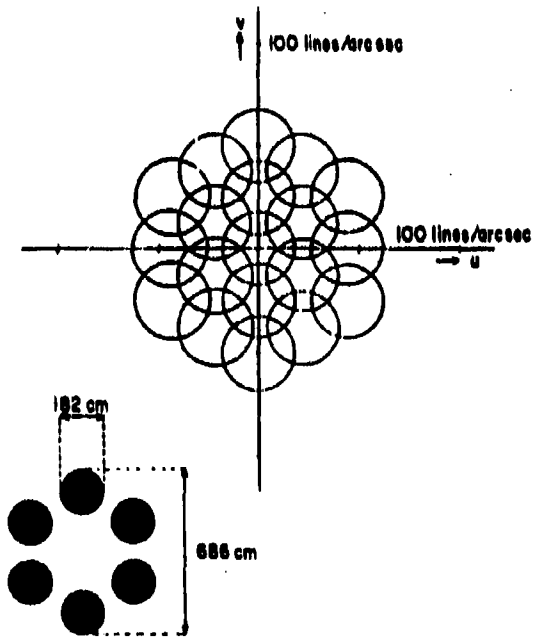

Figure 3.1. On the lower left we show the cross section of the MMT entrance aperture (vertical in figure is vertical on the sky). The central figure shows the coverage in the Fourier transform plane, or (u, v) plane, at a wavelength of 500 nm if the six telescopes are phased.

3.1 MMT Interferometer Geometry

The MMT was constructed primarily as a large light-collecting telescope for astronomical research on faint objects in the optical and infrared spectrum regions. Experiments in the past few years, also supported by NSF (AST-8113212 and AST-8201092) have, however, demonstrated the potential for using the MMT for high angular resolution research. Whereas its equivalent collecting diameter (= diameter of a single telescope having the same collecting area) equals 4.45 m, the MMT has a resolution diameter (= diameter of a single telescope having the same angular resolution) of 6.86 m. This higher angular resolution can, of course, only be achieved if the telescopes are cophased and if the earth's atmospheric effects are accounted for, e.g. by speckle interferometric techniques.

Figure 3.1 shows a cross section of the MMT aperture and response in the Fourier plane (image power spectrum plane) or (u, v) plane when used as a phased array. The (u, v) plane response covers all angular frequencies within the boundaries set by the resolution diameter of the MMT. Many of the frequencies are covered more than once because the MMT array is highly redundant.

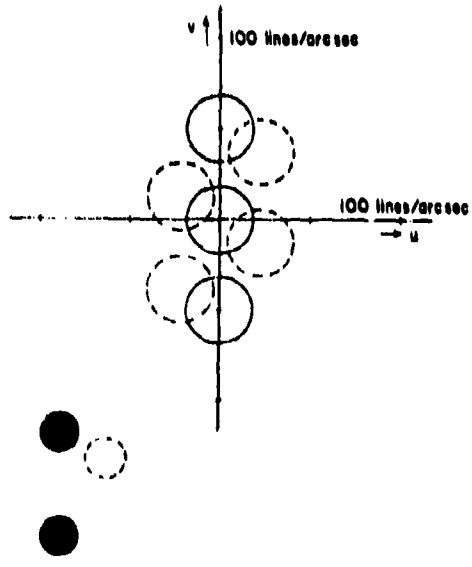

Figure 3.2. As Figure 3.1 but when only using two (or three) of the MMT telescopes.

Figure 3.2 shows a cross section of a subset of 2 (or 3) MMT apertures. With it one covers only a fraction of the (u,v) plane, leaving large gaps. The Figure 3.2 configuration is commonly called an interferometer. Other optical interferometers (Labeyrie 1977, Davis 1983) exist with two mirror configuration with baselines up to 67 meters. They have a very incomplete (u,v) plane coverage, but because of their large baseline they are able to measure a single very high spatial frequency component of the spatial frequency spectrum of a source with an assumed intensity distribution (e.g. the diameter of a stellar disk). By changing the baseline and the projection on the sky, one can improve the situation until a full image is synthesized, as is the case, for example, with the Very Large Array at radio wavelengths. The MMT configuration with 3 mirrors, also shown in Figure 3.2 can be used that way either by using different triads of telescopes or by having its projection rotate across the sky, which is possible because of the MMT's altazimuth mount. In contrast to the interferometer mode shown in Figure 3.2, we will refer to a device with a filled (u,v) plane as shown in Figure 3.1 as a phased telescope. We report here experiments which were done using the MMT as an interferometer (Figure 3.2) and as a phased telescope (Figure 3.1).

3.2 Cophasing the MMT

The MMT has been used at optical (0.4-0.8 μm), infrared (5 μm), and submillimeter (870 μm) wavelength regions as an interferometer or phased telescope. In Figure 3.3 we show schematically how the relative pathlengths are adjusted in the various experiments.

For Submillimeter Experiments the phasing is accomplished by longitudinal translation or focusing of the MMT secondary mirrors (mode A). Since the Rayleigh focal range for the prime focus, $4\lambda f^2$ (primary), equals 25 mm at λ= 870 μm, the defocus for the $\pm$ 2mm secondary mirror adjustment needed for cophasing is insignificant so that the phase sensing is readily accomplished by peaking up the central intensity of an image of a point source. Ulich et al. (1982) showed the measured and calculated intensity distribution of Saturn to be in good agreement.

For Infrared Experiments the telescope pathlengths are adjusted by translation of the beamcombiner (mode B). This was done only for two telescopes (McCarthy, et al. 1982b) so that the MMT worked as a two element interferometer causing fringes across the stellar image when in phase. The cophased condition was sensed by detection of the white light fringe by eye in the optical region which coincides with the phased condition in the IR because of the all-reflecting system (the wedges used for mode C are normally not used for IR work).

In the Optical Experiments the pathlengths have been adjusted by focusing of the secondaries (mode A), translation of the beamcombiner (mode B), and by relative adjustment of pairs of

glass wedges (mode C). Beckers and Roddier (1982) used the Roddier rotation shearing interferometer to obtain interference between two adjacent telescope pupils as seen in Figure 3.4.

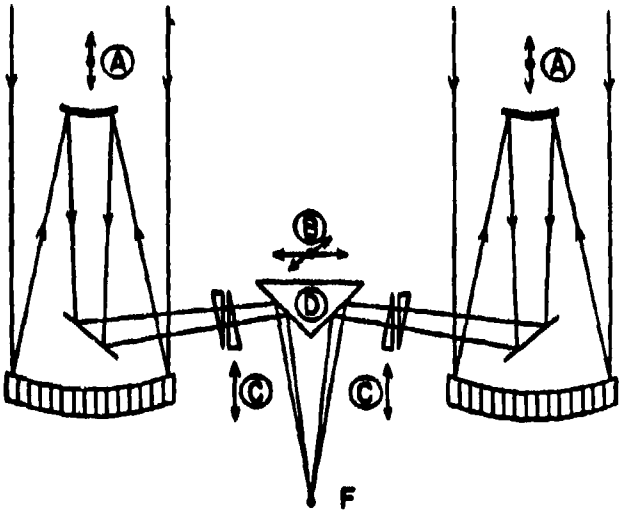

Figure 3.3. Ways of adjusting pathlengths of individual MMT telescopes; A = by longitudinal translation of the secondary hyperbolic mirrors. This may defocus the image by an intolerable mount; B = by sideways translation of beamcombiner in two orthogonal directions. This allows phasing only for up to 3 telescopes; C = by inserting in each beam 2 complimentary wedges and translating one with respect to the other; and D = by separating the six reflecting surfaces of the beamcombiner and translating/tilting them. Drawing is not to scale.

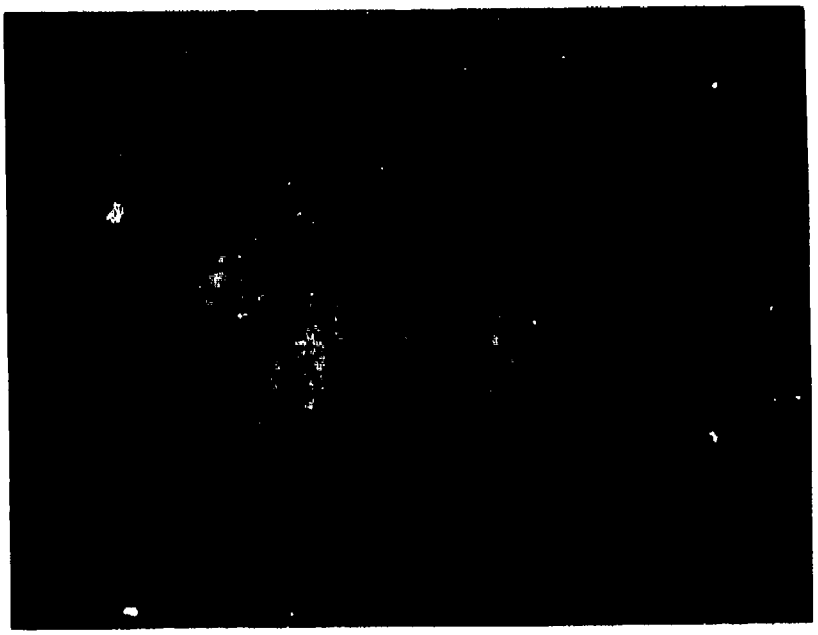

Figure 3.4 Pupil shearing interferometer pupil fringes. A rotational shear has superimposed adjacent MMT subpupils. The actual fringe contrast (and coverage in the overlap region) is much greater than suggested in this vidicon image which, because of video lag effects, is an integration for longer than the fringe correlation time set by the atmosphere.

As active element, they could use the secondary focusing motions since the interference occurs in the pupil plane and is thus quite insensitive to out-of-focus effects. Detection of the cophase condition was done visually directly and by monitoring a TV image.

For conventional speckle interferometry in the image plane, the telescope pathlengths are equalized (mode C) by adjusting pairs of wedges in each of the six beams. Figure 3.5 shows a speckle image (specklegram) so obtained with two telescopes showing the superposition of the two single telescope speckle images and the interference fringes resulting from the cophasing. Figure 3.6 shows the corresponding power spectrum in the (u,v) plane. Figures 3.7 and 3.8 show respectively the fringes (speckles now) and (u,v) response for all six beams.

Figure 3.5. Specklegram of a point source obtained with a pair of phased MMT telescopes. The vertical interference fringes are 27 millisecond of arc apart (wavelength 650 nm).

The cophase condition is detected by visual examination of the video specklegrams, there being at present no instrumentation for fringe sensing. We just watch the real-time video display produced by the intensified video speckle camera (Hege, et al. 1982a). When cophasing the entire telescope, we adjust five of the six pathlengths relative to a sixth chosen as a reference. In order not to confuse the eye, the five telescopes are compared one at a time to the sixth so that only simple fringe patterns such as Figure 3.5 need be inspected. Then all six beams are combined to produce the full-aperture MMT specklegrams such as seen in Figure 3.7.

The cophased condition can be sensed visually with a precision of about 2 μm by centering the white light fringe on the star image. In the future we plan to design and construct an electronic fringe sensor possibly based on a digital television system, using the fast Fourier transform algorithm. Shaklan, Hege and Beckers (1983) have demonstrated the capability for developing instrumentation for measuring the contrast and position of interferometric fringes produced by two phased mirrors of the MMT. The goal of this experiment was to give a preliminary indication of whether or not an automatic mirror phasing system using one of the MMT Point 4 computers would be feasible. We conclude that a given pair of mirrors can be cophased in about 10 seconds to a precision of about 6 μm using stars up to 8th magnitude given a modest hardware FFT device.

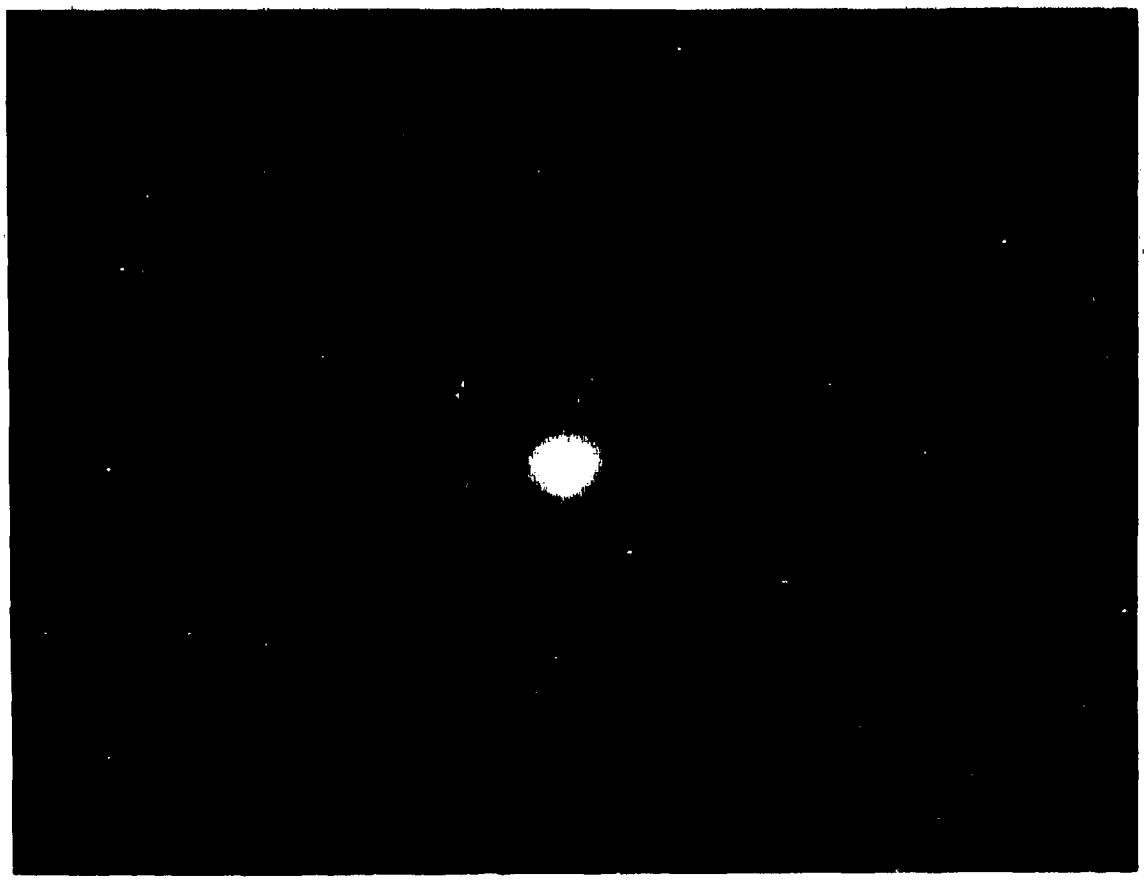

Figure 3.6. Image power spectrum of specklegrams of a point source using two phased telescopes as shown in Figure 3.2.

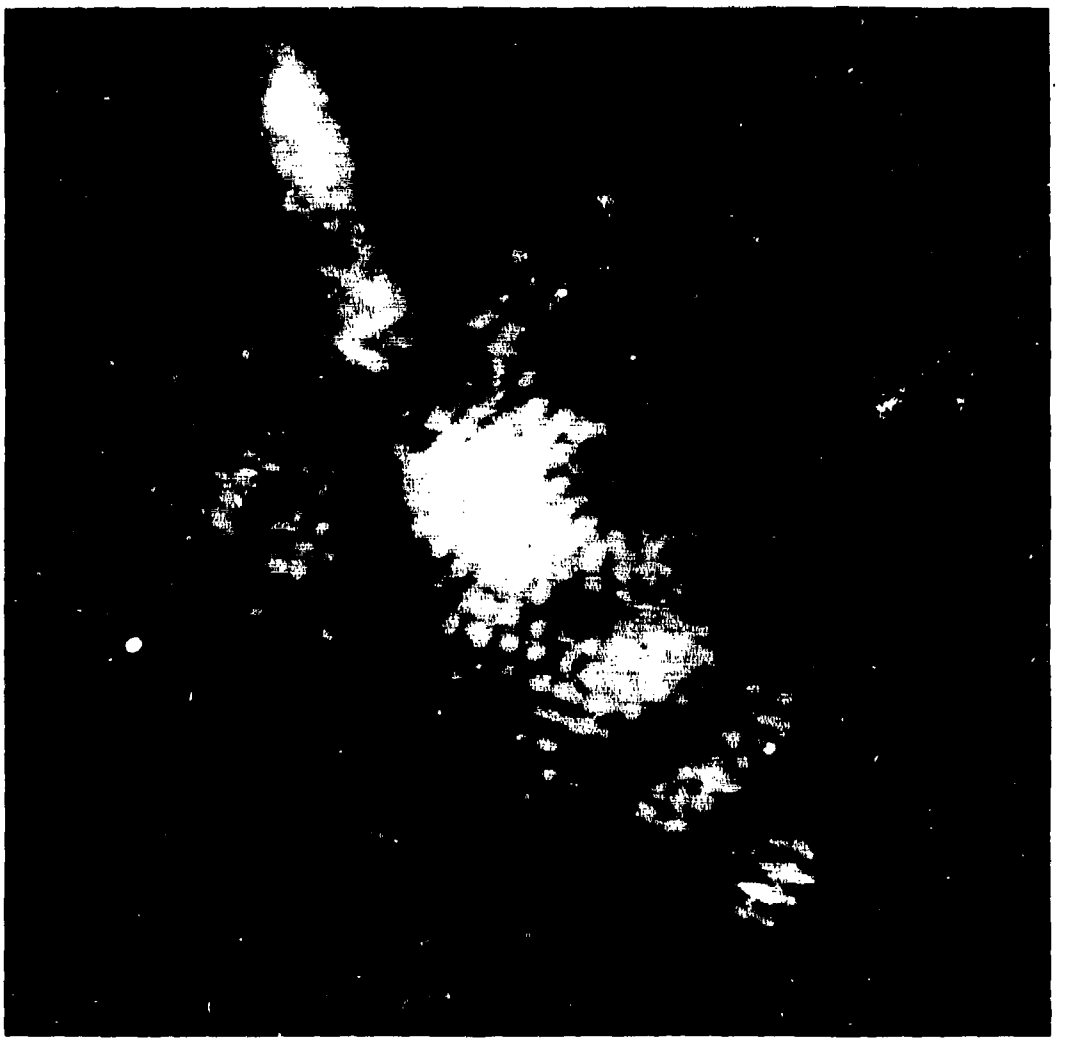

Figure 3.7. MMT specklegrams produced when all six beams are cophased.

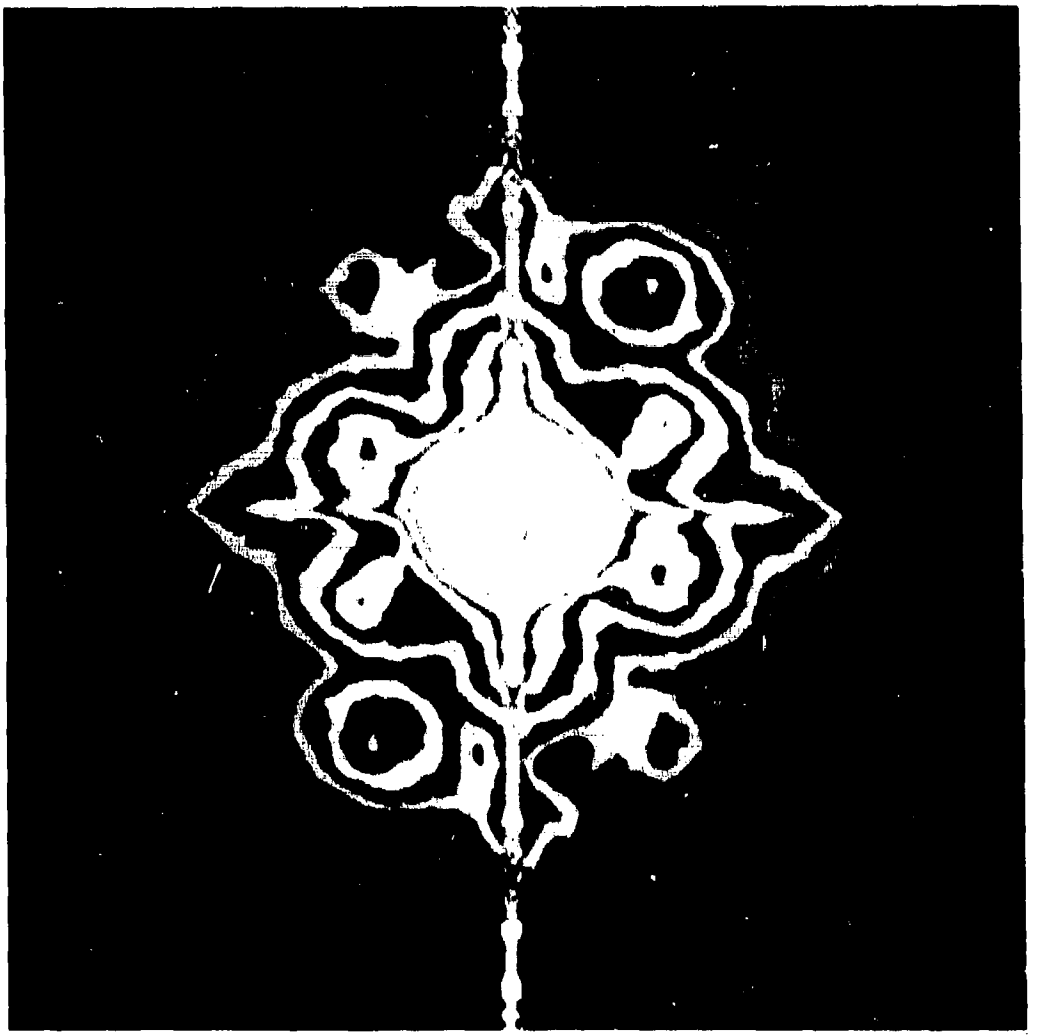

Figure 3.8. Image power spectrum of specklegrams of a point source β Tau observed in a 10 nm bandpass centered at 750 nm using all six beams as shown in Figure 3.1. This is a measure of the actual speckle MTF for the MMT, including atmospheric effects and noise bias. Contours are spaced at $\log_2$ intensity intervals.

As a proof of principle demonstration of an instrumental fringe-sensing system capable of detecting the magnitude and sense of telescope phasing errors, we set up our video system so that the two-telescope fringes were essentially parallel to our video raster lines. Using a simple analogue integrator and 8-bit A/D converter combination, we were able to extract a digitized amplitude from a sample position along each raster line. In that way we extracted a one-dimensional intensity profile across the fringe pattern.

Ideally, the fringes should be centered relative to the seeing distribution, but to determine whether or not our algorithm could detect fringe position, we purposely positioned the fringes at both the top and bottom relative to the seeing distribution, as well as at the center by slightly adjusting the path length.

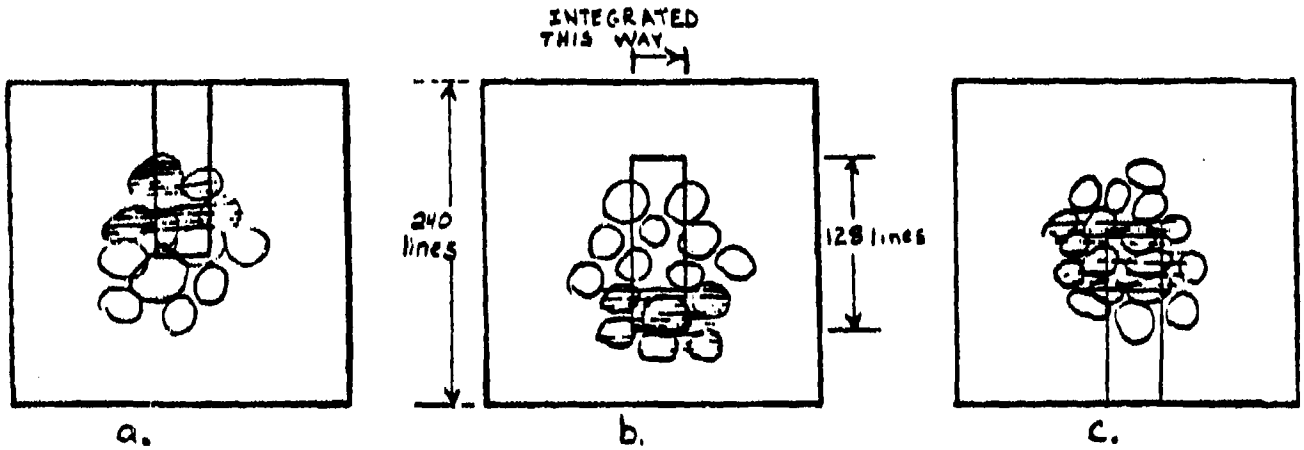

Figure 3.9. Each figure represents a fringe-sample. (a) has the fringes at the top of the seeing distribution and the sample at the top of the raster. (b) has fringes at the bottom, sample at center. (c) is yet another fringe-sample. Note that there are nine possibilities in the scheme.

We sampled data integrated in a strip of width corresponding to the single telescope speckle size across 128 video lines (see Figure 3.9). The sample was moveable; we could position it at the top, center or bottom of the raster. The experiment used the Fourier transformed results to compare fringe contrast statistics for data sampled at the top and bottom 128 lines of the video raster (the center sample was not really needed). For each relative fringe position, we sampled at the three raster positions. A typical power spectrum profile is shown in Figure 3.10.

Letting F be the measured fringe contrast for a given fringe-sample, we define an error signal E as F(sample at bottom) - F(sample at top) for a given fringe position. This gives us an estimate of how well centered the fringes were over the length of the observation (see Table 3.1). The "fringe error" column gives merely a visual estimate (+/- 5 fringes) of how far, on average, the fringes were off-center from the raster, i.e. the distance in number of fringes from the center of the image to the region of maximum fringe contrast. The "path error" column provides the calibration of fringe error in terms of pathlength difference. Thus, for observation A, in which the fringes were centered with respect to the seeing distribution, the "+10" in the "fringe error" column indicates that the fringes were estimated to be 10 fringe widths above the center of the sampling raster, either due to poor centering of the image or offset centering of the fringes on the seeing distribution (our program could not distinguish which). Four different pathlength differences were investigated.

Table 3.1

Fringe Contrast Sensing Experiments

OBS.	Star	Error Sig. F(B)-F(T)	Std. error	S/N	Fringe error	Path error	Sensitivity
A	α Oph	-1.9	1.0	1.9	+10	7.5 μm	4 μm
B	α Oph	2.1	0.7	3.0	-20	15	7
C	α Her	-1.2	1.1	1.1	+10	7.5	6
D	α Her	-0.7	1.2	0.6	< 5	< 4	< 6

The data indicate that our algorithms could in fact detect when the fringes were off-center. For observation A, in which the fringe error appeared to us to be about 10 fringes high, the algorithms found E = -1.9, indicating a stronger signal at the top than at the bottom. The sign of E tells the sense in which to make the correction, (-) to correct down, (+) to correct up. For observation B, in which the fringe error was 20 fringes low, E = 2.1, indicating a stronger signal at the bottom. The C and D observations showed similar results. We point out that statistics for the D observation (the dimmer star) are similar to those for the brighter star. Although at first surprising, this indicates that the statistics are dominated by atmospheric effects (seeing) and image motion (largely induced by telescope motion in this experiment) and not by photon statistics for such objects ($m_v < 4$). It is our experience with other analogue (as constrasted to photon-limited measurements (Hege, et al. 1982) that this is true for objects to about m=6 (if seeing is about 1 arc second). For fainter objects, the photon statistics begin to dominate. In all cases, however, the quantity (F) is a measure of

the mean number of correlated photons detected per scan at fringe frequencies.

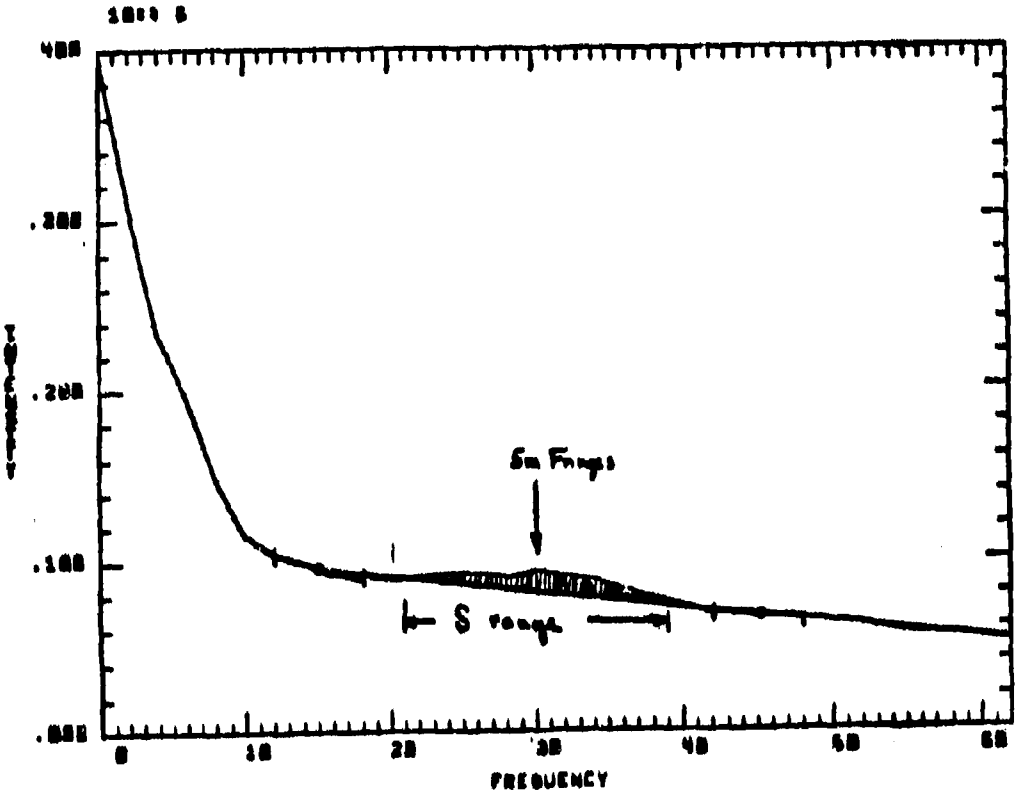

Figure 3.10. The one-dimensional square Fourier Modulus for an unresolved star using an opposite MMT mirror pair. The line segment and the shaded area define the integrated signal calculated by our fringe contrast detection algorithm.

Our contrast-detecting algorithm uses a linear approximation for the noise bias determined at frequencies immediately above and below the expected fringe frequency (see Figure 3.10). The 5 m opposite mirror fringe spacing is 4.3 lines per fringe at 750 nm so that the 5 m baseline is at 128/4.3 = 30 in the 128 point transform. The algorithm then finds the average intensity at those frequencies and determines a line based on those averages. The line is therefore a linear estimator of the noise bias. The algorithm then integrates between the line and the signal. A "fringe contrast" ratio is calculated (= integrated signal divided by the average value of the noise bias). Note that negative contrast ratios are possible because the line may actually be an overestimate of the noise bias; if a very small signal is present, our "contrast" may come out negative because the signal is sitting below this arbitrary line. The relative value is, nevertheless, valid.

All of the data analysis was carried out on a Z-80 with a Forth Floating-point FFT. Fringe contrast data for each fringe-sample (a singe pair of mirrors - 600 samples) took a whopping 15 minutes to compute. But the important point is that only 10 seconds (= 600 fields/60 fields per sec) of data were used for each pair. For full phasing of all six mirrors, 5 baselines x 2 sample-pairs (at top and bottom) x 600 FFT's per sample pair = 6000 FFT's that will have to be executed for 10 second phasing of the telescopes. One must note here that these numbers are only good to m = 6. After that, phasing time increases with magnitude, requiring 100 sec for m = 8.5(which is .1 times as bright as 6th magnitude). These figures show that we require a modest array processor (MC68000 based device) which can reduce FFT times to less than 1ms. Longer integration times, yielding better statistics would, of course, improve the sensitivity to better than the $\pm$ 6 μm or so of this proof of principle demonstration. This experiment was inadequate to allow a prediction of the ultimate cophasing precision one might attain in this way.

3.3 Interferometer Stability

Visual observations of a star image using the TV monitor and a large optical filter bandwidth ($\lambda/\Delta\lambda \sim$ 5-10) easily allow fringe detection for stars brighter than 4th magnitude. With an electronic detector and algorithms such as just described we may gain a few magnitudes, but the fact remains that it will be possible to cophase the MMT telescopes only on rather bright stars. We presently conservatively assume that we will be limited to brighter than 8-9th magnitude stars. To observe faint objects we therefore plan (i) to go to a nearby bright star, (ii) to cophase the telescope on this star, (iii) to go to the object to be studied, correcting for flexure effects, (iv) to continuously correct the pathlengths for flexure and thermal changes, and (v) to return to the bright star after some time Δt to check and improve cophasing. For reasonable use of the MMT as a phased telescope, it is necessary that Δt be long compared to the time needed to cophase the telescopes and that the pathlength corrections for a 5° offset can be well modeled.

Figure 3.11 shows the result of an experiment in which the pathlength change between the two extreme vertical telescopes in the MMT was measured as a function of elevation change while moving the MMT both up and down. The change is very repeatable and there is little hysteresis so that apparently the pathlength change can be modeled to a precision of ~ 10 μm. Much of the remaining variation is due to thermal changes in the Optics Support Structure (OSS).

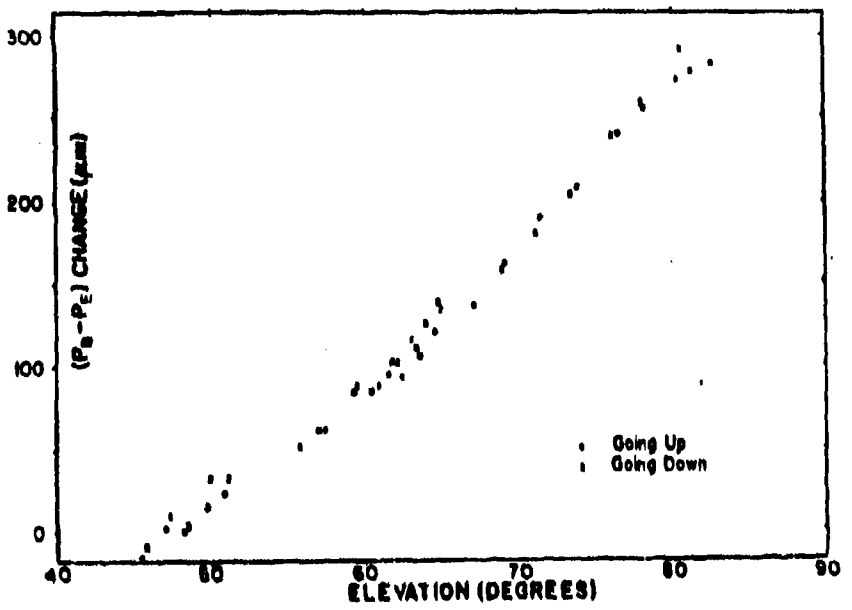

Figure 3.11. Change of pathlength between telescopes B and E as a function of elevation while repeatedly moving up and down.

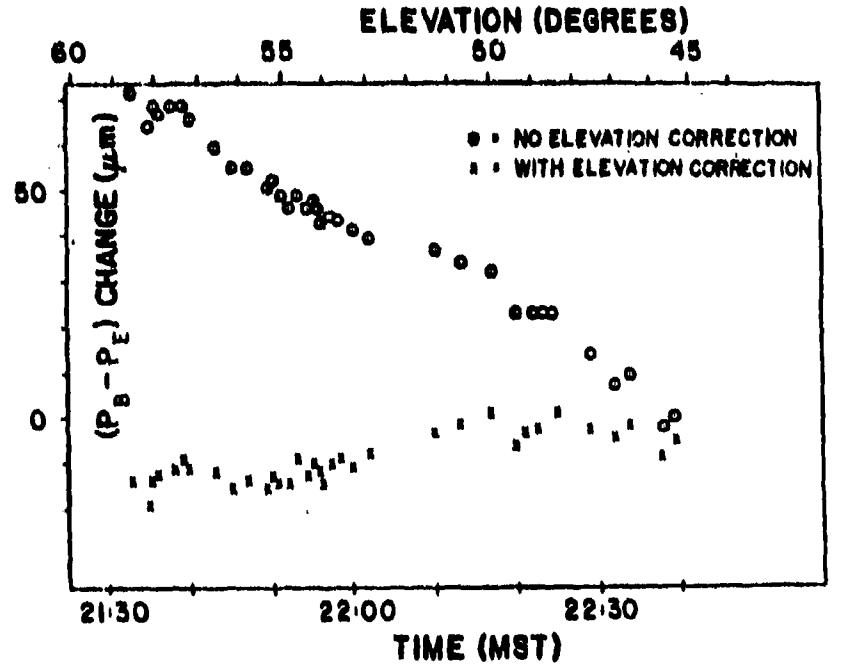

Figure 3.12. Change of pathlength between telescopes B and E as a function of time while tracking a star in the western hemisphere. The circles are the raw data. The crosses, the same data after correction for the elevation change shown in Figure 3.11. The remaining variation of the crosses is mostly due to changes in the mount (OSS) thermal structure.

Figure 3.12 shows the pathlength change for an hour long sequence of observations of a star in the western hemisphere. Most of the change is due to the systematic elevation change, such as shown in Figure 3.11. The remaining change is, for a large part, due to thermal changes in the telescope which can also be modeled. It appears from Figure 3.12 that even without further mechanical improvement, and with a single open-loop model for the elevation change of pathlength, we can control the pathlength to 5 μm over about 30 minutes. Further tests are planned in the future which will include a network of thermal sensors placed across the OSS. At this moment, we measure a pathlength change due to thermal variations of ~ 65 μm/°C (Figure 3.13) so that it will be necessary to monitor the OSS temperature to better than 0.1°C.

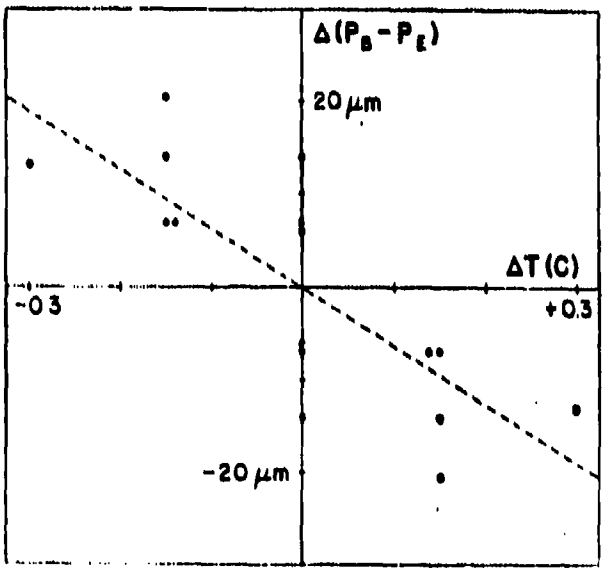

Figure 3.13. Pathlength difference between telescopes B and E as a function of the temperature difference. Dashed line corresponds to 65 μm/°C.

The six pairs of pathlength compensating prisms (mode C, Figure 3.3) are controlled by an Aerotech system including stepping motor drives and precision stages with computer controlable absolute or incremental positioning, and since the controller is compatible with existing (spare!) MMT telescope coalignment control interfaces, it was an extremely straightforward process to implement an open loop control for this cophasing system. We determine for each of the five relative paths a change of pathlength curve such as that shown for telescopes B and E in Figure 3.11. We fit a quadratic equation to each of these five curves and let the computer adjust

the paths correspondingly for changes in elevation. This system is now implemented and the preliminary results using it indicate that the corrections implied by the X's in Figure 3.12 can indeed be achieved for all five relative pathlengths. We have not yet added thermal compensation to this system, but plans to do so are currently underway.

3.4 Instrumental Isoplanicity and Coherence Considerations

The telescope cophasing system just described allows us to bring the six principal rays together in the MMT quasi-cassegrain focus F cophased. This does not imply that (i) the rays stay cophased when looking at a star off the axis of the telescope (so that the image is translated off the telescope axis), and (ii) that rays coming from other points of the telescope pupils are cophased with their principal rays.

Beckers, Hege and Strittmatter (1983c) have analyzed the MMT optics to show that the first condition (i) is met by making the angular converging ray geometry approaching the focus F match the linear aperture geometry of the telescope. Since the maximum edge to edge distance of the six 1.82 m diameter MMT mirrors equals 6.86 m (Figure 3.1), and since the individual telescope beams converge in F at a f/31.6 ratio, that means that the overall f-ratio of the MMT should be f/8.39 (8.39 = 31.6 x 1.82/6.86). With this f-ratio, the white-light fringe crossing the superimposed images of an unresolved star stays centered on that image as the telescope is pointed slightly away from the star (i.e. as the image is moved off-axis). The small change in f-ratio from the original f/9 configuration of the MMT is presently accomplished by a small (0.6 inch) raising of the tertiary mirrors and a small adjustment in the tilt (0.1°) of these mirrors.

The second condition (ii), also analyzed by Beckers, Hege and Strittmatter, is automatically fulfilled in the focal plane of a single perfect telescope. The focal planes of the six MMT telescopes are, however, tilted with respect to one another so that the average focal plane of the MMT (the plane at right angles to the overall telescope axis) deviates from the individual focal planes by 2.5 degrees. As long as the distance between the planes is less than the Rayleigh focal range ($\pm 2 \lambda f^2$ or $\pm$ 1 mm at 500 nm, and $\pm$ 10 mm at 5 μm), the phase difference between the central and edge rays of the pupil equals less than a quarter wave. This corresponds to a diameter of the field of view of 164 arc seconds at 500 nm and 1640 arc seconds at 5 μm. Over the so-called isoplanatic patch at 0.5 μm (~ 4 arc sec), the maximum phase difference is $\lambda/160$, much less that the differences introduced by the atmosphere and by telescope imperfections, so that the focal plane tilts have a negligible effect on the cophasing. If desired, however, these tilts can be removed by, for example, the scheme described by McCarthy, et al. (1982b). In practice this is not nessary.

Figure 3.14 summarizes the analysis of the off-axis condition (i). The condition which has to be met is that the path difference in the central rays for an off axis star outside the telescope (δD) equals the path difference between the rays converging to the common image plane F inside the telescope. The focal planes of each of the telescopes are shown as dashed lines in Figure 3.14 whereas the image plane is shown as a full drawn line. The path difference for the off-axis star inside the telescope is therefore $2\alpha\Delta$. If the effective focal length of the telescopes equals F then $\Delta = \delta F$ and $2\alpha = D/F$. The beam convergence (f-ratio) of each of the telescopes is β radians = $d/f = 1/31.6$ so that the condition (i) is met by making $2\alpha/\beta = D/d$. This means that the angular convergent ray geometry in the image plane must be mapped into the linear aperture geometry. It can easily be shown that the same condition has to preserve not only the overall geometry of the MMT aperture but also the point to point geometry as well.

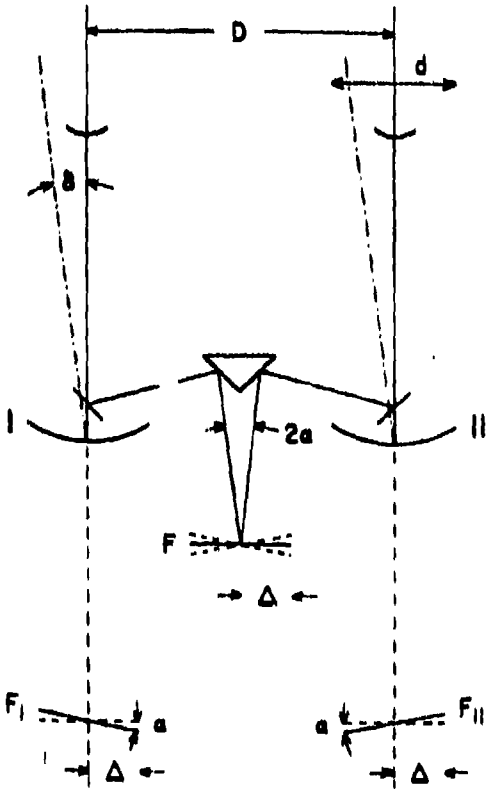

Figure 3.14. Schematic of optical paths in MMT for two telescopes I and II. D = geometrical separation of centers of telescopes, d = geometrical diameter of single telescope, 2α = angles which principal rays make in final image, δ = angle of off axis star to telescope axis, and Δ = distance of off axis star image to center of image plane.

We have analyzed the detailed effects of the tilted focal planes on the non-principal rays. Condition (ii) is met exactly for the principal rays for both on-axis and off-axis objects. We can show that the condition (ii) is also met with sufficient precision for non-principal rays by referring to Figure 3.15.

Consider an off-axis, seeing limited image with seeing disk of s arc seconds produced by a single telescope of diffraction limit $t = 1.2\,\lambda/d$. Clearly the cophasing condition (i) will assure that the pathlengths for all wavelengths are equal at P (the white light fringe is centered). The off-axis principle rays A_1, and A_2 at the detector focal plane are properly phase compensated (white light fringe also centered) if the geometric condition (ii) is satisfied. It remains only to investigate the effects due to the phase errors for the non-principal rays within the seeing distribution. The pathlength error at the edge of the seeing disk is $P = 2\epsilon = s\alpha$, but $2\alpha = 5m/F$ and $S = F/206265$ for 1 arcsecond seeing. Thus $2\epsilon = 12\ \mu m = P$.

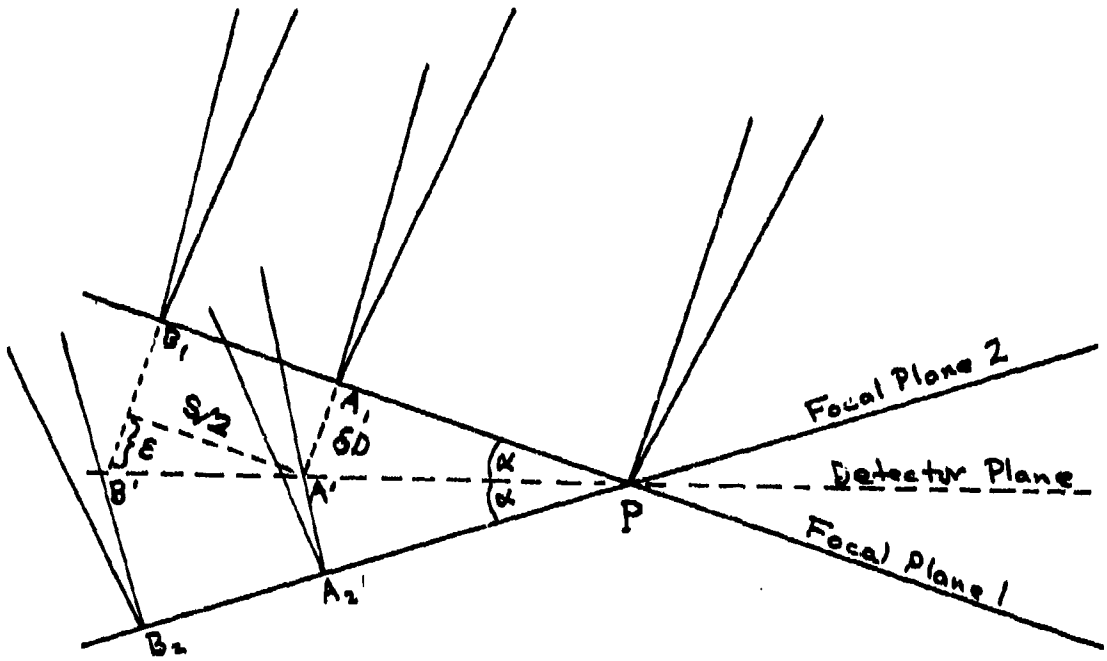

Figure 3.15. Titled focal planes of two single telescopes shown with reference to the detector focal plane which is the mean focal plane for all telescopes. P is at the focus of the principle ray for an on-axis image. A and B are focal points at the center and edge respectively in a seeing limited, off-axis image.

Note that, just as the internal path difference at A_1 compared to P is matched by the external path difference, this path difference is also compensated by the external path difference. The only effect is the difference in phase for light of different wavelengths transmitted in a finite bandpass traversing this distance. Let us require that, for negligible loss of contrast, this phase error be less than 1/10. The condition $(P/\lambda_1) - (P/\lambda_2) < 1/10$ implies that $\Delta\lambda < 0.1\lambda/P$ or $\Delta\lambda < \lambda^2/120\mu m = 2.1nm$ at 500 nm.

For a perfect f/8.39 telescope of 6.86 m aperture in 1 arcsecond seeing, the phase error at the edge of the seeing disk at 500 nm is $n_p \sim (S/2)/(tF)$. Evaluating this at 500 nm yields $n_p = 28$. If again we insist that, after n_p cycles, the phase error is less than 1/10, $n_p \Delta\lambda < \lambda/10$ or $\Delta\lambda < \lambda/(10n_p)$ which at 500 nm gives $\Delta\lambda < 1.8$ nm. There is also a phase error associated with the seeing in the individual 1.83m mirrors. For a 1.8m mirror $n_p \sim (S/2)/(tF) = 7.4$ cycles. This reduces the maximum permissible bandpass for the interferometer system to $\Delta\lambda < 1.6$nm compared to 1.8nm for a perfect telescope of equivalent resolution. The ratio 1.8/1.6 implies a 15% effect, at most, to the precision of these approximations.

We conclude that there is no significant degradation in the performance of this MMT configuration due to titled focal-plane effects for 1 arcsecond seeing at 500 nm.

An additional requirement for optimal interference is that the polarization characteristic of the light passing through the six telescopes is not affected (or is affected in the same way). McCarthy et al. (1982) have shown that to be the case for wavelengths > 2 μm. For optical wavelengths linear retardation occurring on the off-axis reflections of the tertiary mirror and beamcombiner decrease the fringe contrast between non-opposite telescopes somewhat. In the final configuration we may decide to restore the full contrast by insertion of retardation compensating optics. We emphasize that image power spectra do in fact contain energy at all frequencies expected, as can be seen by comparing the actual observed MTF (Figure 3.8) with its predicted basis (Figure 3.1). No detailed analysis of the relative amplitudes at particular frequencies has yet been carried out. The particular example (Figure 3.8) results from data taken without even the closed-loop corrections operating, so it may be expected that amplitude distortions produced by imperfect cophasing may predominate over any other effects seen in this preliminary measurement, which represents only a qualitative proof of principle of these concepts.

3.5 A Six-beam Optical Measurement: Capella

Further qualitative evidence of the validity of this phased array configuration is shown in Figure 3.16 where the binary nature of Capella is seen as visibility minima crossing the 6.86m

image power spectrum, also obtained without benefit of open-loop cophasing correction. From this measurement we infer a separation of components of approximately 1.5 times the diffraction limit -- the second visibility minimum occurs just at the power spectrum cutoff frequency. Table 3.2 compares the observed positional parameters with those accurately known from the well determined (McAlister, 1981) orbital parameters.

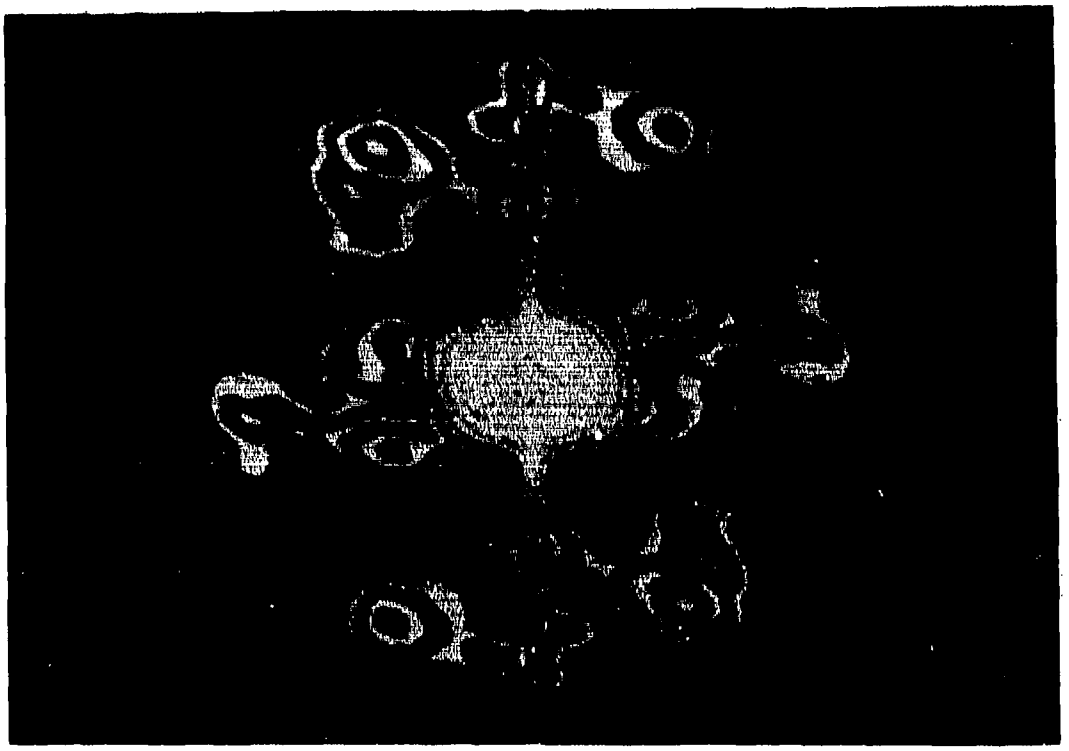

Figure 3.16 Capella. Image power spectrum obtained from specklegrams using the full 6.86 meter MMT aperture in a 10 nm bandpass centered at 750 nm. Contours same as Figure 3.8.

Table 3.2

Speckle Interferometry of Capella - Oct. 1983

	Observed	Predicted
Separation	38.2 msa	40.1 msa
Position Angle	327°.3	321°.2
Relative Intensity	0.5 (750nm)	0.2 (550nm)

The relative intensity value is obtained by calibrating the image power spectrum for Capella shown in Figure 3.16 by dividing it by the image power spectrum for Tau (unresolved) shown in Figure 3.8, both corrected for noise bias. If the speckle MTF for both of these measures was identical (including seeing effects) then this would have produced the square of the visibility function for this binary object. The two-dimensional result is shown, together with an inset showing the average visibility profile, in Figure 3.17.

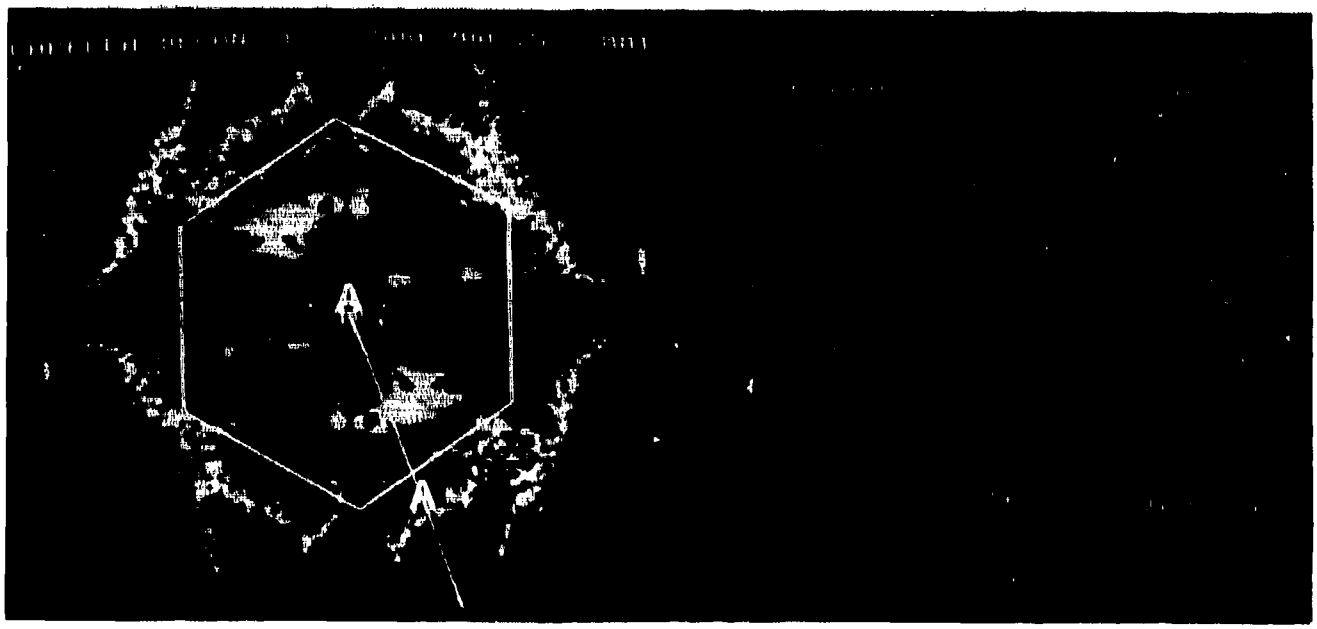

Figure 3.17. Two-dimensional visibility function for Capella. The smooth curve is a least squares fit from which a magnitude difference of $m = 0.5$ is obtained. The theoretical aperture cutoff is represented by its circumscribing hexagonal border. The cut is taken perpendicular to the visibility fringes as marked A-A' on the two-dimensional quotient.

These preliminary results are very encouraging and are the only presently available quantitative evidence of the effectiveness of this phased telescope for optical interferometry. Open-loop cophasing corrections should only improve future results and make possible the extension of these techniques to faint objects. Further data, taken in the interval November 1983 through January 1984, awaits reduction.

4. SPECKLE INTERFEROMETRY INSTRUMENTATION

For high resolution imaging of astronomical objects through the Earth's atmosphere it is necessary to sample images in the telescope focal plane at the diffraction limit of the telescope with integration times sufficiently short to freeze the atmospheric turbulence. Most interesting objects are so faint that only a gentle rain of photons is collected, even with the largest telescopes. The atmospheric correlation time is so short that only a few detector pixels will collect even one photon during the short exposure at the required image scale. The object is to record the coordinates of the pixels which detect photons.

Since even the best direct integrating video detectors have a readout noise of a few electrons per pixel, an image intensifier system is used to make the signal due to a single photoelectron event unambiguously detectable by a standard video camera. Our present detector consists of four stages of electrostatic inverters transfer-lens coupled to a Plumbicon camera, and produces video events of 0.4 volts average peak amplitude for corresponding photoelectron events (Hubbard, et al. 1979, Hege, et al. 1980).

4.1 High-resolution, Minimum Noise Dectector Requirements

Experience with our present intensified plumbicon video system, together with evidence from other workers (Nisenson et al. 1982), establishes rather strong criteria for detector performance. In order to have single-photon detection, detector-lag elimination is required to remove frame-to-frame detector correlation. This is accomplished by frame-subtraction for both analogue and raster-event localization schemes, and we have found the results to be effectively lag free. For astrometric and photometric reasons in conventional speckle interferometry as well as for differential work, very low geometrical distortion (less than one pixel in a 512 x 512 primary raster) is required.

Proximity focused electrostatic image intensifiers (Cromwell et al. 1983), configured in a system with sufficient gain for good photo-electron pulse discrimination provide greatly improved geometrical fidelity and geometrical stability compared to either electrostatic inverters or magnetic focused devices. High quantum efficiency (>20%) and low dark current (<10 $e.cm^{-2}.sec^{-1}$ at $-30^{o}C$) are required in order to obtain useful specklegrams of m_v=15 or fainter objects, although these levels of dark-emission are difficult to achieve for proximity focused devces ith good red response. Also, very fast (<1 μs) output phosphors are required if event detection at 10^6/sec is to be achieved.

The geometrical fidelity and stability and the linearity and dynamic range of the system cannot be better than that of the image intensifier readout system. This immediately rules out

electron-gun video systems in the changing environments of an instrument mounted on an astronomical telescope. Solid-state, direct readout (MEPSICHRON) cameras (Fermani et al. 1984), as well as the event localizing schemes such as described below (secton 4.2.2), appear to meet the requirement that the performance of the primary detector (the first stage image intensifier photocathode) not be degraded.

Although the majority of speckle interferometry to date has used exposures of 20-50 ms (we typically use 33ms as defined by the 30Hz video framing rate), we have experienced atmospheric conditions on many occasions when speckle interferometry could not be effectively accomplished with exposures greater that 1 to 10 ms. In this case, rapid shuttering with frame-subtraction (with subsequent loss of duty-cycle in a standard video raster scheme), or time tagging schemes (with subsequent increase in specklegram rate) are required. The time-tagging, photoelectron-localization schemes appear very attractive as means of introducing variable (and therefore optimizable) frame rates. However, particularly for short correlation times, this places even greater demands upon subsequent signal processor bandwidths. It may be desirable to have both time-tagging and conventional video detectors.

Our proposal to assemble an intensifier/detector system consiting of 2 proximity focused tubes, a microchannel plate intensifier and a reducing boule coupled to a fiber optical input Plumbicon TV camera was not funded.

The analogue resolution of the entire system is dominated by that of the Plumbicon camera and yields no more than 130 elements across the target with conventional camera electronics. With the modifications proposed, it would have been possible to increase the analogue resolution of the TV by a factor ~ 2 (the Plumbicon is capable of this performance). We would ultimately choose to implement a fiber coupled CCD, primarily for astrometric reasons. The system can be adapted to CCD use at a later stage if eventually funded.

We emphasize that for speckle interferometry with raster scan video detectors (unlike, for example, spectroscopy) it is the number of analogue resolution elements per frame that is of importance even in the photon counting mode. The reason for this is that only events that occur in the same speckle in the same frame yield information on the source structure. In practice, we have found it useful to substantially over sample the specklegrams beyond the Nyquist frequency associated with the telescope diffraction limit. The reasons for this are to permit adequate separation of the detector transfer function (DTF) from that of the telescope and hence also to provide sufficient sampling of the aperture MTF that information at this scale can be recovered. The proposed camera would have provided adequate sampling at all conventional telescopes and the expected improvement to the existing TV camera resolution which is necessary for an optimized system at th MMT. Note that the

intensifier package would then yield more than 400 analogue resolution elements at 550 nm which is adequate for full aperture work at the MMT.

Our experience with analogue video data-logging has also revealed severe limitations, both in dynamic range and bandwidth of U-matic 3/4 inch video cassette recorders. This same experience has, however, proven the value of archiving the primary video data, which should be preserved even as on-line data-reduction capabilities are implemented. Archived data can subsequently be reduced by different algorithms to extact different information (Or to correct prior procedural or parametric errors) if it is preserved in its original form.

The compressed format of time-tagged event addresses is the best contender for a high-fidelity primary data archive, expecially for fainter objects where recording only non-zero pixels is a considerable advantage. Although quite expensive, digital video recording techniques can maintain the speeds required if full-format recording of amplitudes for bright objects is required.

Finally, we proposed to build into the new detector package better magnetic shielding to minimize differential distortions introduced by the changing orientation of the telescope, particularly important for differential speckle interferometry (section 4.4).

4.2 Real-time Photoelectron Event-detecting Video Systems

In previous contract work, we had carried out a study of the pulse height distribution of the detector system and had shown that the interframe difference signal is highly suited to unitizing. Therefore it is necessary:

(a) to implement a single frame readout mode (i.e. eliminate the standard video frame interlace).

(b) to provide line-centroiding logic which will permit events to be localized first to ~ 1/2 an analogue resolution element (~ 500 pixels) and later to 1/4 (~ 1,000 pixels).

(c) to provide line-to-line event centroiding with closely similar resolution properties.

The resultant output should be addresses of photon events in ideal form for rapid computation of auto-correlation functions and phase differences. The hardware must have the capability of registering photoelectron events as unique single-pixel events in a 480 x 512 pixel format at 30 Hz frame rates using a standard video format or in a 240 x 512 pixel format at 60 Hz using a non-interlaced, repeat field format.

4.2.1 Video Raster Event Detector

For one-dimensional centroiding to one-pixel precision the stability of the combined camera-digitizer system must be such that no relative drifts as large as one pixel can occur. A hardware processor is required to localize each event to a single pixel along a raster line and an appropriate computer interface is needed to output the element address together with its associated line number.

We have constructed a system (Macklin, et al., 1982) for localization of photoelectron events utilizing an intensified Plumbicon camera and a Grinnell video digitizer. The Grinnell digitizer, arithmetic unit and memory are used to produce a real-time video difference between current pixel value and previous pixel value thereby suppressing multiple detection of the same event. Our event-localization scheme provides double-buffered line-address and event-amplitude for up to 32 events along a 512 pixel video line. A software algorithm allows localization of multiple detections of the same event, and provides a unique address interpolated with single line resolution by the host minicomputer in a 240 x 256 format.

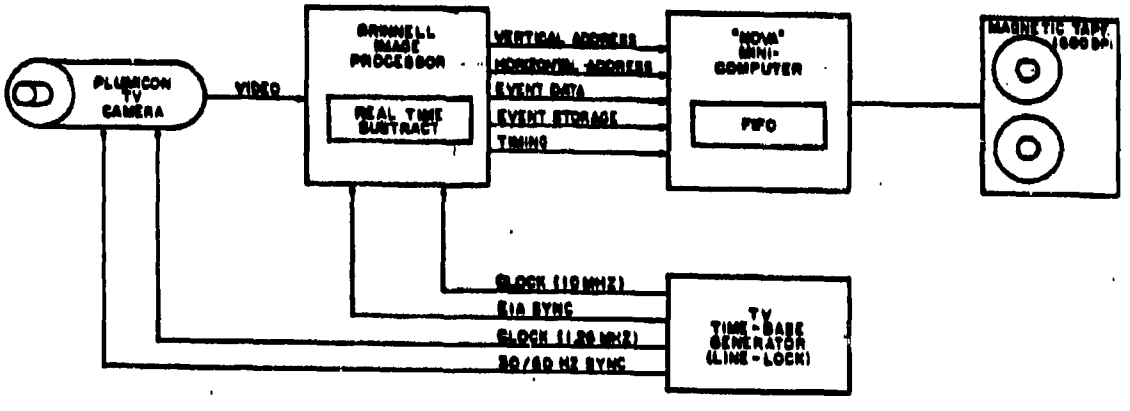

Figure 4.1. The basic data path.

The components of our digital system are 1) a Grinnell Systems 8-bit video digitizer and memory, 2) a Steward Observatory specified video subtractor provided by Grinnell, 3) real-time digital peak-detection hardware, 4) a FIFO-buffered burst-transfer DMA-channel interface to the host computer, and 5) cross-line centroiding logic.

The basic data path is shown in Figure 4.1. In the Grinnell system, the RS-170 video is applied to the input of a TRW-1007 flash converter which produces an 8-bit Analogue-to-Digital conversion at 10 MHz. The system is totally synchronous from the TV camera to the computer interface. Camera synchronization is provided by a 10.080 MHz crystal-controlled oscillator phase-locked to the 60 Hz line at 168,000:1.

The video subtractor option allows this 8-bit video to be stored in the frame memory as the value for the same pixel in the previous frame is retrieved and then forms the 8-bit video difference: current value minus previous value. This video difference is then analyzed by our circuitry to localize all peaks which exceed a predetermined threshold amplitude.

The video subtractor is shown schematically in Figure 4.2. The video frame buffer is 480 lines by 512 pixels at 30 Hz.

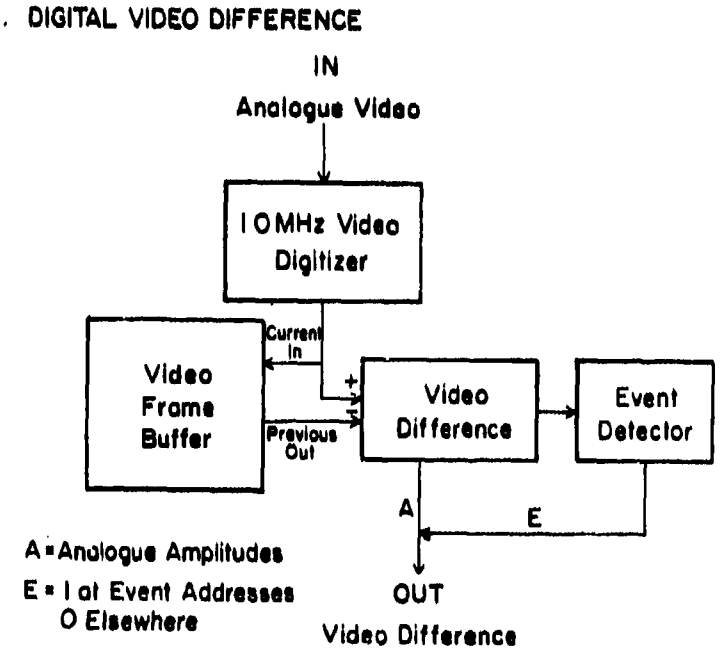

Figure 4.2. The video subtractor.

The video difference (Grinnell) is hardware constrained to be positive or zero; negative differences are suppressed. Thus only new information in the current field is detected. This eliminates any lag effects due to the detector. Figure 4.3 shows a typical example of the digital video input stream.

The upper trace (shown arbitrarily displaced) is a single line of the digitized input video stream. The lower trace is the digital video difference output for the same line resulting when the corresponding line from the previous frame is subtracted. The traces are arbitrarily shown with 256 point/line by plotting only even numbered pixels. The point spread function of these photoelectron events is 4.4 pixels FWHM (2.2 points as plotted here) after convolution with the response functions of the image intensifier, relay lens, camera, video tape recorder, time base corrector and video digitizer. This is equivalent to 130 μm FWHM at the photocathode. The localization of such events with $\pm$ 1 pixel precision improves the event-localization precision of the system by somewhat more than a factor of 4 to 30 μm FWHM at the photocathode. Our system resolves the response 114 through 118 as two events at 115 and 117. The overall resolution of the system remains that of the analogue response function, however!

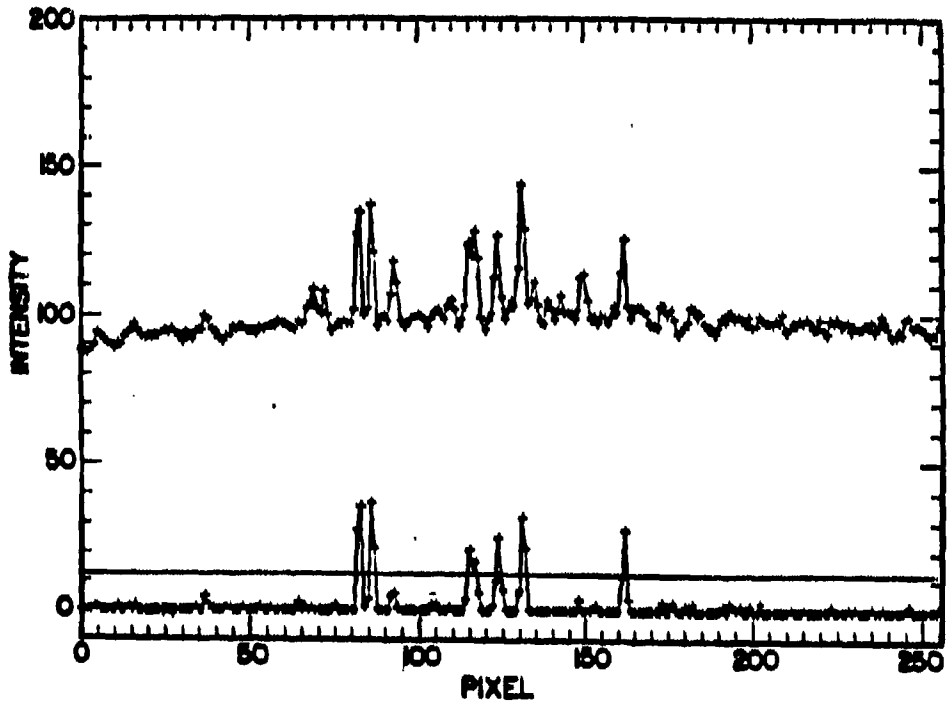

Figure 4.3. Digital video difference.

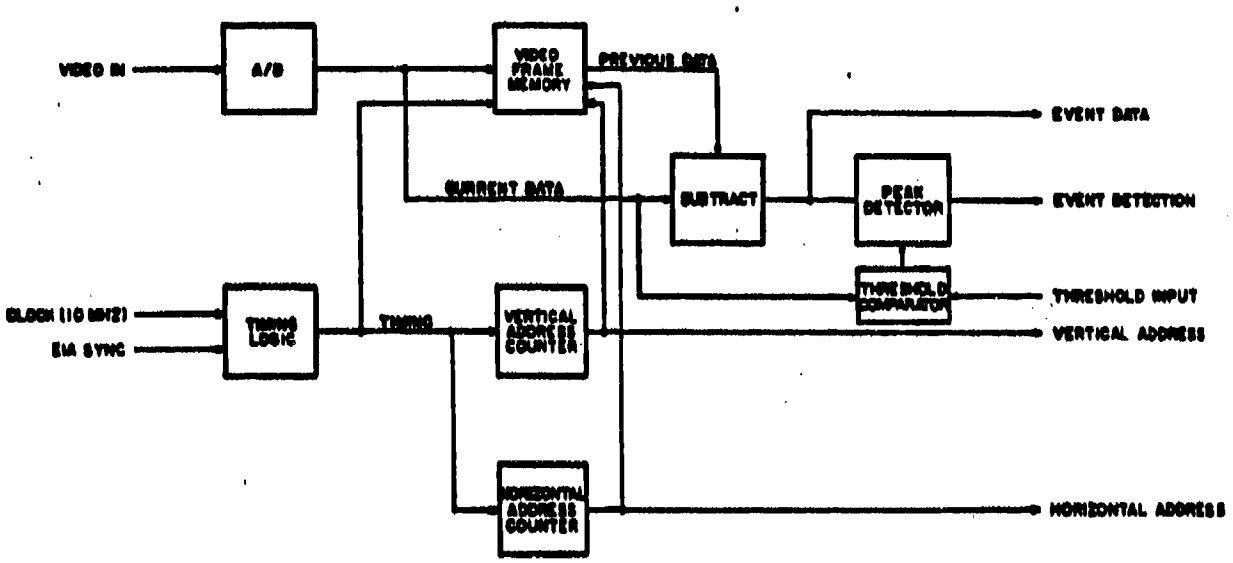

Figure 4.4. The centroiding logic.

The video difference is stored in an 8-bit parallel, single-cell shift-register. The inputs and outputs of this shift-register are applied to an 8-bit comparator. As the difference data are being shifted past the comparator at 10 MHz, the logic tests for the shift-register input to be less than the shift-register output. When this occurs an event-detection strobe is generated. In order to discriminate between low-level noise peaks and large-amplitude signal peaks, the comparator is enabled or disabled by a second 8-bit comparator comparing the difference amplitude to an 8-bit threshold value. The qualified event-detection strobe is then passed to the computer interface.

The centroiding logic, shown schematically in Figure 4.4, contains a horizontal address/vertical address multiplexor. The 64 by 16-bit 10 MHz FIFO buffer, horizontal and vertical qualification registers, and data channel (DMA) control logic are all in the computer interface.

Data are stored in the computer through the data channel. There are 1 + n words for each video line within the vertical qualification window ($0 \leq n < 32$). The number n is the number of horizontal events detected along the line. The upper bound 32 is

set somewhat arbitrarily by the data channel rate of the Data General Nova class host computer used in our application. The entry of a video line-number is tagged by MSB = 1. Horizontal event entries, tagged by MSB = 0, contain both the horizontal address and the 5 most significant amplitude bits. Our design anticipates eventual implementation of 10-bit (1 in 1024) horizontal addresses ($\pm$ 15 μm at the photocathode).

The interface uses a 64 by 16-bit FIFO buffer to allow the computer to accept burst transfers at up to 6 times the rate that the data channel can accept them. For a 10 MHz video-sample rate, the maximum peak detection rate is 5 MHz (200 ns peak separation). The data channel rate is only 800 KHz (1.2 μs per word). The 64 word FIFO provides a 2-line buffer with input at 5 MHz and output at 800 KHz.

When the vertical address equals the bottom of the vertical qualification window, an interrupt is generated to inform the event-logging program that the current frame of data is complete.

Presently cross-line centroiding (1 in 240) is produced by a software algorithm in the data reduction computer. Using the analogue amplitude information, photoelectron addresses are localized to unique pixel events on a 240 x 256 grid which recognizes cross-line events with -1, 0, or +1 pixel horizontal displacements. The maximum data-logging rate of 60,000 Hz is set by the 75 ips 1600 bpi magtape system. This is compatible with the 32^2 addresses/frame saturation of the interface.

With a three-line circular buffer a hardware processor to localize an event multiply detected on adjacent scan lines could be implemented to produce unique photoelectron addresses. However, we do this crossline event centroiding (at considerable cost in processing time, and equivalently in observing duty cycle) in software in the host minicomputer.

4.2.2 Direct Event-address Readout

Recently a mask-encoding image intensifier event-position readout system has been developed at Harvard/SAO by Papaliolios and Mertz (1982). We have begun a collaboration with Drs. C. Papaliolios and P. Nisenson of Harvard/SAO in order to evaluate the effectiveness of this detector system in our observing programs. The present realization of that system was tested satisfactorily in an observing run using the 2.3m telescope in October 1983. The primary features of the Papaliolios system are

(i) a 256 x 256 format in an 18 mm square (25 mm diagnonal) patch of an image intensifier output. This may be eventually expanded to 512 x 512 format.

(ii) a maximum event detection rate of 10^5 events/second, essentially anywhere in the field of view.

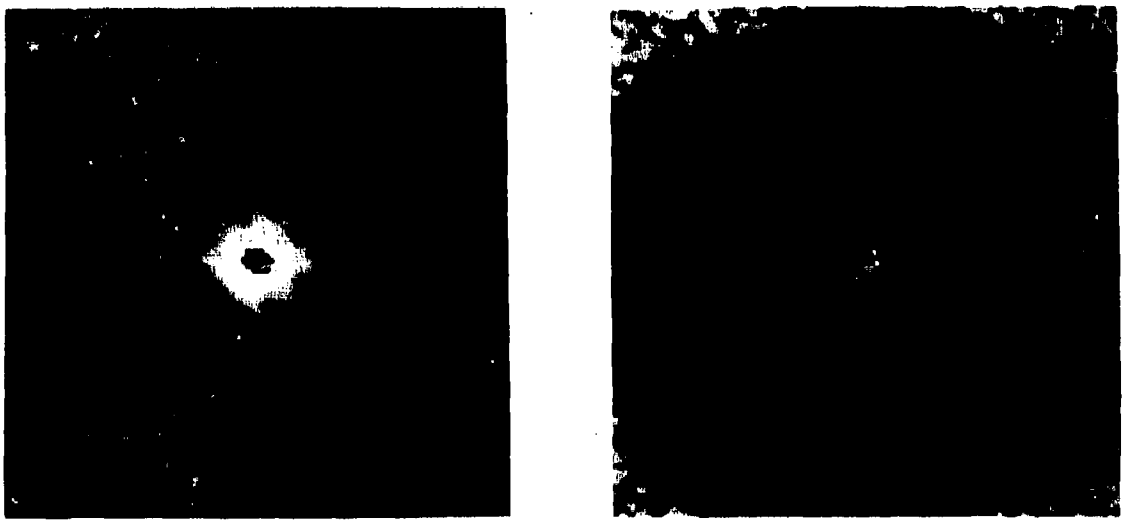

Figure 4.5. Power spectra resulting from the Papaliolios photon-counting camera. a) Left is the power spectrum for γ Ori, recently discovered to be a binary. b) Right is the power spectrum for the (well) resolved asteroid Vesta after deconvolution using the power spectrum of an unresolvable source.

(iii) true single pixel point-spread-function. The spatial resolution, set by the Nyquist limit, is 18mm/256 elements (at full resolution) = 70 μm.

(iv) low spatial distortion. The image intensifier presently used with the system has only a single stage of electrostatic inverter gain, followed by distortion-free microchannel plate gain. A further refinement would be to use a proximity focus first stage.

(v) low dark current. The usual good performance of Varo photoelectronic devices is achieved, i.e. less than one dark photoelectron per correlation time (typically about 20 ms).

(vi) uniform sensitivity. No significant vignetting is produced by reduced image intensifier gain (or equivalently increased differential magnification) near the edges of the field of view. There are, however, some residual flat-field effects.

These flat-field problems persist even when a flat-field correction is applied, frame-by-frame (by treating photons as floating-point numbers inversely proportional to the flat field response), as seen in the Vesta result.

(vii) true digital output. No further processing is required to produce event addresses. The output of the system consists of the time-ordered sequence of digital (x,y) pairs corresponding to the event coordinates. This could directly feed an on-line processing system. Presently this address list is recorded digitally on a video cassette recorder. This recording media provides the necessary bandwidth to log up 10^5 address pairs per second produced by this detector. Since the events are merely time-ordered and not time tagged, event rate measurements are required to divide the address lists into frames corresponding, on the average, to the atmospheric correlation time.

Typical results produced in that preliminary observing run, shown in Figure 4.5, are very encouraging. Especially significant is the proper debiasing achieved by simply subtracting the number of photons detected from each pixel of the power spectrum as predicted by simple Poison noise statistics. Upon further experimentation, a derivative of this photoelectron event-readout system, with an improved image intensifier primary detector may prove to be the system of choice for speckle interferometry.

4.3 High-speed Digital Signal Processing for Speckle Interferometry: A Proposal for a Real-time Processor.

It was an objective of this project to specify in detail the components of a system capable of producing on-line seeing-corrected autocorrelation functions in 480 x 512 format and to simulate the performance of such a system in 128 x 128 format. The system should be able to record on-line, with 100% duty cycle at up to 1,000 events/frame, the entire 480 x 512 format for off-line processing to exploit the full image resolving capability of the MMT. The fast auto-correlation algorithm requires word-length of at least 18 bits to accomodate the 480 x 512 data format on-line, and is hence beyond the capabilties of present Steward Observatory minicomputer systems.

The limitation on the array size arises from limitations in the memory capabilities of the EDS.4 computer systems at the observing sites. Large autocorrelation functions will require large minicomputers or dedicated hardware processors and associated memories. The 128 x 128 format is adequate, however, to sample objects of small extent (0".5 or less) at the aperture limit of the MMT. Such a small format would not be able to sample a region of the scale of the full isoplanatic patch at the full resolution of the MMT, however.

Nisenson et al. (1980) have proposed a scheme based upon the accumulation of four arrays, each of which is derived from the

complex Fourier transform and summed over the ensemble of specklegrams, which can be the basis for an integration yielding the Fourier phases. We propose in this paper a hardware realization of the procedure.

Given $FT(i(x,y)) = I(u,v) = A(u,v)e^{i\,(u,v)}$, the four arrays which are to be accumulated are:

$\langle I(u,v) \rangle$	Equivalent to the Long Exposure.	(4.1)
$\langle \lvert I(u,v) \rvert^2 \rangle$	The usual Power Spectrum.	(4.2)
$\langle I^*(u,v)I(u + \Delta u,v) \rangle$	An X-phase array.	(4.3)
$\langle I^*(u,v)I(u,v + \Delta v) \rangle$	An Y-phase array.	(4.4)

Nisenson et al. (1980) show that (4.3) and (4.4) effectively yield phase differences which can be integrated to yield the desired transform phases for a Knox-Thompson style two-dimensional image reconstruction. In a subsequent paper, Nisenson et al. (1983a) have shown that this method can also be corrected for the effects of photon noise bias. Hence it is our method of choice for both bright objects as well as faint objects for which the photon noise bias becomes dominant.

In practice, we have found that ordinary computational methods are prohibitively slow for even the usual power spectrum processing and that ordinary array processors of the AP-120B class would not provide the through-put to implement the above four-array algorithm on a sufficiently fine grid to sample the diffraction limit of the MMT in a real-time integration at 60 Hz (or even 30 Hz). We require the accumulation of the four arrays noted above for 8-bit video data digitized on a 256 x 256 raster for every 16.7 ms (60 Hz) video field in order to utilize the full duty cycle of the observation for faint objects. In searching for a technology capable of this task, we found that the special-purpose signal-processing hardware optimized for radar and sonar signal processing appears to satisfy our requirements. Hence we propose a Signal Processing Systems SPS-1000 based system (Hege et al., 1983).

The configuration of the proposed SPS-1000 signal processing subsystem for digital speckle interferometry is illustrated in Figures 4.6 and 4.7. The system is shown in both minimum and maximum configurations. The minimum system provides a modest but acceptable level of performance at a minimum cost. The minimum system can be incrementally expanded to improve throughput until an optimum configuration is reached. The maximum configuration uses a different basic processor and therefore would involve a more extensive modification if a smaller configuration is built first. However, since all models of the SPS-1000 use the same byte sliced building block modules, the smaller processor can be converted, at the factory, to the larger one. Thus the proposed system provides a systematic means whereby the performance of the digital speckle interferometry system can grow.

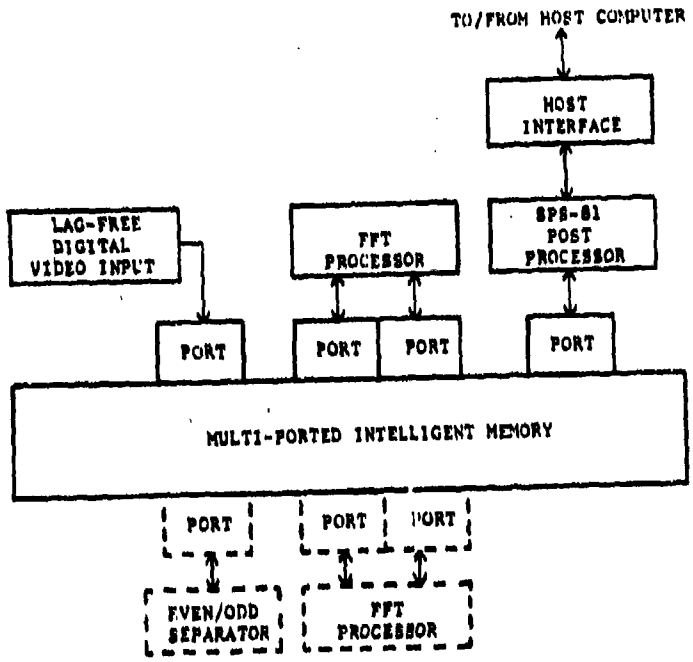

Figure 4.6. Minimum system.

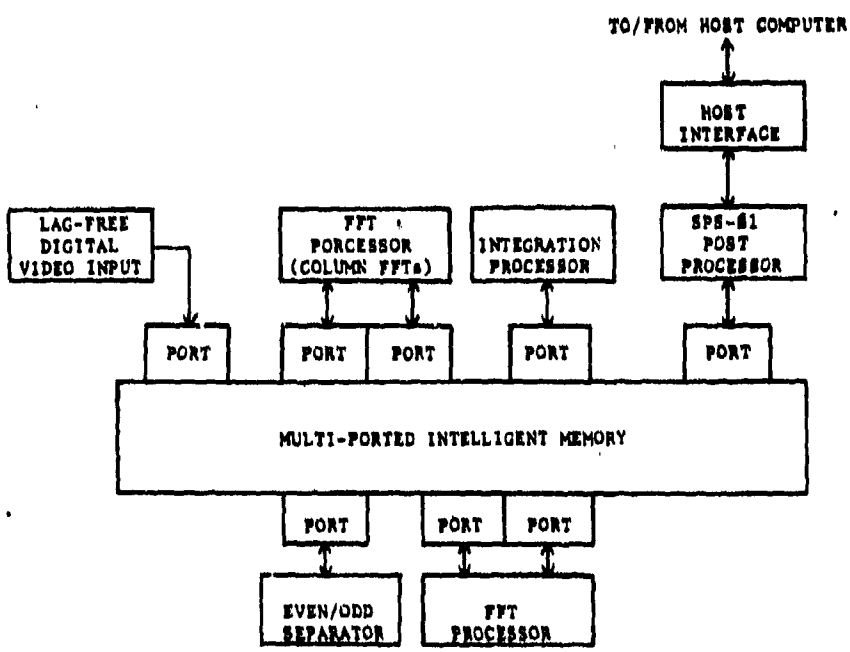

Figure 4.7. Maximum system

As mentioned previously, the use of a conventional programmable processor such as a general purpose computer and/or an array processor is precluded by the high computational rates required by the algorithms used. At the same time, it is desired that the system be programmable to some reasonable level to permit modification of the techniques used. This desire, coupled with the high cost and schedule risk associated with development of a special purpose hard-wired processor, motivated the selection of the SPS-1000 for the signal processor.

The SPS-1000 is a memory centered multi-processor system which was developed to facilitate implementation of high speed real-time signal processing systems such as radar and sonar. It uses a multi-ported intelligent memory to provide attachment points for a variety of processors each optimized for a specific part of the overall signal processing task. These processors may be general purpose computers, array processors, microprocessors, hard-wired modules, etc. For applications which involve Fourier Transforms, the manufacturer offers an imbedded Fast Fourier Transform (FFT) processor which attaches to two of the ports of the memory. A general purpose programmable signal processor (the SPS-81) with throughput comparable to that of a high speed array processor is also offered as an imbedded processor.

The use of intelligent memory as the system integration medium, coupled with a manufacturer supported block diagram compiler, permits the system to operate under program control by application oriented high level language statements.

For the minimum system we selected a small SPS-1000 processor designated the SPS-1016-15. This system includes an imbedded FFT processor which will perform continuous FFTs of up to 1024 complex points at sample rates up to 1.9 megabytes. FFTs larger than 1024 points are accomplished at one half that rate. Two dimensional FFTs are accomodated by using the same pipeline for both the row and column FFTs. The throughput of the system can be doubled by adding a second FFT processor so that the row and column FFTs are accomplished concurrently. The SPS-1000 can be prewired to accept the second FFT processor as a plug-in option to facilitate future expansion.

For the maximum system we selected a faster version of the SPS-1000 designated the SPS-1016-45 with an additional FFT processor. This system can perform continuous two-dimensional FFTs on complex data input at over 6 megabytes.

Both the minimum and maximum systems use an SPS-81 imbedded processor as a post FFT processor. In the case of the minimum system, the SPS-81 can perform the integration of the transformed data as well as the post integration processing. For the maximum system, the SPS-81 is not fast enough to do the integration. Therefore, for this version a specialized imbedded processor will be used to accomplish the integrations and the SPS-81 will be required to perform only the post integration processing.

Table 4.1. System Performance Tradeoffs

Frame Size (pixels)	Minimum System Frame Rate (Hz)	Minimum System Pixel Rate (MHz)	Maximum System Frame Rate (Hz)	Maximum System Pixel Rate (MHz)
128 x 128	70	1.15	170	4.42
256 x 256	18	1.17	84	5.51
512 x 512	4.6	1.21	23	6.03

Both the minimum and maximum systems are programmable, so that a variety of application software packages can be developed to provide tradeoffs between various performance parameters. For example, Table 4.1 indicates the tradeoff between frame size and frame rate for each of the two configurations discussed in this paper.

The frame rates and corresponding pixel rates indicated in the table are the maxima which can be accomodated by the system. Since the system is data driven, the data can be input at any rate up to the maximum for the particular frame size used with no change to the software. The maximum frame rates given above for the minimum system can be approximately doubled by adding the second FFT processor which is indicated by broken lines in Figure 4.6. The performance numbers for the maximum system already include the second FFT processor. All of the above numbers presume maximum utilization of the capability of the hardware. Prudence dictates, however, that some 5% to 10% reduction of these numbers be applied to allow a performance margin as in all programmable digital processors.

The input data to the system are real whereas the FFT operation is inherently a complex number algorithm and the outputs from the FFT are complex. Although several algorithms exist for performing real to complex FFTs, the FFT processor of the SPS-1000 does only complex to complex FFTs. For the minimum system, the input data will be made "complex" by inputting zeros in the imaginary parts of the complex input words. This makes for some inefficiency in the first (row) FFT operation but is in keeping with the concept of a minimum system. The result of a complex FFT on real input data is a conjugate symmetric array, one half of which is the desired result. Therefore, one half of these results can be ignored in doing the column FFTs and no further ineffiencly results. Thus, the processing of an N X N input array results in an N/2 intermediate array and a similiar output array.

For the maximum system, advantage is taken of an option offered by the manufacturer of the SPS-1000 to efficiently

perform real to complex FFTs. This option, called an even-odd separator unscrambles the results obtained by performing an FFT on a pseudo-complex input array which is obtained by packing successive even and odd input samples as the real and imaginary parts of complex words. This technique reduces the input rate and the size of the row FFTs by half and results in increased system performance. The even-odd separator can also be included in the minimum system to provide a further performance improvement over and above that which can be achieved by a second FFT processor.

The implementation of the signal processing functions for the minimum and maximum systems are illustrated by Figures 4.8 and 4.9. The two implementations are identical except for the packing on input and the even-odd separation between the row and column FFTs. In the minimum system the four integrations will be performed by the SPS-81 processor whereas in the maximum system these will be done by a specialized processor attached to a separate port. In both cases the image reconstruction will be done by the SPS-81 processor.

The entire signal processor is attached to a host computer which provides the application program files and the downloading function. The host computer can be connected directly to a port or can interface to the system through the SPS-81 processor. We have chosen the latter since the SPS-81 requires a host interface in any case and thus one port can be saved.

Since the basic concept for this system is an intelligent, multi-ported memory system, considerable flexibility in implementation of and variants to the basic speckle processing algorithm are possible. We have discussed only the requirements for Knox-Thompson based image reconstruction in order to limit the scope of this discussion. However, the flexibility of the system is adequate to allow implementation of other image retrieval methods such as the complex deconvolution of differential speckle imaging or the neighborhood processing required by phase-following approaches. By employing more integration buffers and simple first-moment calculations one could implement "r_o-monitoring" as proposed by Mariotti, et al. (1983) to improve the precision of seeing calibrations, for example.

We believe this type of system provides an optimal compromise between hard-wired signal processors (the ultimate in speed) and conventional, floating-point processors (the ultimate in algorithmic flexibility).

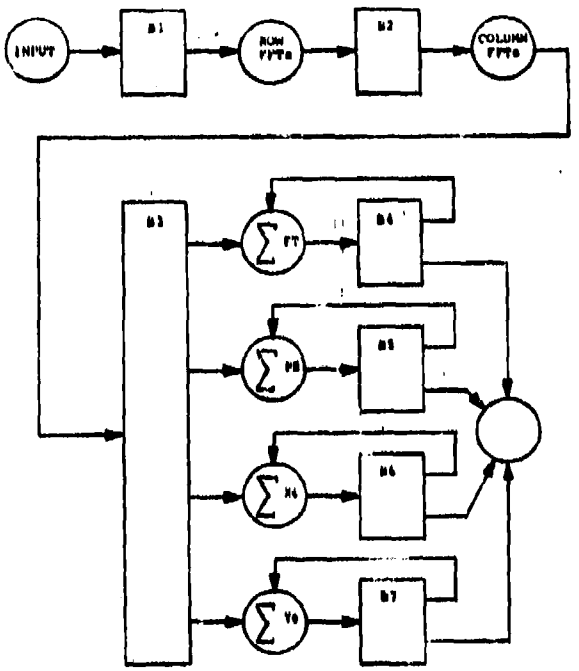

Figure 4.8. Minimum processing

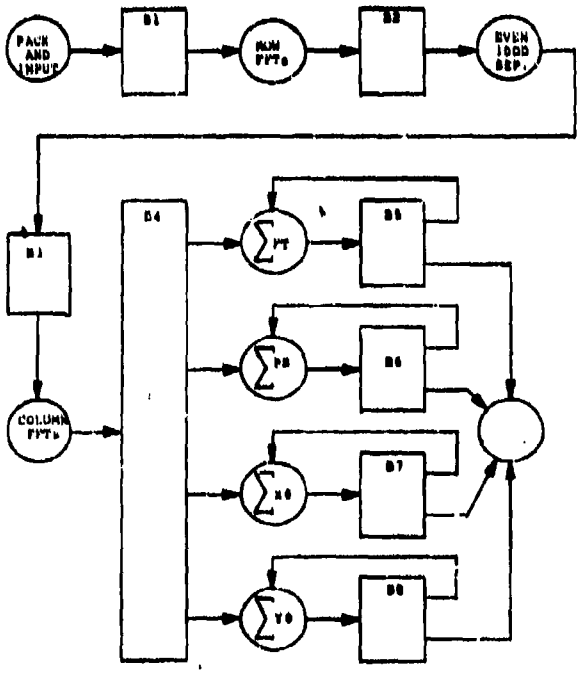

Figure 4.9. Maximum processing

Therefore we conclude that the data-processing requirements, which now make speckle image reconstruction computationally impractical, can be met by implementation of currently available signal-processing technology. The raw data sets from which true image reconstruction can be achieved can be accumulated in real-time (image power spectra and image phase arrays) at the telescope just as optical spectra (in raw form) are presently integrated in real-time while the observation progresses. No serious implementation of diffraction limited astronomical optical image reconstruction should settle for less.

4.4 The Differential Speckle Camera

Differential Speckle Interferometry (DSI) is a technique in which simultaneous specklegrams are taken in two nearby wavelengths in order to derive information which relates to the differences in the object as seen in the two different wavelengths (e.g. due to Doppler shifts, stellar emission or absorption lines, Zeeman effects, etc.). The differential speckle camera (Beckers et al.1983a) uses narrowband (0.04 - 0.16 nm) solid etalons with mica spacers, together with a 2 nm blocking filter, to produce the two (polarized) observing bandpasses. These are then deviated to produce separated images with a Wollaston prism. A 1/2-wave plate can be used to chop between the two polarization states in each wavelength channel, or in another mode to cause the camera to act as a differential speckle polarimeter. In a third configuration, a dispersing element can be used in place of the narrowband filters to produce a speckle spectrograph which, when used with a slit of size comparable to the telescope diffraction limit, produces a set of one-dimensional specklegrams as a function of wavelength.

Figure 4.10 shows a diagram of the differential speckle camera (DSC) as it has been constructed for use with the MMT, the Steward 2.3 m and the KPNO 4 m telescopes. After a reflecting stop at the telescope focal plane which feeds the field viewing optics and the TCS of the MMT, the light passes through a collimator/camera lens system which images the light onto the intensified video system at either 25x or 45x magnification. The area between the collimator and camera is a versatile optical bench/instrument bay into which the various configurations can be inserted as shown at the right in Figure 4.10. In a few minutes it is possible to modify the optical configuration to any of those shown in figure 4.10, or variants thereof, including (default: no components in instrument bay) conventional speckle interferometry, in which case the microprocessor controlled anti-dispersion system (Hege et al., 1982a) is placed ahead of the entire DSC system. This instrument is now our instrument of choice for all modes of speckle interferometry at all of the telescopes noted above.

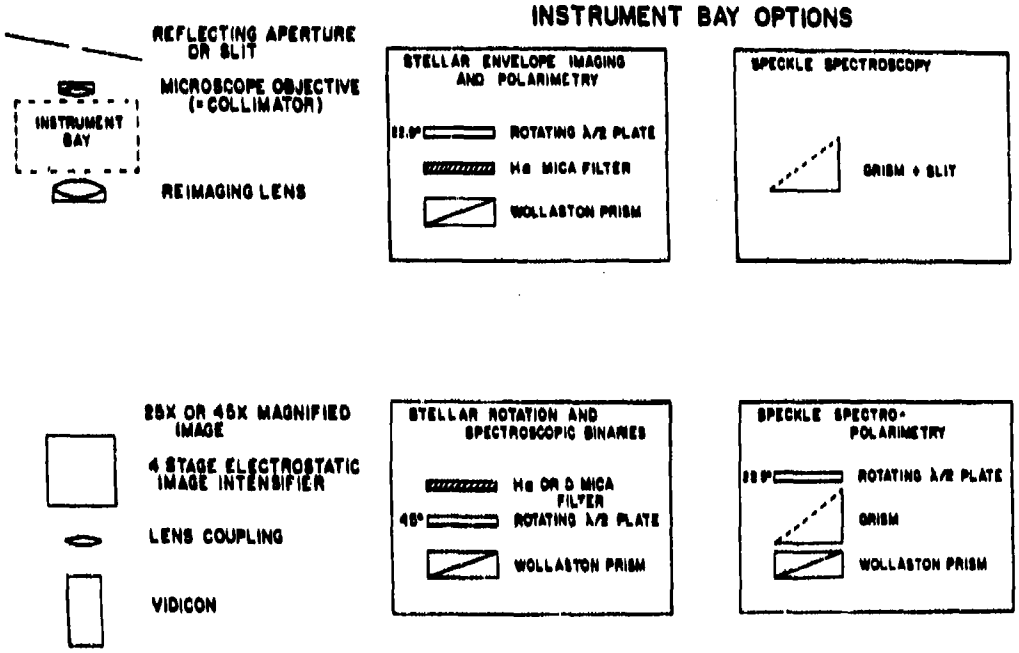

Figure 4.10. The Differential Speckle Camera. On the left is shown the optical configuration of the instrument. In the middle and right are shown the different configurations of the instrument bay used for different types of observations.

4.4.1 Differential speckle imaging mode

In the differential speckle imaging mode the optics bay contains the following components:

(i) A solid Fabry-Perot etalon (Dobrowolski filter) which, since mica is birefringent, has two passbands for orthogonal linear polarizations. The spectral separation is determined by the mica thickness. Blocking filters (not shown) are required to eliminate undesired orders. All optics, including lenses, waveplates, etc., are high efficiency antireflection coated to reduce possible effects resulting from multiple reflections and to produce the highest possible optical throughput.

(ii) A Wollaston prism which separates the two specklegrams corresponding to the two polarization directions to produce two distinct images in the intensified video focal plane. Figure 4.11 is an example of such simultaneous specklegrams of α Tau, one in the H_α line and one in the nearby continuum.

(iii) A rotating half-wave plate driven by a microprocessor controlled stepper motor which, when located in front of the mica filter and rotated in 22.5° steps, makes the DSC a linear polarimeter. When located between the mica filter and the Wollaston prism and rotated in 45° steps it swaps the wavelengths of the two specklegrams.

Figure 4.11. Double specklegram formed by the DSC using Wollastan beamsplitter. The right, brighter image is taken in the continuum 0.55 nm to the red of the H_α absorption line in α Tau. The left image is taken at the center of the H_α line.

4.4.2. Speckle Spectroscopy Mode

In speckle spectroscopy the entrance aperture is replaced by a 5 μm to 10 μm wide slit (about equal to the speckle size) and the optics bay contains a GRISM (Carpenters Prism) or a zero deviation refractive disperser. The part of the specklegram intersected by the narrow slit is therefore spectrally dissected and recorded by the detector. Figure 4.12 shows a low dispersion speckle spectrogram taken with two opposite phased MMT telescopes. The baseline between the two telescopes runs parallel to the spectrograph slit so that the interference

fringes are at right angles to the slit. The spectral behavior of both speckles and interference fringes are clearly shown. Both speckles and fringes separate linearly as a function of wavelength as they should, being interference phenomena. By using the rotating (22.5° steps) half waveplate and the Wollaston prism, the speckle spectroscopy can be combined with polarimetry, a feature which is of interest for certain stellar observations where polarization in lines is known to exist.

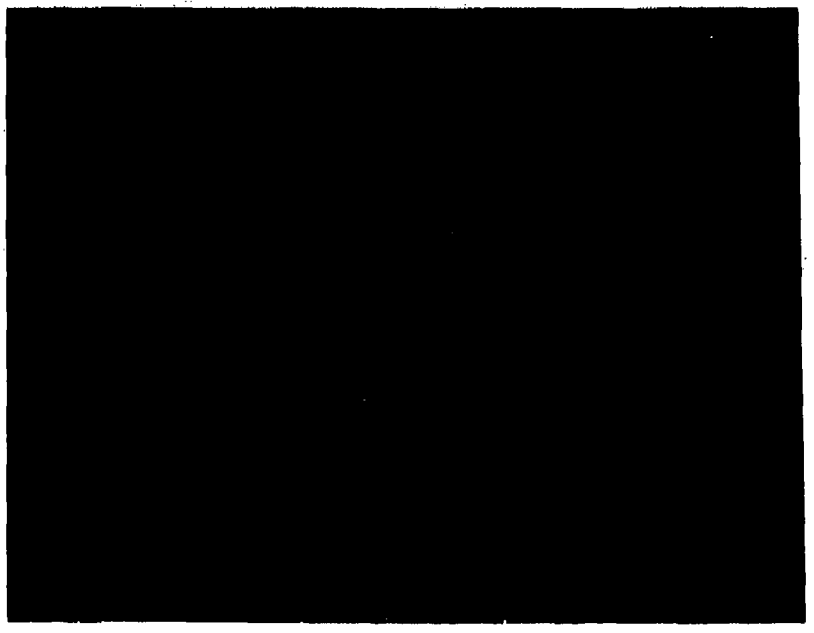

Figure 4.12. Speckle spectrogram taken with two phased MMT telescopes (separation = 5 m). Wavelength runs from 450 nm on top to 850 nm on the bottom. The fringes are caused by the interference between the two telescopes. The larger scale inhomogenieties are due to the intersection of the combined speckle patterns of the two telescopes.

5. ALGORITHM DEVELOPMENT

The development of algorithms for image reconstruction and image analysis has continued to be one of the major components of this work. All of our previous work had been based on Labeyrie's original power spectrum analysis (or equivalent autocorrelation analysis for fainter objects), including our experiments with Worden's "self-calibrating" methods. It is generally conceded by all (even advocates of "phaseless" image reconstruction methods) that some image phase information is necessaray for the complete and unambiguous recovery of an image from speckle data.

Since we have, for convenience in image processing and efficiency of detection and data processing, divided our work into two categories depending upon source brightness, we have correspondingly divided our image recovery efforts into direct analog methods for application to bright objects for which atmospheric statistics dominate (or are comparable to) the photon statistics, and photon-by-photon event address methods for faint objects for which photon statistics dominate. The analog methods rely heavily (but are not limited to) Fourier transform methods. The faint object methods use autocorrelation or other discrete event image-plane techniques. All of the significant progress during this contract interval has involved the analog methods. However, we have implemented the rudiments of a photon-by-photon image phase retrieval scheme.

In many instances it is possible to interpret power spectra (or autocorrelation functions) directly in order to parameterize models of the corresponding source object intensity function. These techniques have been particularly useful in the interpretation of our asteroid measurements.

Since high-speed digital signal processing systems such as described in Section 4.3 are not yet available to us, it has been necessary, at considerable overhead in programming, to break down these complex algorithms into a form that can execute (however slowly!) on available minicomputer and micorprocessor systems. (Access to the KPNO cyber and the University cyber systems has been severely limited due to limited funding).

5.1 Photon-by-photon Image Phase Retrieval

As noted in Section 4.3, the Knox-Thompson algorithm requires phase integration which may be accomplished by integrating X- and Y- shifted quantities given by expressions 4.3 and 4.4. In the photon limited case the n-th specklegram, eq. 1.1, becomes

$$i_n(L) = \sum \delta(L - L_i) \qquad (5.1)$$

where $\{L_i\}_n$ = the list of photon addresses (x_i, y_i) for the n-th frame. The discrete Fourier transform of this is

$$I(K) = \sum \exp\{(2\pi i/N)(K-1)(L-1)\}\ I(L) \qquad (5.2)$$

The desired quantities to be integrated (4.3 and 4.4) are of the form, for shift s,

$$Q_s(K) = I^*(K)\ I(K+s). \qquad (5.3)$$

The inverse Fourier transform of this is

$$q(L) = \sum \exp\{(-2\pi i/N)(K-1)(L-1)\}\ Q(K), \qquad (5.4)$$

which is an image-plane expression reducing to

$$q(L) = \sum \sum \exp\{(2\pi i/n)(K-1)[L'_n - (L-1)]\} \times \exp\{(2\pi i/N)\ s\ (L'_n - 1)\}. \qquad (5.5)$$

This reduces to the autocorrelation-function-like quantity

$$q(L) = N \sum \exp\{(2\pi i/N)\ s\ (L'_n - 1)\} \times \delta(L'_n - L_n - L + 1), \qquad (5.6)$$

i.e. the autocorrelation function with a complex modulation term.

Since none of the computational resources available to this project have sufficient main memory necessary to accumulate (random access) the three arrays, i.e., the autocorrelation function (real) and the x- and y-shift phases (complex), for even a minimal 128 x 128 pixel format, one of us (EKH) has obtained private funds to implement this on a Motorola MC68000 based microcomputer system equipped with 0.5M-byte memory, 16 Mbyte Winchester disk and a 9 track magtape drive for data transport from and back to Steward Observatory. It executes slowly! A complete reduction, including accumulation of autocorrelation function and phase-shift arrays, for a 10 minute observation of a bright asteroid requires approximately 20 hours (still the factor of 100!). Nevertheless this system is permitting an investigation of discrete photon image phase retrieval methods.

5.2 Shift-and-Add Methods

These algorithms utilize from one to all of the speckles in a single specklegram to obtain a "mean" speckle for that particular specklegram. The average of these "mean" speckles over a number of specklegrams is then taken to represent diffraction-limited information which, in certain circumstances, can be considered to be a high resolution image of the object irradiance. A simplistic model for a specklegram is that it is the sum of a number of discrete speckles. If we let p(x,y) be the profile of a point source speckle then the specklegram can be considered to be the convolution of such a profile with an impulse distribution Imp(x,y). Thus, for a point source, the observed intensity can be written as

$$i(x,y) = p(x,y) * Imp(x,y) \qquad (5.7)$$

where * represents convolution.

Now, for a resolved object we can consider each speckle to be the convolution of the point source speckle with the resolved object irradiance o(x,y). Therefor the specklegram of a resolved object can be written as

$$i_n(x,y) = [p(x,y) * Imp(x,y)]_n * o(x,y). \quad (5.8)$$

Thus if we look at both a resolved and an unresolved object we can obtain a "mean" speckle for each. The "mean" speckle of the former is considered to be the convolution of the point source "mean" speckle with o(x,y). By deconvolving the resolved object "mean" speckle with the point source "mean" speckle the object irradiance o(x,y) can then be recovered. This approach was first applied by Lynds,Worden & Harvey (1976).

In order for this approach to yield results it is essential that the individual speckles in a specklegram should have well defined maxima. If this is not so, then the "mean" speckle would blur out the diffraction-limited information and thus would not be of use.

This analysis is also limited to bright object data where individual bright analogue speckles are visible. On the Steward system this translates to objects with apparent magnitudes less than approximately m=6 to 8 depending upon seeing and observing bandwidth.

We have implemented algorithms for two variants on this simple shift-and-add (SAA) idea, and developed two derivative methods, weighted shift-and-add (WSA) and deconvolved shift-and-add which have the further advantage of "flattening" the seeing-noise background upon which all shift-and-add results are superimposed.

5.2.1 Simple Shift-and-Add

This analysis was first proposed by Bates and Cady (1980) and consists of locating the brightest speckle within a specklegram and co-adding on a specklegram-by-specklegram basis. This is the most straightforward of the analyses implemented. In this case, the impulse function is simply a unit delta-function located at the position of the brightest speckle, which in turn is defined to be the local maximum of the specklegram. In order to suppress effects of Poisson noise (photon statistics), we have implemented various filter functions which may be applied to (convolved with) the individual specklegrams before further processing.

One of the major drawbacks of this form of analysis is that only one speckle per specklegram contributes to the final image. A variation on this technique developed by Bagnuolo (1982,3) to

include more signal from each specklegram has also been implemented. SAA analysis has the advantage of its simplicity but has the disadvantages that (i) the brightest pixel can be due to a noise spike (ion event) (ii) the brghtest pixel could be saturated and therefore not linearly related to the object intensity and (iii) more specklegrams are required to reach the same signal-to-noise ratio (S.N.R.) produced by Bagnuolo's technique. The Bagnuolo technique therefore appears to be the SAA method of choice.

5.2.2 Weighted Shift-and-Add

The S.N.R. can be increased tremendously if the majority of speckles in a specklegram can be used. This was the advantage of the Lynds,Worden & Harvey (1976) method, hereafter refered to as LWH. In their analysis of Alpha Orionis they created an impulse function to represent the distribution of the speckles in an individual specklegram, thus obtaining Imp(x,y) in equation 5.8. This was then cross-correlated with the original specklegram to produce a "mean" speckle p(x,y) for that particular specklegram. Their impulse function comprised a set of Dirac delta functions of uniform height. Thus all the speckles contributed the same weighting to the the "mean" speckle. The actual algorithms used to create p(x,y) in fact calculated the cross correlation between the speckle and impulse frames so as to avoid the problems of small number divisions in the complex quotient of the deconvolution process.

This technique however proves to be non-linear because of a thresholding of the data to locate only the brightest speckles and also because of the uniform impulse distribution Imp(x,y). In order to avoid these non-linearities it was decided to weight the impulse distribution by setting the amplitude of the delta functions to that of the speckle which they represented. Thus all the speckles in the specklegram were being utilized thereby increasing the S.N.R. compared to the SSA technique. This defines our Weighted Shift and Add (WSA) method.

5.2.3 Formal Analysis of WSA Method

A statistical analysis of the Weighted Shift and Add method has been undertaken to determine the expected mean speckle profile for the single point source case, for the multiple point source case and for the extended point source case. Further analysis to determine the extent to which the "overlapping of speckles" degrades the results of WSA data has also been attempted. The tentative results of this analysis are reported.

WSA Profiles

In all the cases discussed below, a standard technique has been employed to compute the expected WSA profile. We estimate the WSA profile by an extrapolation of the method Hunt, Fright and Bates (1982) applied to the analysis of the simple shift-and-add

algorithm (SSA). In the WSA case the shifting is done on all the speckles in a specklegram and not just the brightest. Simply then, to obtain to the WSA profile the expectation of the SSA result subject to models of the speckle intensity statistics is calculated. Therefore the expected WSA profile $\Omega(x)$ can be written as:

$$\Omega(x) = \sum_{i=1}^{N} \int_{0}^{\infty} s(x)\, \eta_i^2(x) p(\eta_i)\, d\eta_i \qquad (5.8)$$

where $s(x)$ is the SSA profile, represents the intensities of the N speckles in the specklegram,

$$p(\eta_i) = (1/\langle I \rangle) \exp\{-\eta_i/\langle I \rangle\} \qquad (5.9)$$

is the probability density for the intensity, and $\langle I \rangle$ is the average speckle intensity for the frame.

For the point source case the SSA profile was found to be:

$$S(x) = 2\langle I \rangle + [R_s(x)/\langle I \rangle^2] (S_{max} - \langle I \rangle) - S_{max} \qquad (5.10)$$

where S_{max} is the intensity of the brightest speckle found in the specklegram. $R_s(x)$ is the autocorrelation of the speckles and is independent of individual speckles under the assumption that the speckle process remains constant with time. $R_s(x)$ is related to the complex coherence factor $\mu_A(x)$ by the expression:

$$R_s(x) = \langle I \rangle^2 [\, 1 + |\mu_A(x)|^2] \qquad (5.11)$$

where:

$$0 \leq |\mu_A(x)| \leq 1$$

After some simplification eq.(5.8) reduces to:

$$\Omega(x) = 4 N \langle I \rangle R_s(x) - 2 N \langle I \rangle^3 \qquad (5.12)$$

The above equation reveals that the WSA profile will be the autocorrelation of the mean speckle of the data set with a constant, proportional to the average background, subtracted off. A comparison of the results of the SSA algorithm and the WSA algorithm reveals that the signal to noise ratio for the WSA algorithm grows faster than for the SSA algorithm. If we substitute $\langle I \rangle^2[1+|\mu_A(x)|^2]$ for $R_s(x)$ in the results for both the SSA and WSA procedures, and if we associate $|\mu_A(x)|$ with the signal, then

$$SNR_{SSA} = [(k-1)/2]\, SNR_{WSA}$$

where $k = S_{max}/\langle I \rangle$ for $k > 1$.

Thus the WSA algorithm is found to be superior, i.e. $SNR_{SSA} < SNR_{WSA}$, if $k<3$. By a simple application of the

exponential speckle intensity statistics defined by (5.9) above (Dainty and Greenaway, 1979), we find that the probability that the intensity of a single speckle equals or exceeds three times the average intensity is only 0.049, and even allowing for the large number of speckles in a specklegram, this is still a very small probability. Thus we can conclude that WSA is almost always a better algorithm than SSA, i.e., when seeing > 1".0.

If the object is a multiple point source object with the positions of the components located by the T vectors η_k then the SSA profile is found to be:

$$S(x) = \sum_{k=1}^{T} S_k(x_k)$$

where $S_k(x_k)$ is given by 5.10 with $x_k = x - \eta_k$, i.e. the single speckle autocorrelation response $R_s(x_k)$ is placed at each of the source component positions with its appropriate maximum speckle amplitude $S^{(k)}_{max}$ and average speckle intensity $\langle I_k \rangle$. Substituting this summed quantity S(x) and doing the WSA profile calculation leads to

$$\Omega(x) = \sum_{i=1}^{T} \sum_{k=1}^{T} N \left(\langle I_i \rangle^2 / \langle I_k \rangle^2\right) \times \left[4 R_s(x - \eta_k - \eta_i \langle I_k \rangle - 2 \langle I_k \rangle^3 \right] \quad (5.13)$$

If we define a T-component point source to be composed of T-speckles then the WSA profile will have maxima at the same places as a regular autocorrelation of a frame of a multiple point source object although the amplitude of the profile at each maxima will be

$$N \langle I_i \rangle^2 \left[4 R_s(x - \eta_k - \eta_i) \langle I_k \rangle - 2 \langle I_k \rangle^3\right] / \langle I_k \rangle^2 \quad (5.14)$$

where $R_s(x')$ is the mean autocorrelation of the speckles of a component. Since the WSA multiple point source result is just a superposition of the WSA result for the point source case, the advantages of WSA over SSA for the multiple source will correspond as well. Note particularly that, although a response is produced at each of the coordinates corresponding to the image autocorrelation function, the Amplitudes are asymmetric (unlike the case for the autocorrelation function). Thus image phase information is preserved.

Work on the statistical analysis for extended objects is still in progress at present. We are studying, initially, the special case in which a speckle is characterized by a single local maximum, i.e.the case for a bright star surrounded by a resolvable atmosphere.

Degradation of Data by Overlapping of Speckles

Up to this point no attempt has been made to determine how much speckle interferometric data is degraded by the overlapping of adjacent speckles. To that end a first order statistical model of the number of overlaps was attempted. Unfortunately,

though, the model developed has been found to be rather cumbersome in use. Because of this a newer model is in preliminary stages of development.

5.3 Deconvolution and Holographic Methods

Implicit in deconvolution and holographic methods is some technique for sampling the instantaneous speckle modulation transfer function (MTF), the quantity which is averaged to produce the second term in eq. 1.2. In our work we have experimented with two methods for obtaining this information which use variants on speckle interferometry made possible with the differential speckle camera. If the object is essentially unresolved in one wavelength and well resolved in an adjacent wavelength (i.e. the continuum near an emission or absorption feature vs a sample centered on that feature), or if the observation can be arranged so that a sufficiently bright, unresolved source is in the field, then a complex deconvolution consisting of the complex quotient

$$O'(u,v) = \langle I_n(u,v;r) \,/\, I_n(u,v;u) \rangle, \qquad (5.15)$$

where $I_n(u,v;r)$ and $I_n(u,v;u)$ are respectively the complex Fourier transforms of the n-th specklegrams for the resolved and unresolved components obtained simultaneously, yields a useful approximation $O'(u,v)$ of the desired complex object intensity distribution upon averaging a sufficient number of observations. Quite surprisingly, there appears to be no "division by small numbers" problem with this quotient.

There is, however, a crucial detector distortion problem in this method using our present intensified video camera. There is sufficient geometrical distortion (principally "pincushion") that it is necessary to correct the data frame-by-frame. We have implemented a simple grid re-mapping algorithm which is calibrated by observing a calibrated, square-grid reticle in the speckle camera (telescope) focal plane.

Because of the complexity of these computations, and the need for multiple arrays (some of which are complex) in main memory, this program is implemented in several sub-steps, in part on the Steward Observatory Eclipse (raster extraction and re-mapping) and in part on the KPNO Cyber (the complex deconvolutions - see section 6.8 and Figure 6.22).

5.4 Differential Speckle Interferometry

In addition to the method of complex deconvolution described above in section 5.3, further algorithms for reductions of DSI data have been implemented, primarily for faint object work, on the Steward Eclipse system. The principle reduction method requires the averaged cross-correlation of the DSI specklegram pairs. This is conveniently accumulated as a windowed autocorrelation function treating the specklegram pair as a

simple specklegram of an "artificially binary" object. The window is centered on the "binary separation" corresponding to the instrumentally induced image separation. Further refinements allow accumulation of separate results corresponding to different polarization states.

5.5 Model-fitting and Statistics

The limitations of PS or ACF information are in many applications very serious. These functions have the attributes of a) preserving size information up to the (possibly filtered) diffraction limit of the telescope but b) scrambling that information in a radially symmetric way (because of the loss of image phase information). Clearly it is desirable to analyze a restored image, but in many instances that is not yet feasible. Therefore, we use model-based analyses of PS or ACF data to extract parameters characteristic of some appropriate mathematical representation of the image of the object measured by these functions. Generally we begin by making simple assumptions about the object, fitting the corresponding simple model and examining the residuals to the fit in order to attempt a refinement of the model.

Our methods for least squares fitting are based on the general methods applicable to a wide class of nonlinear problems described by Jefferys (1980,1981). Analytic functions are "linearized" by a first-order Taylor expansion and iterated until the solution for the model parameters converges. The Jefferys method also allows for simultaneously imposing an additional equation of constraint upon the model parameters, although we have not used this capability. Non-analytical functions (that is, any function which can be tabulated) can be fit by approximating the first derivative by the first tabular difference. The method is complete, including the full covariance matrix for evaluating the validty (error analysis) of the fit. Our present implementation includes this covariance analysis, but does not include individual weights for each data point - all data points are weighted equally in our present implementation of this analysis on the very small computers presently available to this project.

Since Speckle Interferometry PS and ACF results are radially symmetric, a simple procedure (but possibly physically misleading - the results must be interpreted with great care) is to implement fits of radial functions of the form

$$F(r) = A\, f(r|p(a)) + B \qquad (5.16)$$

where p(a) is a single size parameter in the one-dimensional case or a set of three parameters (x-scale, y-scale and position angle in the two-dimensional case. Useful forms for f(r) which we have implemented are: (5.17)

1) $f(r) = e^{(r|p(a))^2}$ Gaussian $\sigma = p(a)$

2) $f(r) = e^{(r|p(a))^{5/3}}$ "Seeing" - 5/3-law

3) $f(r) = \pi R^2 - r\sqrt{R^2 - r^2/4} - 2R^2 \arcsin(r/2R)$
= ACF of uniform disk of radius R=p(a).

4) f(r) = Averaged radial profile taken from data.

5) f(r) = cos(r|p(a))
= Binary star visibility: separation = 1/p(a)

6) f(r) = Airy(r|p(a))
= Airy function
= PS of uniform disk of radius p(a).

This technique is used in order to correct for the shape of the noise bias $n \langle|D(u,v)|^2\rangle$ (see eq. 1.3) produced by our detector which appears with a characteristic Gaussian shape in both the analogue and the old event thresholding photon detection methods (Hege et al. 1982a). Since the "physical object" in this instance is the brightness distribution at the output of the image intensifier consequent to detection of a photoelectron event, a Gaussian model fits rather well and leads to reasonable corrections for the noise bias in PS measurements.

6. IMAGE RECONSTRUCTION RESULTS

Image reconstruction and image retrieval efforts are still in very preliminary stages of investigation. In this section we summarize some of the experiments currently under way.

6.1 Fienup Method

Image reconstruction of the asteroids Eros and Herculina was attempted using Fienup's phaseless method. The data were noisy, and the objects were only marginally resolved, but the oblong shape of Eros and the effects of albedo variegations on Herculina are evident in the images, shown in Figures 6.1 and 6.2 respectively.

Figure 6.1 Eros reconstructed image. The contours are marked by intensity enhancements at each factor of two. The narrow dimension is just at the diffraction limit of the 2.3 m telescope.

These images were obtained by the Fienup method, with minimal start-up information, and used debiased, deconvolved, cleaned power spectra from event-mode data. Especially in Figure 6.2, effects of video digitization artifacts (the large horizontal artifact) are evident. Also, the Herculina data may have a residual power spectrum bias error (leading to the bright excess in the center), or this may be evidence of the inability of the Fienup method to properly allocate excess diffraction limited energy (e.g. due to bright spots, for which there is other, independent evidence). There is a hint of evidence of

albedo variegation commensurate with that required to appropriately model simultaneously the speckle autocorrelation functions and the lightcurve observed at the same epoch. Further refinements and experiments, using more data sets, are required to effectively evaluate the reliability of this method. However, the present results are encouraging in that these are our first reconstructions for 10^{th} magnitude objects using discrete photon-counting techniques.

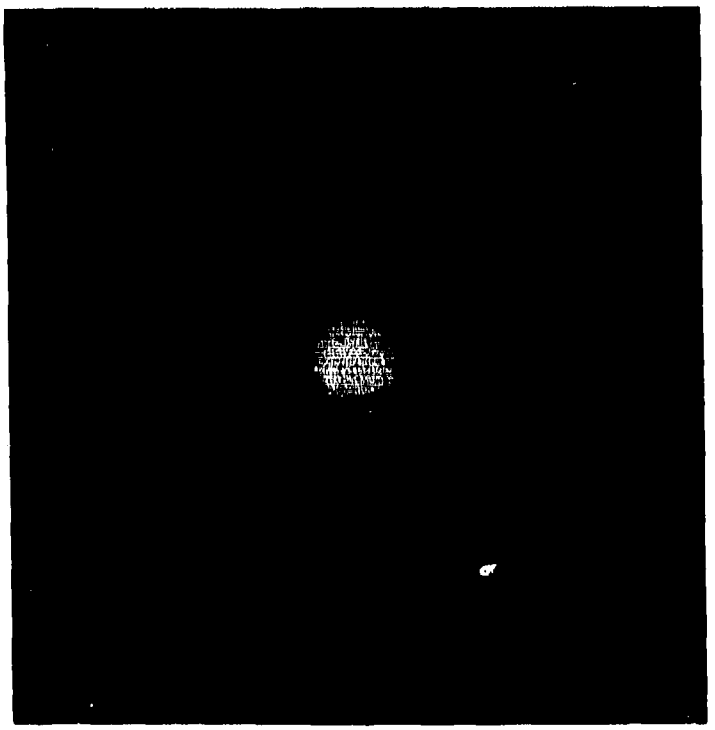

Figure 6.2 Herculina. (See text)

In related work, the use of the Walker (1982) method for image reconstruction has been investigated, but this method does not seem to work very well for our two-dimensional images. McCarthy has had some success, however, by combining the iterative methods of Walker and Fienup.

Cocke (1983) has also shown that Cauchy's inequality is an even stronger criterion than the Bochner-Khinchin theorem for use in further constraining these "phaseless" image retrieval methods. However, we have no results yet with this idea.

6.2 Simple Shift and Add

Three types of objects have been investigated by this technique, (i) a computer generated set of "triple star" simulated specklegrams, and real data for (ii) Supergiant Stars and (iii) Close Binary Systems.

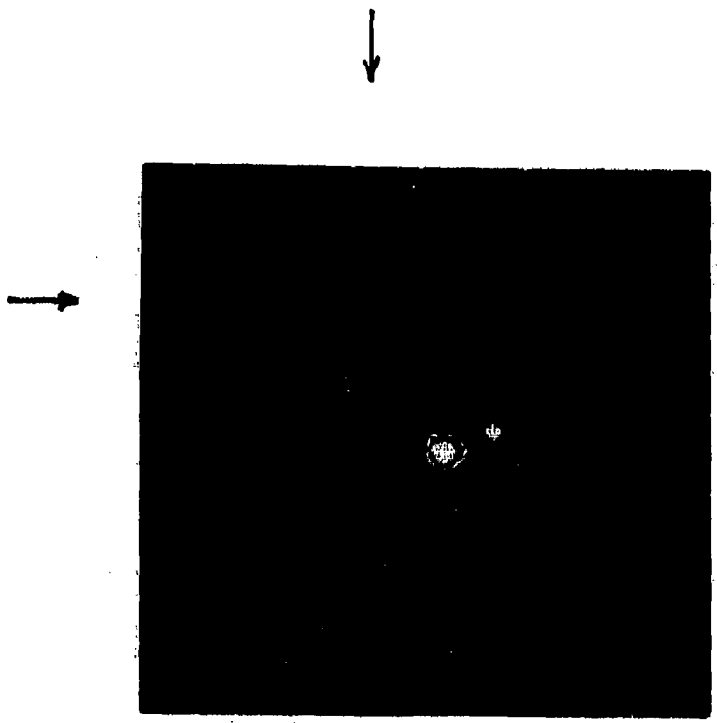

Figure 6.3 Triple star simulation. Simple shift-and-add. Third component response just at noise level, is marked by arrows.

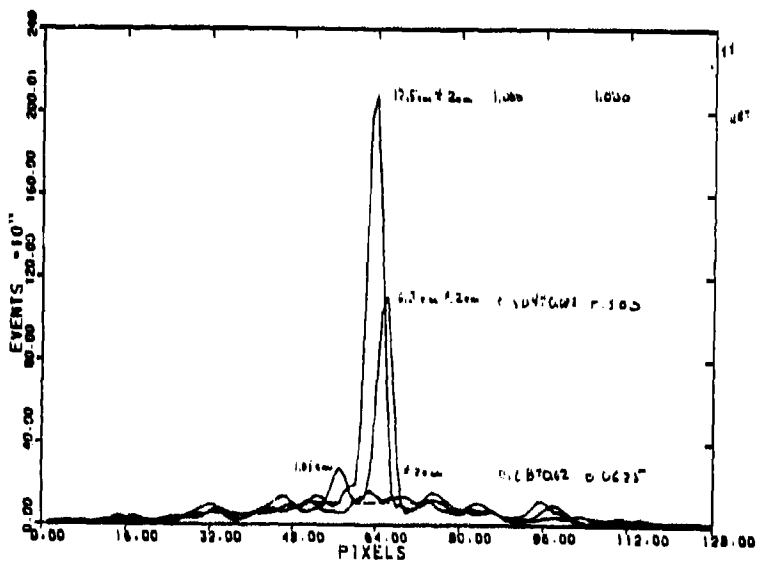

Figure 6.4 Horizontal cut through centers of expected responses in triple star simulation SAA result. The recovered intensity ratios are 1 : 0.504 : 0.08 compared to input 1 : 0.5 : 0.0625.

The first data set analyzed was a ten specklegram triple star noise-free simulation. The ratio of the three components was 1 : 0.5 : 0.0625. Figure 6.3 shows the reconstruction. The two brighter components are clearly visible with the correct separation and position angle. The third component, however, is lost in the noise of this process. This noise is introduced from the remainder of the specklegram when the whole specklegram is translated to put the bright speckle at the specklegram centre. As only ten specklegrams were used in this analysis there was not enough signal in the third component to bring it out. The measured ratio of the two brighter components is 1 : 0.504. Since the known input signal can be used to analyze the output, one can see that in fact there is a response at the position of the third component as shown in the cuts in Figure 6.4.

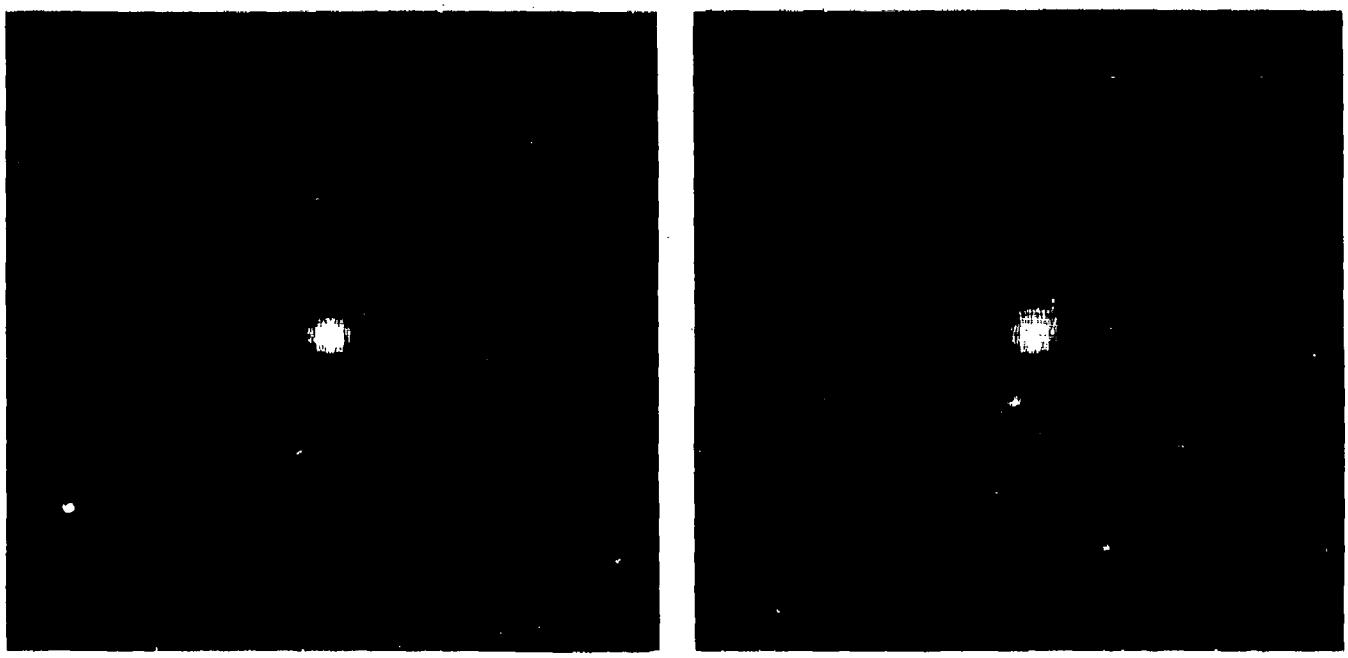

Figure 6.5 Shift-and-Add results for unresolved star (γ Ori left) and resolved star (α Ori right) at 422.7 nm using 2.3 m telescope.

The supergiants looked at are part of the Expanded Stellar Atmosphere program, the aim of which is to resolve the atmosphere of cool red supergiants by looking at the structure in the atmospheric emission lines, e.g. H_α 656.3, CaI 422.7 etc. One of the program objects is Alpha Orionis (M2 Iab) and one of the comparison stars for this object was Gamma Orionis (B2 III). Figure 6.5 shows the Simple Shift & Add (SSA) image of the latter. This shows the strong central maximum which is of the size of the diffraction limit of the telescope surrounded by the first Airy ring, showing that this object is a point source, superimposed on the strong "seeing" background produced from the overlap of the remainder of the translated speckle specklegrams.

Figure 6.5 also shows the SSA image for Alpha Orionis. Here the strong central maximum shows a larger size as would be expected for a resolved object. There is also some indication that the image is elongated.

In order to further reduce this data the "seeing" background must be removed. One way to do this is by modelling the background with a two dimensional Gaussian and subtracting it so that the central maximum lies on a flat background. Once this is done for both stars the complex deconvolution of Alpha Orionis with Gamma Orionis can be computed. See below for results of such an empirical seeing correction as applied to binary star data.

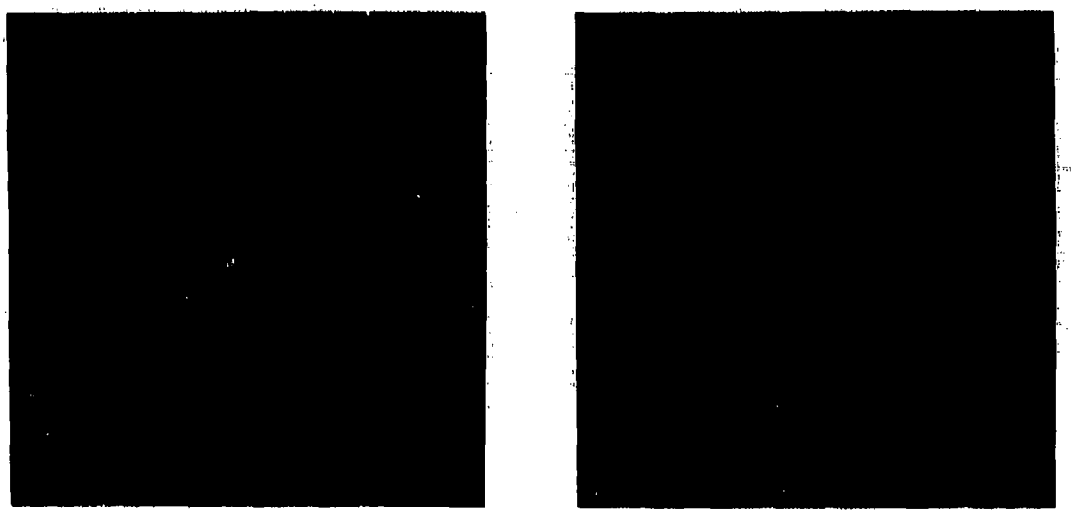

Figure 6.6 Capella by SSA. Left is raw result. Right is 12 paramerer model fit (see text).

Two close binary systems have so far been studied by this method, Alpha Aurigae and 115 Tauri, the latter being an occultation binary. Alpha Aurigae is a system composed of two G III giants of very similar magnitude. The SSA image of Alpha Aurigae is shown in Figure 6.6. It is interesting to see that this image suggests three components. This is due to the speckle statistics. Each speckle has two maxima, one for each component of the binary system. The brightness ratio of these maxima will be equal to that of the two components, modified by Poisson statistics. As the two components have similar magnitudes it is possible, occasionally, for the maximum due to the fainter component to be larger than the other. When this happens the third component of the SSA image is created. Thus, if a binary system comprised of two very nearly equal components (to within measurement limits) then the SSA image would be similar in form

to an autocorrelation and would therefore conceal the correct orientation of the system. However, for the more common unequal component case, the maximum due to the brighter component should occur much more frequently and, therefore, the correct orientation can be ascertained by looking at the brighter of the two secondaries of the SSA image. The ratio of the intensities of the two secondaries is therefore related to the magnitude difference between the two components, Bagnuolo (1982). Refering again to Fig. 6.6 it can be seen that the NW component appears to be the brighter. An estimate of the brightness difference can be made by removing the background from the SSA image. To do this a twelve parameter non-linear 2-D least squares fit was applied to the centre 30 square pixels of the image. The three peaks were modelled by gaussians and a gaussian "seeing" background sitting atop a tilted term (a*x+b*y+c*x*y) was also assumed. The central five pixels of the image were omitted in the fit because of the photon spike (noise bias). The intensity ratio of the two SSA secondary sidelobes was found to be r=0.66 which corresponds to a true binary star intensity ratio of f=0.80 when converting r to f according to Bagnuolo's (1982) statistical analysis. This model image is also shown in Figure 6.6.

Figure 6.7 Residual to SSA Model-fit to Capella.

The model did not take into account the Airy rings in the image and these can be clearly seen in the residual of the fit, Figure 6.7. Notice that these rings appear "lumpy". This non-uniform structure also shows up in Airy rings from other SSA images. The photon spike is clearly seen at the centre of the residual and represents the region not fitted by the model. The dark area immediately to the left of the central "spike" is caused by undershoot in the video analogue signal. This is

produced by the peaking circuit in the Video Cassette Recorder and cannot be removed in the digitizing process. This again emphasises need for high quality, distortion-free detectors with on-line read out to guarantee data integrity.

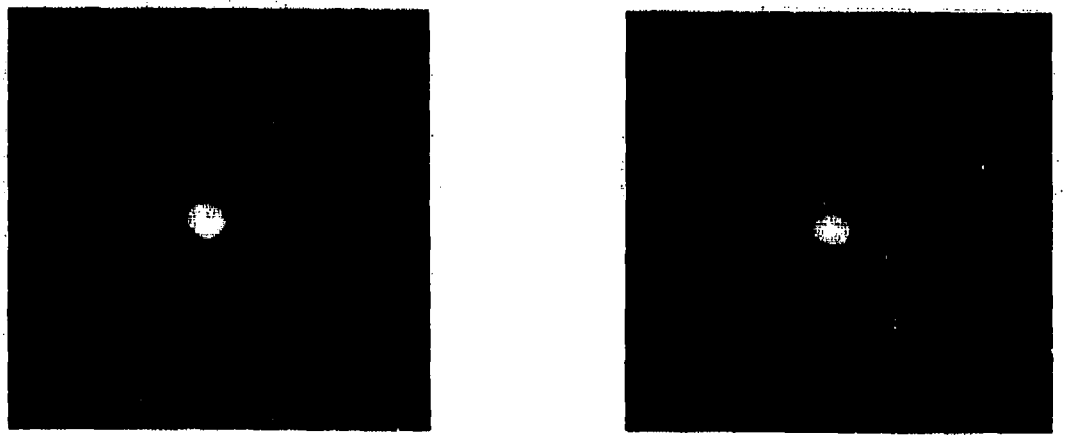

Figure 6.8 113 Tau (unresolved - left) and 115 Tau (resolved - right) by SSA.

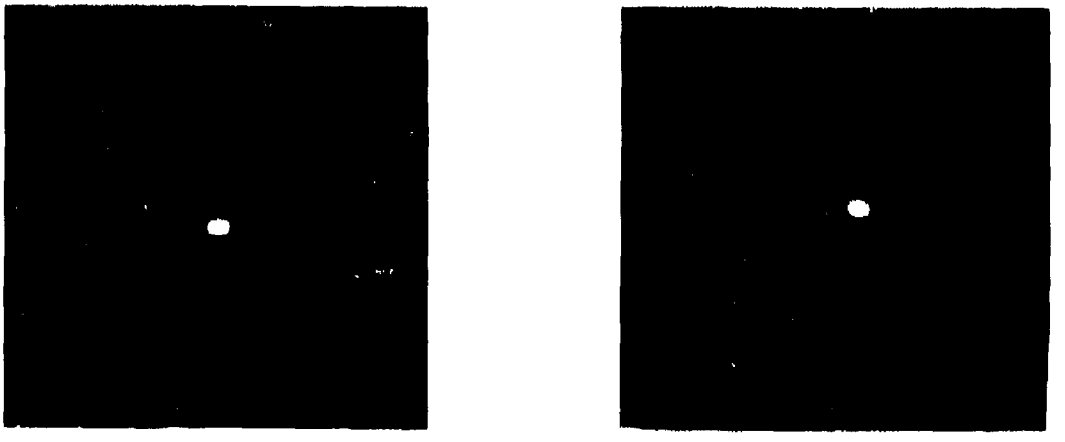

Figure 6.9 115 Tau deconvolution results from SSA after crude model-fit seeing correction. An "aperture" filter is required before the inverse transformation. Filter corresponds to telescope aperture (left) and to .7 x telescope aperture (right).

Figure 6.8 shows the SSA images for 115 Tauri and the comparison 113 Tauri. At the epoch of observation the separation of the two components of 115 Tauri was approaching the diffraction limit of the 2.3m telescope, as can be seen by comparing the images in fig. 6.8. The Airy ring is clearly visible in this image and the secondary component can be seen overlapping the Airy ring to the east in the resolved object. Notice a smaller blurring westward of the central peak due to the secondary. Note that for 113 Tauri no secondary peaks can be seen. The Airy ring in both images shows very non-uniform structure. This seems to be a characteristic of these data sets. Further analysis is required to tell if it is a statistical effect or a signature of the telescope OTF.

These two images were seeing corrected using a Gaussian model and then Fourier transformed. The complex quotient of the two was then computed and inverse transformed to produce a deconvolved "image", Figure 6.9. We can now see the two secondary peaks more clearly as the Airy ring has also deconvolved. The poor signal-to-noise ratio (SNR) of this data did not allow for a determination of the secondary peak ratio as only a few hundred specklegrams were used. There is no indication of a third component as earlier thought (suggested by "lumpy" Airy rings). The magnitude ratio is not correct, appearing to be greater in the deconvolved result than occultation measures show. This is probably due to inadequacies in the seeing model correction. We have not yet attempted Weiner-filter based seeing corrections using the data from the unresolved star to correct the image of the resolved star, as suggested by, e.g., Bates.

6.3 Correlated Shift-and-Add (DSI)

In this experiment, the brightest speckles which correlate at the known instrumental separation in each specklegram of the simultaneous DSI specklegram pair are chosen to define the shift positions for each component of the DSI pair. The SAA result is then accumulated separately for each component of the pair. This will then allow a comparison of the two results for which the seeing effects should be identical. An example for α Ori observed with the mica Fabry-Perot with two bandpasses 0.125 nm wide separated by 0.5 nm is shown in Figure 6.10. Both images show evidence for a faint, elongated cloud towards the south-east. The bandpass in the red wing of the line shows this effect to be weaker. We have not yet completed the analysis of this data (i.e. Weiner filtering, or complex deconvolution of the image taken on line center by that taken off-line).

Figure 6.11 shows a similar pair of Correlated SAA images obtained for the unresolved? (optically) star α Lyr (Vega). The curious elongation in the raster direction may be due to a bright-speckle video saturation effect - it is not verified. It does show (c.f Figure 6.10) an object with angular size smaller than α Ori.

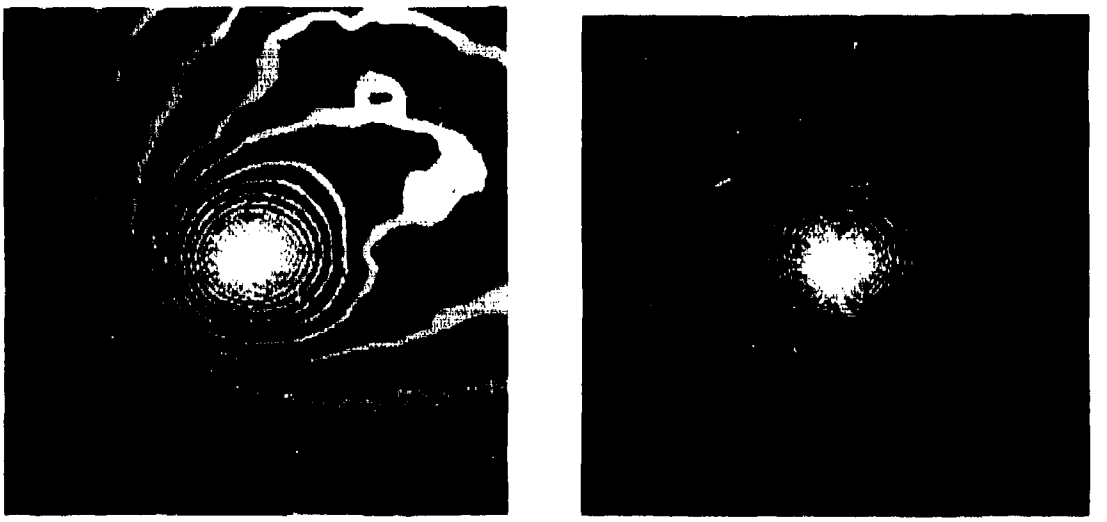

Figure 6.10 Correlated SAA Ori. Left - line center. Right - off line.

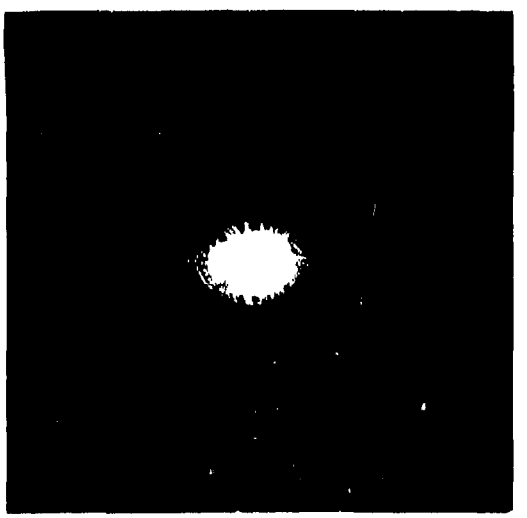

Figure 6.11 Correlated SAA. Vega.

6.4 Deconvolution and Cross-correlation Methods

A series of experiments to investigate methods for avoiding some of the problems with the original LWH method and to eliminate inherent non-linearities in methods requiring a threshold was conducted.

The algorithm to derive a set of weighted impulse functions for each specklegram was implemented to avoid problems with the LWH method when the cross-correlations between the derived impulses and true specklegrams were computed. This was first done for the ten specklegram triple-star simulation and the results can be seen in Figure 6.12. Notice that like the SSA image this also shows a triple peak for the two brightest components of the system. This is easily explained because the cross-correlation between the speckle and weighted impulse frames mimics an autocorrelation procedure. As in an autocorrelation a binary object will produce a triple response. What does make this cross-correlation differ from the autocorrelation is that a speckle cross-correlates with a delta function rather than itself so that the peaks in the cross-correlation are of the speckle size instead of twice the size as would be for the autocorrelation case. Thus, this cross-correlation is a type of "quasi-autocorrelation".

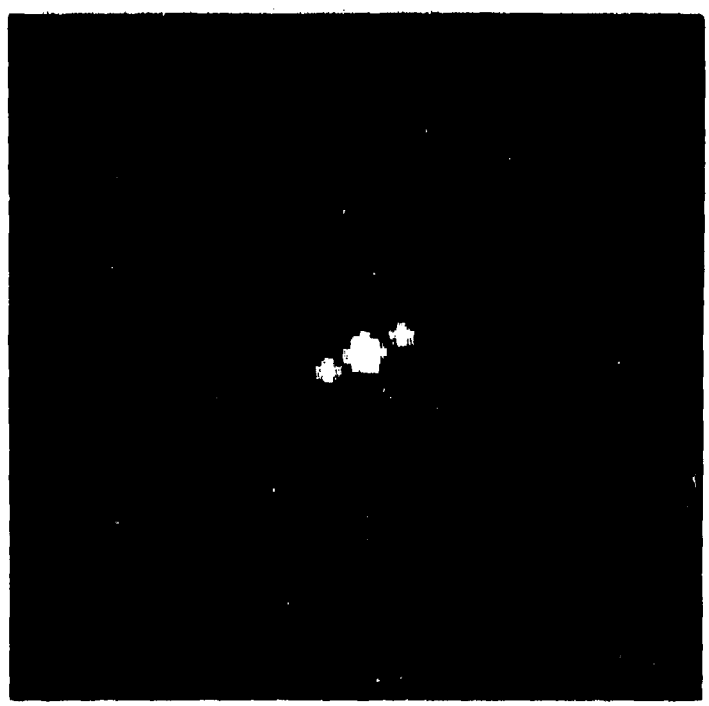

Figure 6.12 Triple star simulation. Weighted SAA (WSA).

Thus for the case of a binary system or any multiple system the ambiguities of the orientation which exist in an autocorrelation will also exist in the cross-correlation. However, for a resolvable single object, e.g. a supergiant, where there is only one maximum per speckle then the cross-correlation peak will represent the "mean" speckle for the specklegram. Notice in Figure 6.12 that there is a background which is due to the cross-correlation of a speckle with the delta function representing another speckle, therefore creating a "seeing" hump similar to that for the SSA and also in regular autocorrelation.

In order to use this weighted analysis on multiple system data so that the orientation information can be extracted, the impulse function was replaced by the square of itself before computing the cross-correlation. This has the effect of removing the amplitude symmetry in the "quasi-autocorrelation". Taking for example a binary star with components of brightness A1 and A2, respectively, then the secondary peaks in the "quasi-autocorrealtion" will have amplitudes each of A1*A2. However, when the impulse function is squared the amplitudes now become A1*A1*A2 and A1*A2*A2 respectively giving a ratio of A1:A2, the ratio of the actual brightnesses. Figure 6.13 shows the cross-correlation for the squared impulse distribution for the triple star simulation data. The amplitude symmetry is no longer present and the NE secondary is brighter, agreeing with the results for the SSA case as to the orientation of the system. Of course, if we have the case of identically equal components then this case too would degenerate into a "quasi-autocorrelation": no technique could recover an orientation if the two components had identical brightness. This could only be done if their spectral types were different, and observations would have to be made at wavelengths chosen to emphasize the difference. Analysis shows that the original intensity ratio is preserved in the ratio of the sidelobes (secondary to tertiary) and that the orientation is given by the orientation of the secondary with respect to the primary. Thus, unlike strict (or "quasi-) autocorrelation, this non-linear method <u>preserves essential phase and amplitude information for binary star research</u>.

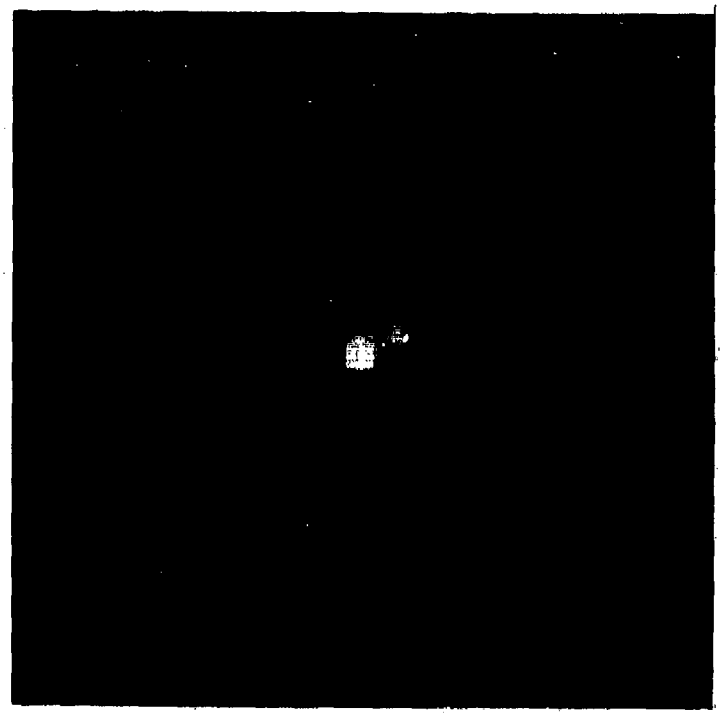

Figure 6.13 Squared Impulse WSA for Triple Star simulation. The phase and relative amplitudes are preserved for a binary system.

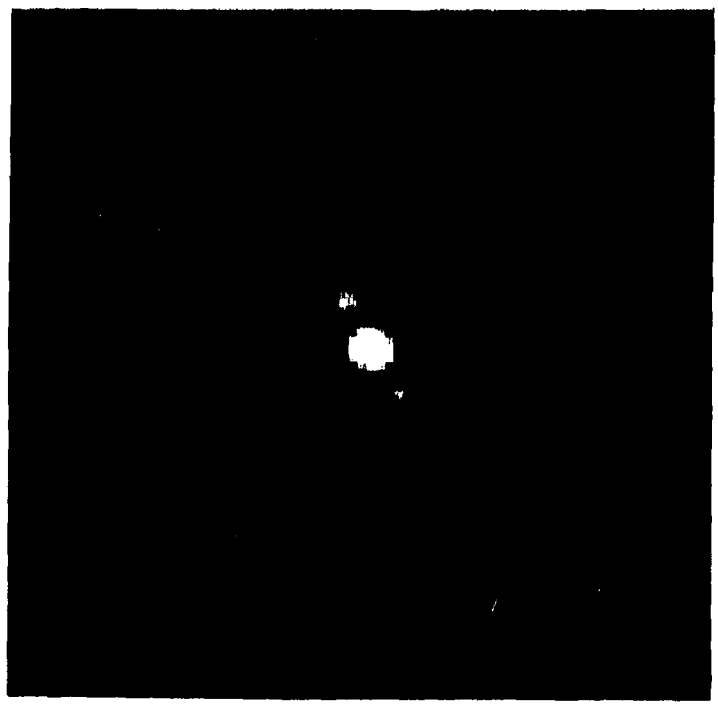

Figure 6.14 Capella by Squared Impulse WSA.

Figure 6.14 shows the squared impulse Weight Shift and Add (WSA) image of Alpha Aurigae. Note that the NW secondary in this image is the brighter, indicating the orientation which agrees with the SSA image. The Airy rings due to the telescope are clearly visible around all three peaks and all three sit atop a seeing "hump". There is a marked similarity in the WSA and SSA results. This could be fit in the same manner as the SSA image to obtain the secondary peak ratios and therefore the brightness ratio between the two components. Further work is required to investigate the limits of precision of this method.

An alternative to computing the cross-correlation is actually computing the full complex deconvolution. This is done by using just the regular impulse function as opposed to the squared impulse function. The full complex FFT of both the specklegram and the impulse frame are computed and the complex quotient is calculated (similar to eq. 5.15, although this does have a "small numbers divide" problem). These are summed to provide the average deconvolved object transform. This is then inverse transformed using an FFT to give the full deconvolution.

For every speckle maximum in a specklegram there will be an impulse with a corresponding weight. From equations 5.7 and 5.8 it can therefore be seen that the deconvolution will give the "mean" speckle for the specklegram. In fact this will be the mean speckle maximum. If the object is a binary system with both components unresolved, then each speckle will have two maxima and therefore each speckle will be represented by two impulses. The deconvolution will then remove all duplicity giving a single peak. This is not the desired result! Thus as a method for studying multiple systems the deconvolution version of the Weighted Shift-and-Add (D/WSA) needs some modification. However for a point source or single resolvable source meeting the requirements set out in the introduction, specifically, that individual speckles are characterized by a single maximum, this technique should produce a well defined "mean" speckle. An advantage to this form of analysis is that all speckles are deconvolved with their respective impulses. This places the mean speckle at the origin (centre) of the specklegram. Thus there is no "seeing" background, unlike both the SSA and WSA. This therefore allows a better determination of any intensity information as the background does not have to be fitted and removed. In fact, this is a "seeing" independant technique which only depends upon the existence of speckles with such specific properties.

Figure 6.15 is the deconvolved WSA (D/WSA) image for the triple star simulation data set. Notice the bright central maximum and the flat background. As expected no other structure is significant. Figure 6.16 is also a D/WSA image but this time the impulse frame was generated from a smoothed specklegram. The original specklegram was smoothed with a low pass filter to "blur" the maxima from the two brighter components to produce just one maximum. This filtered impulse frame was then deconvolved with the original specklegram. The sum of ten of

these providing the image. The secondary component is now clearly visible with the correct orientation, separation and ratio of the two intensities. The flat "no-seeing" background is apparent.

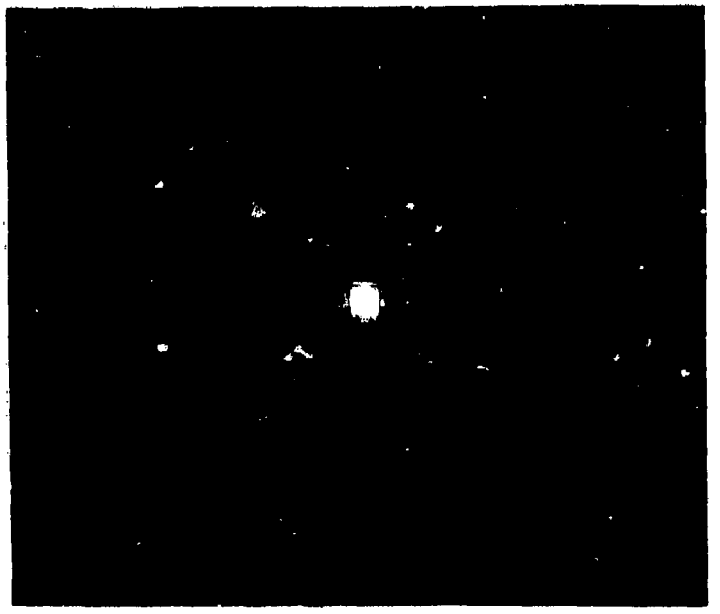

Figure 6.15 Deconvolved WSA image for triple star simulation. The most notable feature here is the "flattened" seeing background.

Figure 6.16 Filtered deconvolved WSA for triple star simulation. Note that now the phase and relative intensity are preserved. Filtering forced the speckles to have only a single maximum.

Another way to enable this routine to work for multiple systems is to edit the impulse function. The regular Labeyrie autocorrelation or SSA analysis determines the spatial information about the object, i.e. its separation and position angle. For a binary system the two components produce two maxima for each speckle giving two impulses for each speckle. Knowing the spatial information it is then possible to look for impulse pairs with the same vector separation. Either the left or right impulse from the pair can now be edited out of the impulse frame and the deconvolution calculated. Figure 6.17 shows the effect of doing this for the triple star simulation. The secondary is noticable although there is more structure in the otherwise flat background since only one half of the impulses are now used. As for all of the reconstruction tests for this data set the tertiary component is lost in the noise of the background and is not visible.

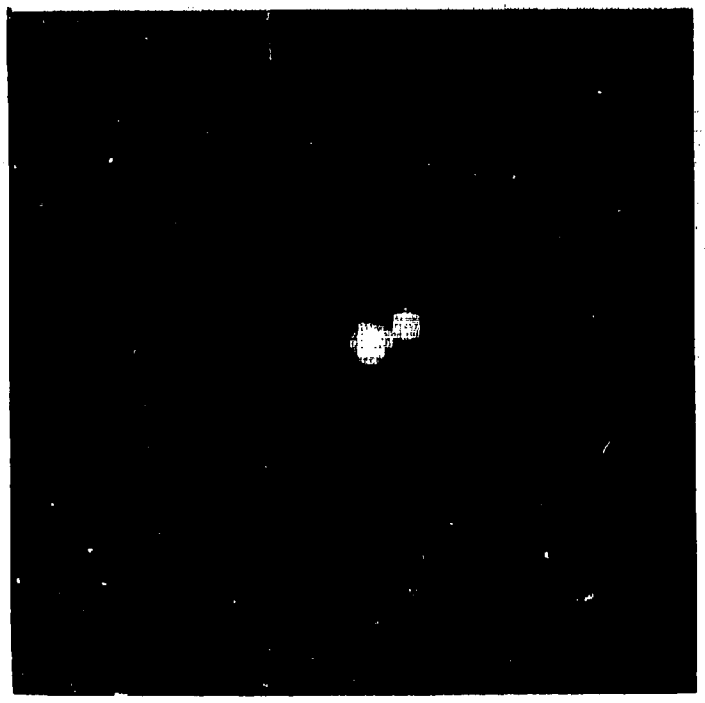

Figure 6.17 Edited deconvolved WSA for triple star simulation. Again the orientation and relative magnitudes are preserved, but the background is noiser since only half of the speckles are used.

Figure 6.18 shows the D/WSA image for the unresolved star Alpha Lyrae. The flat background is very much in evidence as well as the Airy ring. The N-S and E-W structure in the image background are effects of the numerical deconvolution, probably of digitization artifacts, and need to be investigated further. The SE-NW striping is also an effect due to the deconvolution and represents the transform of a couple of anamalously bright pixels in the quotient (the "small numbers divide" problem). In order

to fully utilize this technique the quotient problems have to be eliminated. One way of doing this is currently under test. This involves looking for outlier pixels in the complex quotient. If a pixel has a value which is greater than two sigma from the mean of the eight surrounding pixels then its value is replaced by the mean of the surrounding pixels. Unfortunately this involves extra overhead in the already slow and cumbersome analysis routines, and faster and more efficient means of performing this outlier rejection algorithm are only feasible with array processor systems.

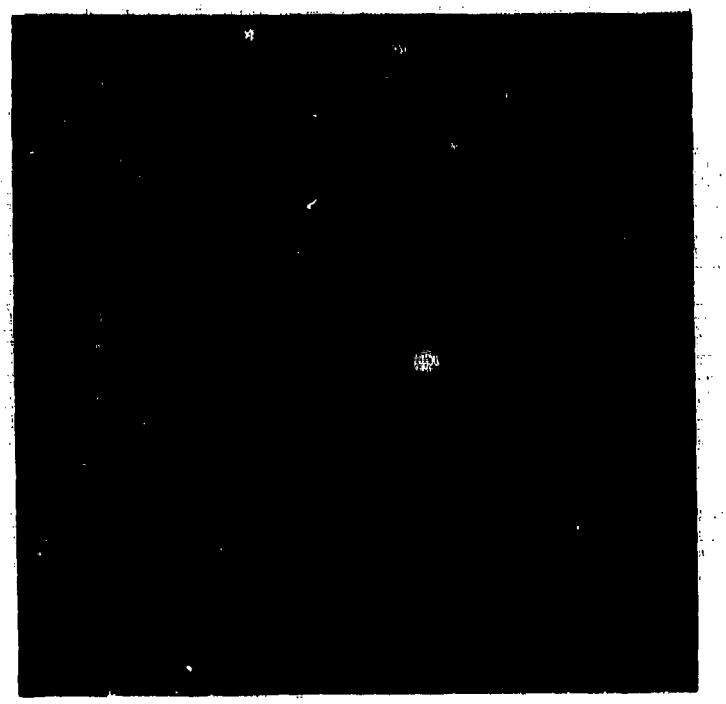

Figure 6.18 Alpha Lyrae by deconvolved WSA showing unresolved object on flattened background.

These demonstrations with both real and simulated data sets suggest that this method for producing seeing-corrected deconvolved images from specklegrams of bright objects holds great promise. Further work is required to ascertain whether these methods are extensible to fainter objects where a speckle maximum is only definable as a local maximum in a generally quite sparse photon distribution.

6.5 Holographic and Differential Deconvolution Methods

The differential speckle camera was used to record simultaneous specklegrams of α_1 and α_2 Sco. Since α_2 Sco is a fainter B-type companion to α_1 Sco, it can be used as a holographic reference for a complete image reconstruction of α_1 Sco. In order to balance the relative intensities of these objects, we placed a neutral density filter in front of the

intensified video camera (speckle) focal plane so that it just intercepted the image of α_1 but not α_2. The simple SAA results for both objects were accumulated separately, and the results are shown in Figure 6.19. We have not yet completed the comparative analysis of these images, but the resolved nature of α_1 Sco, and possibly evidence for extended structure, is clearly seen. Initial efforts to perform the holographic deconvolution using eq. 5.15 were not convincing due to insufficient data to produce a good SNR. (The statistics in the quotient are, of course, limited by the fainter object). A longer integration should produce good results.

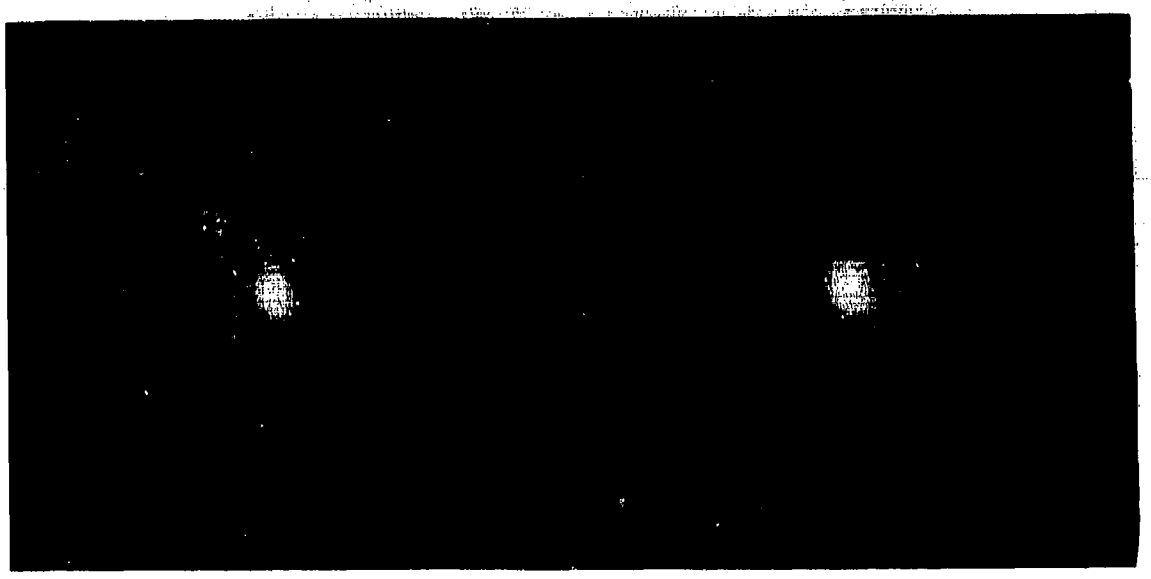

Figure 6.19 Simultaneous SSA results for α Sco. α_2 Sco left. α_1 Sco right.

Better results have been achieved with the two band-pass DSI approach. Figure 6.20 shows results for α Sco obtained by the integration 5.15 applied frame-by-frame to DSI data in which the Fourier transform of the data on line center is divided by the data off line for which α Sco is only partially resolved. In order to restore an image which should more nearly represent the true appearance of the object, the integrated quotient transform was multiplied by the Fourier transform of a uniform disk of the size corresponding to the continuum disk size of α Sco from conventional speckle interferometry. This may not be exactly correct, as α Sco may not be a perfect, symmetric uniform disk in the continuum. The results are nevertheless encouraging, and show definite evidence for an elongated gaseous envelope.

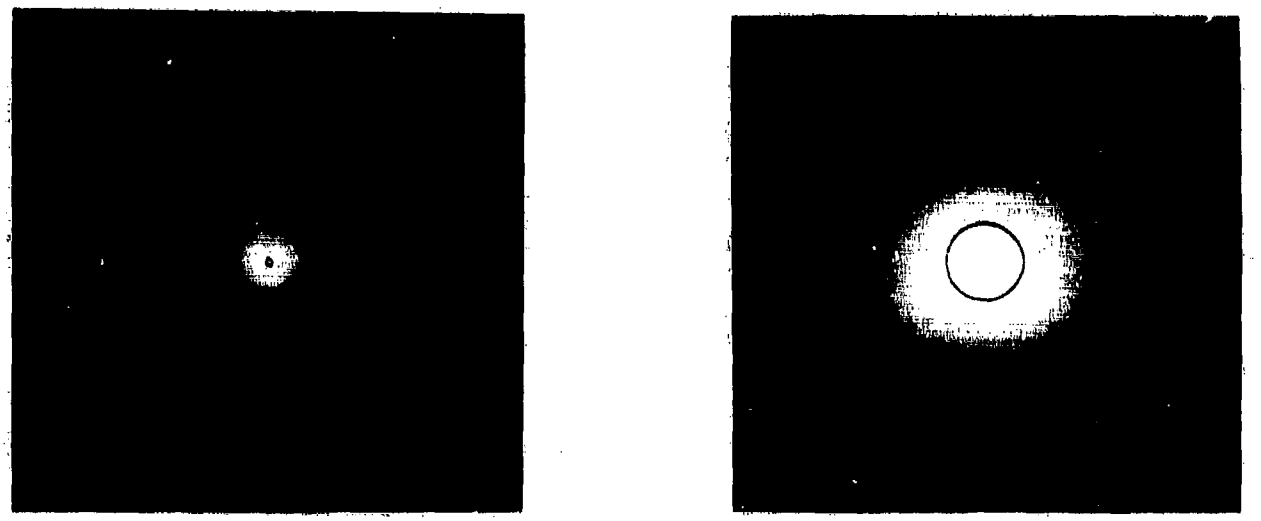

Figure 6.20 DSI Holographic Deconvolution of α Sco (right). The superimposed circle represents the continuum disk size. The results for α Lyr (left) are shown for comparison.

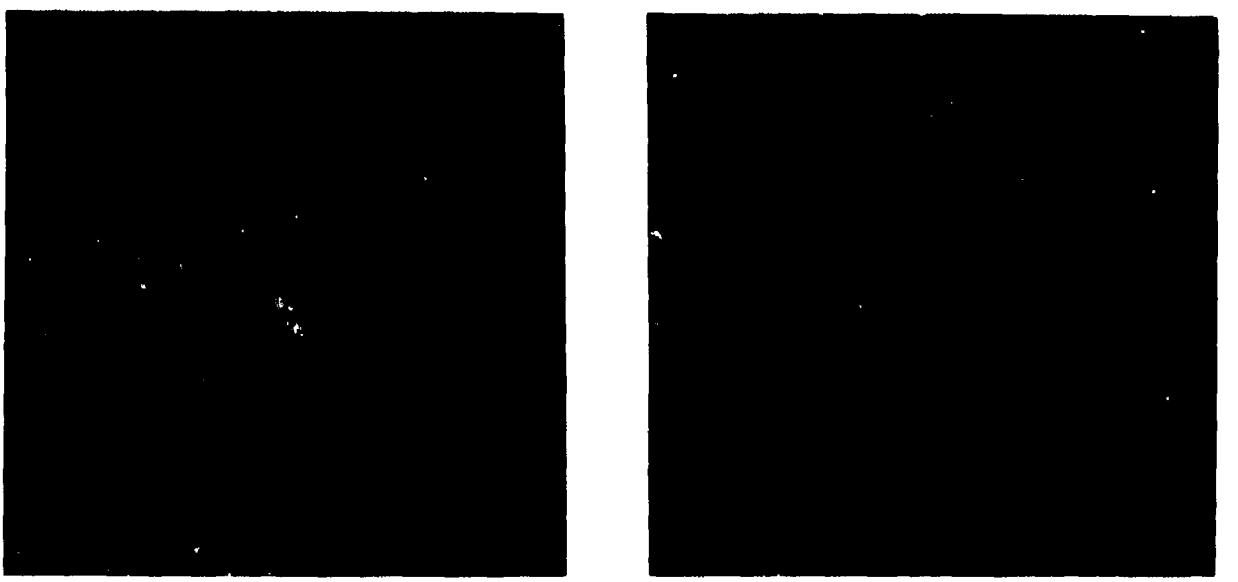

Figure 6.21 Triple star image reconstruction. Knox-Thompson (left) and phase unwrapping (right).

6.6 Other Direct Phase Retrieval Methods

The triple star simulation data set was also analyzed by the Knox-Thompson and the phase-unwrapping (Cocke 1980) techniques. The results are shown in Figure 6.21. For this "noise-free" simulation, the Knox-Thompson method gives superior results. It is not clear that this will be the case for Poisson statistics limited data. We do not yet have comparative results for these methods applied to real astronomical data. We have previously published (Hege et al. 1982a) broad-band (5 - 10 nm) images for Betelgeuse and Capella using the Knox-Thompson procedure, and have preliminary results (see section 7.2.2, Figure 7.3) for two narrow-band (.3nm) images of Betelgeuse, using the Fienup procedure only. We intend to extend the comparative studies of Knox-Thompson and phase unwrapping procedures to these data sets.

6.7 Image Modelling Results

We applied non-linear least squares procedures to the interpretation of the Alpha Orionis data sets (see section 7.2.2). We compared the averaged measured radial profile to that computed for a uniform, circular disk (in which case a "diameter" can be extracted) and for a Gaussian radial profile (in which case a scale height can be extracted). In all cases, these simple model profiles departed from the observed intensity profiles at large radii. However, at small radii, even at the diffraction limit of the 4 meter telescope (effectively 3.5m in our filtered reduction), there were too few pixels within the stellar limb to constrain even a simple grey-model for limb darkening in a significant least-squares sense.

Analysis of the full, two-dimensional measurements of Alpha Orionis showed clear asymmetries. In order to characterize the principle asymmetry in a simple way, we chose a model characterized by a major-axis, a minor axis, and a major-axis position angle. Surprisingly several of the broadband measures, in addition to the H-alpha and CaII narowband measures, showed an asymmetry near 110° when this model was fitted to the inner 70mas of the ACF results. The two narrowband measures, however, showed additional structure at larger radii at different position angles. In addition, close inspection of the data contours, compared to the model contours, showed evidence for another significant position angle near 10° near 1 stellar radius.

Our most recent use of this model-fitting procedure was to fit elliptical contours (again major axis, minor axis and position angle) to the observed PS data for asteroids (Drummond, et al. 1984). Sets of these parameters, taken at various times with respect to the asteroids rotational phase as established by its lightcurve, are used in a subsequent least-squares model analysis to fit three body axes and the pole orientation for an ellipsoidal models of the asteroids. A detailed discussion is contained in Drummond et al. (1984).

6.8 Conclusion: Computation Limited

The data processing bottleneck is the single most crucial impediment remaining in the implementation of high resolution imaging systems for use in our Air Force sponsored speckle interferometry projects. For each observation, from 10^3 to 10^5 frames of video data (256 x 256 x 8-bits) must be corrected for geometric and amplitude distortions and Fourier transfromed (or autocorrelated). A typical flow of data through our present computer systems is shown in Figure 6.22. The array processor we proposed in section 4.3 has sufficient bandwidth to accomplish this task at the rate at which the data accumulates at the telescope (7.5 frames/sec for analogue video data - up to 10^6 addresses/sec for event mode data). With our present hardware, this takes from 50 to 150 hours for each hour of observing time. An array processor facility is crucially important to the timely production of sensitive observations for which results could potentially be obtained within hours of the actual observations rather than weeks, as at present. It would also allow the empirical investigation of statistical questions dependent upon analysis of large ensembles of data, and for which theoretical modelling is inadequate, a technique which is presently too expensive computationally to be considered given our limited resources.

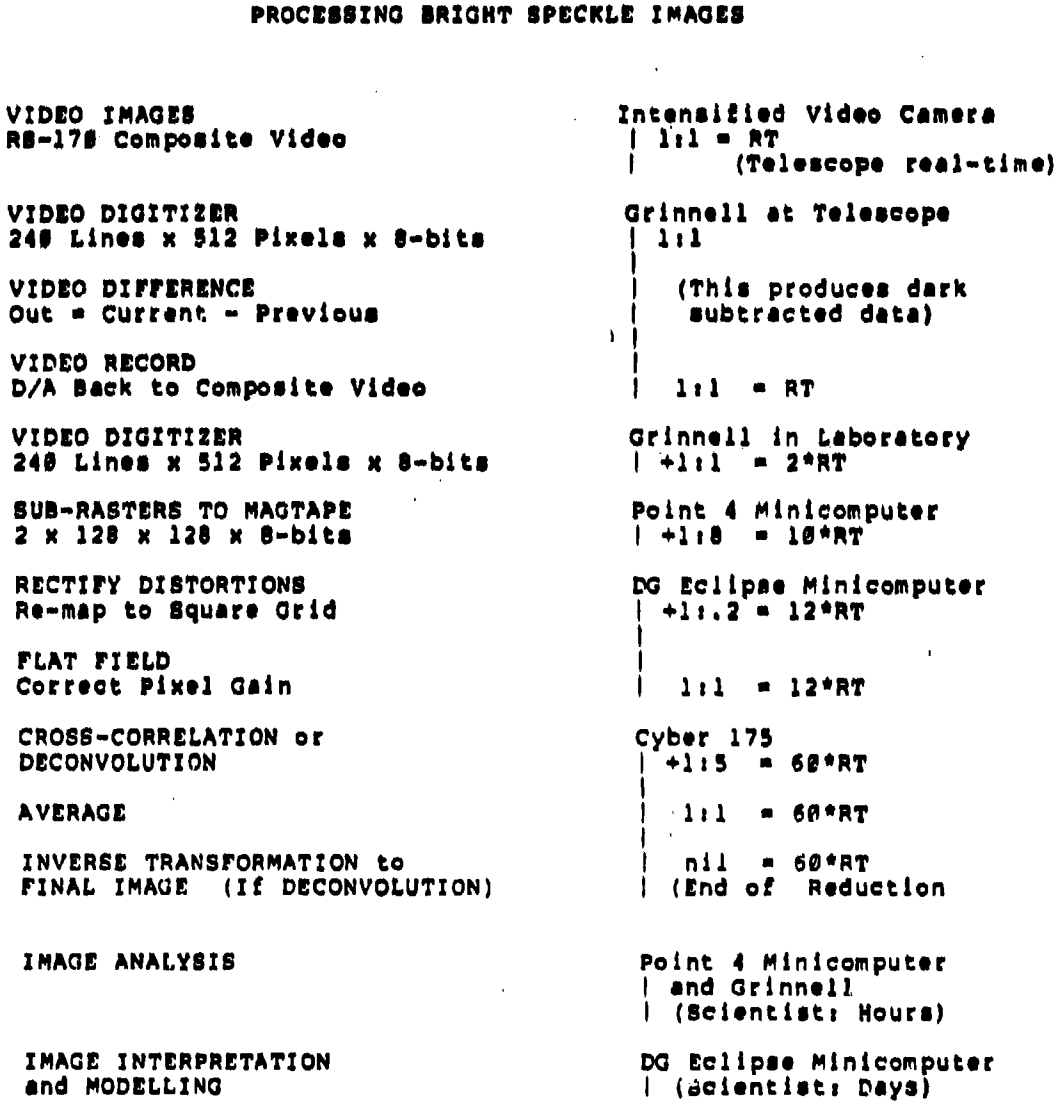

Figure 6.22 Schematics of Speckle Data Reductions Systems.

7. SCIENTIFIC RESULTS

The principal effort in this work has been to develop the MMT for interferometric work and to implement techniques for speckle interferometry, including in particular image reconstruction. Nevertheless, some effort to produce useful measurements has been expended, and we will summarize here some of the principal areas of investigation currently in progress.

7.1 Observations of Artificial Satellites

Due to limited funds for this component of our work, only limited satellite observations were made with the objective of producing proof of principle results. We were able to observe a geosynchronous satellite at the diffraction limit of the MMT, to acquire and track an intermediate range object, and to track a near earth orbit object.

7.1.1 Measurement of FLTSATCOM1 using MMT Interferometer

On 30 March 1983 FLTSATCOM1 was observed for 30 minutes and again on 31 March 1983 for an additional 30 minutes using mirrors B and E (opposite, vertical). The mirrors were cophased using a bright star at similar elevation (within 2°). The observing bandpass was 10 nm at 550 nm. The range of the object during both observations was approximately 37,000 km.

The debiased power spectra, averaged along the direction corresponding to the mirror separation, for FLTSATCOM1 and for an SAO catalogue star near the same elevation (observed to similar statistics) are shown in Figures 7.1 and 7.2 respectively.

From the cut-off frequency in Figure 7.1, the size of the object is approximately 1/50 arcsecond. This corresponds to 3.6 m at the range of the object. It is impossible from this noisy, inadequately calibrated (i.e. bias uncorrected) pair to produce a significant deconvolution. Such a measure would require:

1. A longer integration (Better SNR)

2. Accurate calibration of the photon PSF, or better still a measurement with a true "photon counting" detector (cf section 4.2.2). The present scheme of localizing events in a video raster leads to non-"delta-function" photon responses.

3. Active pathlength monitoring to assure that the telescope MTF is stable during such extended integration and calibration measurements.

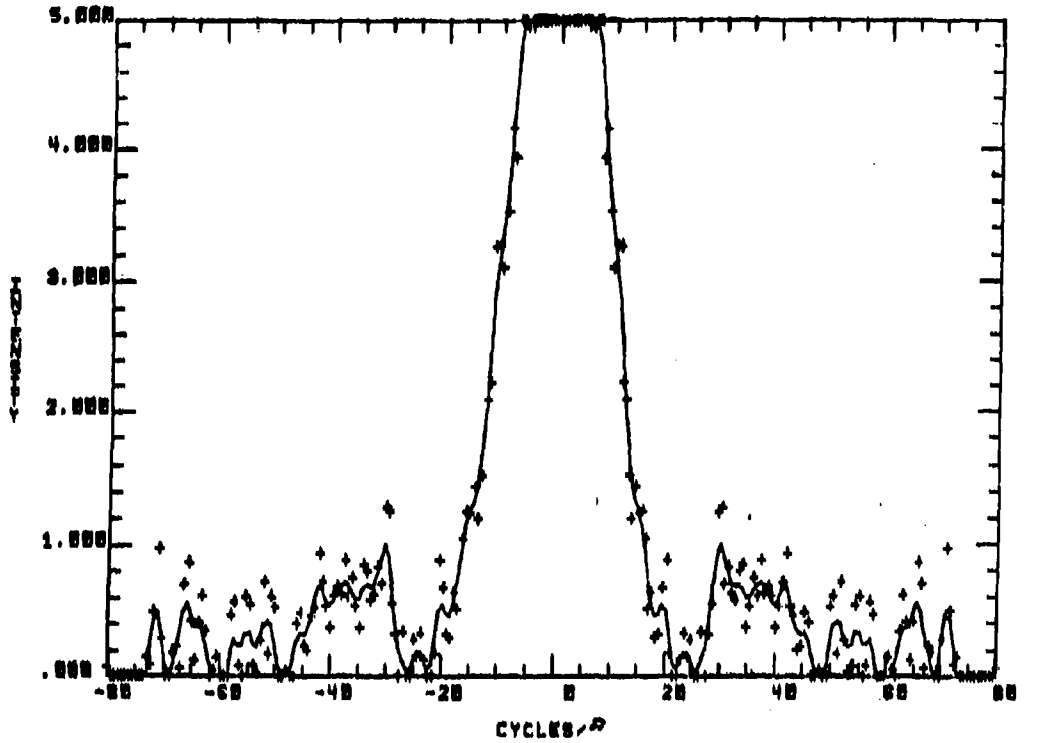

Figure 7.1 FLTSATCOM1 - Debiased power spectrum. No significant energy is seen above about 50 cycles/arcsecond.

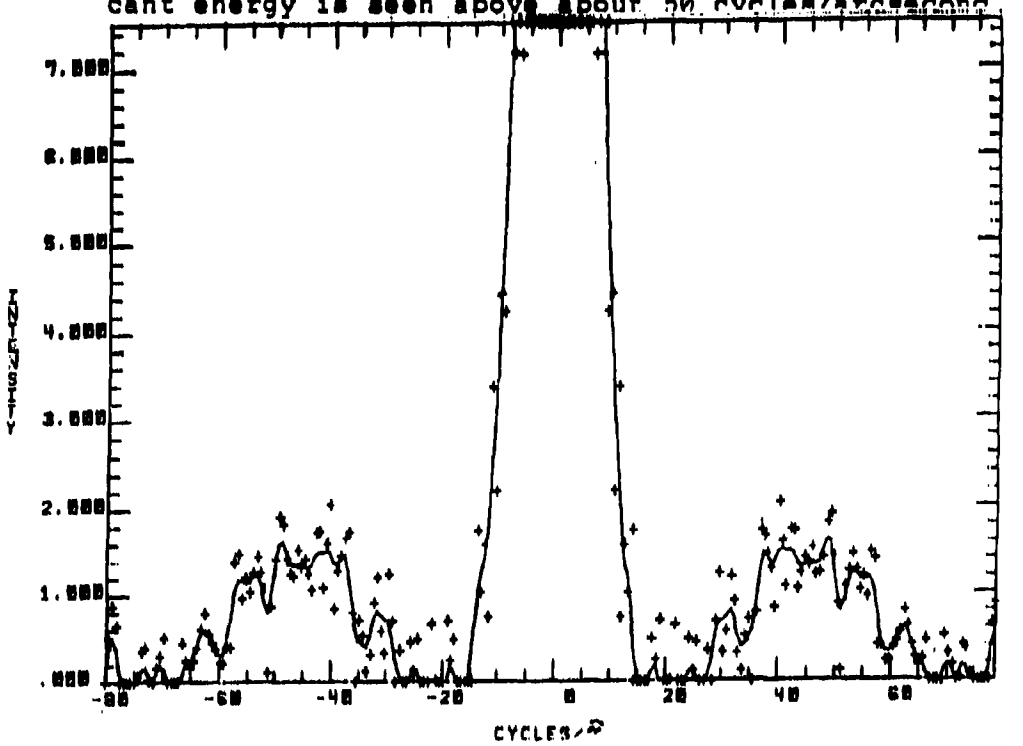

Figure 7.2 SAO 137310 - Debiased power spectrum. Shows energy to 6.86 m aperture cut-off at 61 cycles/arcsecond.

A second observation of FLTSATCOM1, with the same observing parameters, on 5 May 1983 was reduced in somwhat different manner. No effort was made to correct for noise bias. The measurements were taken from the raw autocorrelation functions. A gaussian model was used to correct for the seeing distribution. Then a uniform disk profile was fit to the central residual, but at radii large compared to the size of the photon detection PSF. A similar measure of an SAO star was used to correct for the effects of convolution by the telescope diffraction size. Using

$$(\text{Diameter})^2 = (\text{Measured})^2 - (\text{Star})^2 \qquad (7.1)$$

to deconvolve, in Gaussian approxination, the diffraction-limited (stellar) response from the measured satellite response to give a value 6.1 m for the satellite diameter in the vertical direction.

These two values either disagree drastically, or agree well. But we cannot say which without further analysis. They were observed under different conditions of solar illumination, and the results of our asteriod analysis show conclusively that such large differences in the autocorrelation (or equivalently power spectrum) size can arise from illumination effects. A model analysis of these results has not yet been attempted.

Clearly an image reconstruction or better yet an image retrieval (the difference being whether image phase information is inferred or actually measured) is much to be desired. We have only begun to apply image reconstruction methods (Fienup) to asteroid data and are only in preliminary stages of image phase retrieval (Knox-Thompson) for photon-limited data.

The best estimate presently availabe is the average of these two measures.

Vertical Dia. FLTSATCOM1 = 4.9 m ($\pm$2.0 m)

No measures have yet been obtained with the recently implemented six-beam interferometer (full aperture MMT). We expect that, with open loop control to compensate for temperature effects, and with discrete event Knox-Thompson phase retrieval methods we are now in position to make a well calibrated two-dimensional measurement and, possibly combining Fienup and Knox-Thompson methods, to produce a diffraction-limited image for such an object.

7.1.2 Tracking of Intermediate- and Low-Earth Orbit Objects

Several recent improvements to the MMT have enhanced its performance as a satellite tracking instrument. A new 18 bit D/A and software to match has been installed for both the AZ and EL servos. There is no longer a requirement for separate gain settings for tracking and slewing, thus the glitches formerly induced in changing between tracking and slewing have been elimina-

ted. Autoguiding software is now operational in the Telescope Coalignmenat System which allows common mode tracking errors to be removed by the mount control and differential errors to be removed by the secondaries. This is particularly important for maintaining the cophased condition when operating the telescope as a multiple-aperture interferometer. The present closed-loop operation of this system at 4Hz removes tracking errors at 1Hz.

Experiments

1. Pageos was acquired (about 1/2 degree from predicted position) by manually executing a "square spiral" search around the predicted trajectory. No useful observations were obtained.

(i) The accuracy of the Aerospace supplied ephemeris was limited to 2 decimal places (36") for each point.

(ii) The coordinates were spaced at one minute intervals.

Thus it was extremely difficult to manually apply guiding corrections to keep the object centered in the 5" observing aperture.

Proposed Improvements

(i) The ephemeris must be accurate to 4 decimal places.

(ii) Three or more points per minute are required.

(iii) Such an ephemeris must be supplied in machine readable format to be transferred to the MMT mount-control floppy disk.

2. Space Shuttle was observed using coordinates acquired from Johnson Space Center. These were accurate only to three decimal places (3".6) at 5 second intervals. The object was acquired in the Celestron wide field, and tracked in the 90" field of view of the MMT top-box with tracking errors of 10-20". This was too imprecise to make spectroscopic observations (the purpose of that exercise) but it was encouragingly small for such a rapidly moving object.

Proposed Improvements

(i) A machine-readable, 4 decimal place, 5 second interval ephemeris is certainly required. On-line generation from the orbit elements would be better still.

(ii) The present autoguiding capabilities (common mode errors to mount - differential mode errors to secondaries) at 4Hz may make possible small aperture observations of such low orbit, rapid moving objects with existing capabilities. Further fine tuning of the autoguider may be possible.

Conclusions and Future tests required

1. Intermediate range objects (such as Pageos) present no particularly difficult problems with present telescope capabilities.

(i) Improved precision coordinates on a finer time grid in machine readable form will allow acquisition and tracking with quadratic interpolation will permit manual guiding in a 5" aperture. Coordinate generation directly from the orbital elements would be preferred.

(ii) Autoguiding should make such observations of intermediate range objects routine in a 2" aperture.

2. Low earth objects (such as Space Shuttle) present more of a challenge, but appear possible given sufficiently accurate coordinates and autoguiding capabilities.

a. Autoguiding will be required, even for 5" aperture, but an improved detector will be required to observe at the diffraction limit of the MMT in such a large field of view.

b. Improved autoguider performance, especially increased bandwidth (10Hz) rapid-guiding, appears to be necessary for speckle interferomety in a 2" aperture.

c. Further experiments to determine the properties of the present autoguiding capability are required.

7.2 Astronomical Results

Our principal astronomical programs are studies of asteroids, the gaseous envelopes of red supergiants, the nuclear regions of Seyfert galaxies, atmospheric phenomena affecting diffraction limited imaging, and design of future high-resolution imaging interferometric systems.

7.2.1 Asteroids

Assuming that an asteroid is a smooth triaxial ellipsoid rotating about its shortest axis, the asteroid will project onto the plane of the Earth's sky as an ellipse. At low to moderate solar phase angles ($<45^{o}$), the illuminated portion of an asteroid can still be approximated by an ellipse. As the body rotates it presents a time series of ellipses that change in size, shape and orientation. There is a transformation from this series of observable ellipses to body parameters that involves six variables (three size parameters and three angles).

From these parameters the body axes sizes and direction of rotational axis, including the sense of rotation, can be found.

We have obtained observations of more than a dozen resolved asteroids, and are in the process of reducing the data to dimensions and pole for each.

As of this report we have the following results:

433 Eros

Axes Diameter (Km) Speckle Interferometry

42.1 ± 2.6	RA	359° ±9°
15.5 ± 2.0	DEC	+45°
14.0 ± 2.4		

Others' Results

37.5 ± 1	RA	10° ±2°
15.6 ± 1	DEC	+16°
14.9 ± 1		

532 Herculina

Speckle Interferometry

261 ± 14	RA	120° ±6°
222 ± 16	DEC	-33°
213 ± 18		

Others' Results

220 ------

2 Pallas

Speckle Interferometry

731* ± 38	RA	230° ±6°
547 ± 74	DEC	0°
543 ± 18		

Others' Results

558 ± 8		
526 ± 12	RA	200 ±20°
532 ± 30	DEC	+37

*The possibility of a satellite is not confirmed.

The results for Eros may (especially for our pole) be compromised somewhat by the influence of the large solar phase angle

during our observations (40° and 52°), but we feel that the results are in good agreement with others'.

Our observations of Herculina only yield plausible results if 4 out of our 8 measurements of the minor axis are ignored. In other words at certain aspects the short dimension (as measured in power spectrum space) in much too short. From an extensive analysis of simulated data we conclude that these effects are caused by a bright spot on the surface of Herculina, having the following characteristics:

Longitude (measured from the long axis in the equatorial plane)	160°
Latitude	-35°
Albedo (relative to non-spot surface)	2.2
Diameter of spot	35° or 70 km

Lightcurves of Herculina have been obtained at 4 oppositions, in 1954, 1964, 1978 and 1982. All but the 1978 observations showed one maximum and one minimum in 9 hours, leading to a rotational period of about 18 hours. However, the 1978 observations clearly showed two maxima and minima in 9 hours, the true rotation period. Our results for a bright spot near the tip of the long axis explain the lightcurves quite well. All but the 1978 lightcurves were obtained at southern latitudes (based on our pole) where the bright spot "filled in" one minimum leading to only one maximum and one minimum in 9 hours. The 1978 lightcurves were obtained at northern latitudes, when the spot was mostly invisible throughout the lightcurve.

No evidence for a satellite larger than ~ 50 km exists in the speckle interferometry data. In 1979, we announced that speckle observation of 2 Pallas could be interpreted as caused by a large satellite circling Pallas. We have just applied our ellipsoid model analysis to this same data set, and obtained the single body results given in the previous table. It is immediately apparent that neither interpretation can be ruled out from speckle. However, the binary model predicts a maximum lightcurve amplitude of .10 mag, the ellipsoid model an amplitude of .31 mag, and the maximum observed has been .15 mag. Therefore, lightcurve data favors the binary hypothesis. We have nearly completed the preparatory reduction of more than a dozen observations of Pallas obtained over two nights in 1982, which will hopefully resolve the question (and the satellite if it exists).

Also in the "pipeline" are 511 Davida for which we have completed the computationally intense preparatory reductions

(converting data to two dimensional power spectra with atmospheric seeing removed) and 12 Victoria which is in the preparatory reduction stage. In addition, we have suitable data awaiting the first preparatory reductions for 10 other asteroids: 1 Ceres, 9 Metis, 10 Hygeia, 16 Psyche, 21 Lutetia, 88 Thisbe, 115 Thyra, 145 Adeona, 182 Elsa and 349 Dembowska.

7.2.2 Red Supergiants

We have preliminary results from two programs for observations of red supergiants, the first using conventional speckle interferometry at the 2.3 and 4 meter telescopes and the second using speckle spectroscopy at the MMT

7.2.2.1. Conventional Speckle Interferometry

The Steward Observatory intensfied video speckle camera (Hubbard et al. 1979, Hege et al. 1980,1982) was used at the KPNO 4 meter telescope on 2 and 3 February 1981 for observations of Alpha Orionis. For each of the observing band-passes (see Table 7.1, col 1) 10 minute observations of both α Ori and γ Ori (for seeing and instrumental calibration) were recorded on U-matic video tape. Since in all cases (including the 0.3nm emission-line filters) the speckle images (specklegrams) were sufficiently bright, analogue data amplitudes were recorded with 15ms exposures at 7.5Hz. At this shutter frequency the image intensifier afterglow is sufficiently decayed between exposures that it can be removed by our digital procedures, which subtract from each video exposure the frame immediately preceeding (the dark frame).

The Steward Observatory Point 4 minicomputer system with a Grinnell digital television system was used to record approximately 600 dark-subtracted video frames, digitized 8-bits deep in a 128 X 128 raster, yielding a detector image scale of 7.22 milliseconds of arc (msa)/pixel, on 9-track tape for both α Ori and γ Ori. These digital specklegrams were then Fourier transformed and converted to power spectra, which were then coadded to form the average image power spectrum for each object in each band-pass using the KPNO CDC Cyber-175 computer. These power spectra were then written on 9-track tape for subsequent analysis using the Steward mini-computer.

The starting point of the analysis is the summed power spectra ($\sum$ PS) of the individual 15ms specklegrams. Each $\sum$ PS of α Ori at a given wavelength was calibrated by a similar $\sum$ PS for the nearby point source γ Ori, the two data sets being taken as nearly simultaneosly as possible, to ensure similar statistics for tho seeing.

Table 7.1

SIZE PARAMETERS FROM α ORI AUTOCORRELATIONS

Wavelength		Diameter (Radial)	Diameter (2-D fit)	Shell Radius	Principal Asymmetry	Relative Shell Inten.
410nm	10nm	61.7mas	53.8mas	280mas	95°	1%
520	10	49.6	48.1	250	110	1
650	2	54.9	47.5	-	(Round)	<0.3
656.3	0.3	54.3	48.1	235	130	3
850	10	46.5	39.9	-	(Round)	<0.5
854.2	0.3	53.0	41.7	290	110	11

The α Ori Σ PS were deconvolved by the following procedure: (i) Each Σ PS was deconvolved by the appropriate detector transfer function (DTF), which was obtained by finding the Σ PS of a large number of frames uniformly illuminated at low light levels (isolated photoelectron events). (ii) The resulting quotients were debiased by subtracting a constant, determined by the average quotient value at the theoretical telescope aperture cutoff. (iii) the raw seeing-corrected α Ori power spectra were then obtained by dividing the debiased α Ori power spectra by the similarly debiased calibrating γ^1 Ori power spectra. This data reduction procedure is described in more detail in Hege, et al., (1982). This deconvolution is written as

$$\text{Deconvolved PS} = \frac{\text{PS}(\alpha\ \text{Ori}) - \text{Bias}}{\text{PS}(\gamma^1\ \text{Ori}) - \text{Bias}} \quad . \qquad (7.2)$$

As expected, these seeing-corrected power spectra seemed well-behaved at spatial frequencies less than the aperture limit; but near this point, they became very noisy because of the low signal-to-noise in the quotients, and, of course, beyond the aperture limit they are meaningless. (iv) Finite resolution was then reintroduced, in a consistent way, by filtering (multiplying) by a computed aperture function, chosen to have a high frequency cut-off about 10% less than the telescope diffraction limit in order to suppress the high-frequency noise. (v) The resulting filtered spectra were then cleaned by an iterative technique which forces the physical constraint that both members of an autocorrelation-power spectrum pair be non-negative. Corrections for certain systematic artifacts, recognized to be caused by video processing of the data, were also made.

The resulting autocorrelation functions showed several features suggesting departure from simple radial symmetry, and from a simple (limb-darkened) round disk. Since image autocorrelation functions (or power spectra) have the effect of a) preserving the original image frequencies (up to the filter cut-off) but b) scrambling the image frequencies radially (because of loss of the image phases), it is necessary to use mathematical models in order to interpret them. Thus we compared the averaged measured radial profile to that computed for a uniform, circular disk (in which case a diameter can be extracted), and to that for

some limb-darkened radial profiles (in which case a scale height can be extracted). We then examined the residuals of the least-squares fits of the model profiles to the observed profiles in order to refine the models. In all cases, uniform disk profiles departed from the observed intensity profiles. However, even at the diffraction limit of the 4 meter telescope (effectively filtered to 3.5 meters by the combination of its 3.8 meter pupil mask and our final noise filter), there are too few pixels within the stellar limb to constrain even a simple grey-model for limb darkening in a least-squares sense. Thus we report in Table 7.1 (col 2) radial profile core diameters which are the results of fitting a uniform disk autocorrelation profile (convolved with the filter resolution) to the averaged radial profiles. Empirically these diameter measures were found to be within about 5% (equivalent to the precision of the measures) of the 2σ diameters for gaussian profiles (σ = half width at 1/e) fit to the same data.

Except for the results at 650nm and 850nm, the data profiles fell more slowly than the model profiles at distances greater than 1-2 core diameters. The shell radii reported in Table 7.1 (col 4) are the radii at which these profiles fell to the noise level of the measurement background. These excess profile intensities appear to be particularly significant in the narrow-band measurements at 656.3nm and 854.2nm, and for the broad-band measures at 410nm and 520nm. The relative shell intensity (col 6) is a measure of the integrated excess intensity in these "shells" compared to that modelled in the radially averaged core profiles.

Analysis of the full, two-dimensional measurements showed clear asymmetries, which to some extent were shared by all of the measurements and which also showed individual variations. In order to characterize the principal asymmetry in a simple way, we chose a three-parameter fit to the two-dimensional intensity distribution in which a uniform-disk intensity profile was azimuthly scaled in order to extract a major-axis, a minor-axis, and a major-axis position angle. That postion angle is given as the position angle of principal asymmetry in Table 7.1 (col 5) and the mean diameter (a+b)/2 is given as the 2-D fit core diameter (col 3). These core diameters are consistently smaller than those extracted from the averaged radial profiles, a result which emphasizes the model-dependent nature of the results of such model parameterizations. The principal asymmetry, which appears to be shared by all of the data sets parameterized this way, is a preference for a SE-NW position angle near 110° (modluo 180°, range 95° to 130°).

There appear to be significant departures from this general tendency which we characterize in Table 7.2 by listing the position angles of the intensity maxima of the measured auto-correlation intensity profiles taken at constant radius.

Table 7.2

POSITION ANGLES OF ASYMMETRIES AS A FUNCTION OF RADIUS
(All angles are Mod 180°)

	Radius						
Wavelength	18msa	36msa	54msa	72msa	108msa	144msa	180msa
410nm	110°	110°	-°	-°	-°	-°	-°
520	110	110	110	-	-	-	-
650	0	0	10*	10*	-	-	-
656.3	90	100	120	115	80,130	80,125	85,120
850	40	40	40,130	-	-	-	-
854.2	90	110	110	110	110	100	75

* Reported in Goldberg et al. (1981) as 28°.
- Too noisy to measure at this radius.
, Two maxima in the circular profile.

From these morphological interpretations, we infer the existence of a resolved core, corresponding to the photosphere of α Ori, and also an extended low-intensity asymmetric structure which we refer to as a "shell". The shell is most prominent in the emission-line autocorrelations at 656.3nm and 854.2nm. The effect of the Fourier noise filter is assumed to follow the approximate convolution rule $d^2_{Model} = d^2_{Core} + d^2_{Filter}$. The uncertainty in both core estimates (Table 7.1, cols 2 and 3) is about 2.0msa (2σ). This represents the systematic variation obtained by changing the bias corrections for both the object and the calibration power spectra, as well as the noise-filter cutoff frequency, within reasonable limits.

We note that the values of the 2-D fit core diameters for the group 410nm-656.3nm are all approximately 50msa, whereas d_{Core} for 850nm-854.2nm is about 40msa. We believe this result is significant, and it seems to corroborate earlier measurements by Welter and Worden (1980).

All of these measures (both Tables 7.1 and 7.2) were taken from the final, reduced autocorrelation functions, and the two-dimensional measures in Table I were restricted to the central 70msa. Only for the narrow-band measures at 656.3 and 854.2nm is there unambiguous evidence in the two-dimensional analysis for structure beyond about 120msa. It is only in the averaged radial profiles that we see what appears to be evidence for even larger (to about 250msa) extensions. The evidence for the larger scale structure should be considered only suggestive as there is considerable uncertainty in the low frequency calibrations (seeing corrections) provided by the γ Ori deconvolutions. These calibration uncertainties also contribute to a large uncertainty in the actual values of the integrated shell intensties given in Table 7.1; however, we expect that the enhanced intensity of the shell observed in H_δ and CaII, as well as the similar extensions with lesser intensity in the broader bands and 410 and 520nm which span many spectral features, is real.

A method for reconstructing 2-D image phase information from image autocorrelation functions developed by Fienup (1978,1980) was used to produce the images shown in Figure 7.3 for the 656.3nm and 854.2nm measurements. We believe that the finer details of these maps may not be significant, but that the overall morphology (except for a 180° orientation ambiguity) is probably correct. Thus we see that the inner 50mas core (highest brightness contour) is quite round and that the principle asymmetry at about 110-290° is shared by both. They both show evidence for distortion at approximately 15-205°, consistent with that previously reported for a measurement at 650nm in Goldberg et al. (1981), at a smaller radius. Because of the relatively low resolution of these measures, it is difficult to assert whether such distortions of the intensity contours are caused by a surface feature near the limb (as asserted in Goldberg et al.) or by a chromospheric feature near the surface.

The preliminary results reported by Goldberg et al. (1981) are reassuringly similar to those reported here. The 24 Nov 1980 data, acquired in the "photon event" mode at 656.3nm show, in common with the present data set, evidence for an intermediate range (1-3 core radii) extension at about 110° and for a smaller one (about 1 core radius) at about 20°. In the present data set, the largest scale extensions, seen unambiguously in the H and CaII only, appear to be at about 80° (at 2-5 core radii, beyond the radii tabulated in Table 7.2). The earlier data has poorer resolution, having been taken at the Steward 2.3m telescope, but the two data sets yield the same physical sizes for the extensions. Thus the sizes of the resolved features measured do not depend on the system resolution. It is doubly reassuring that data acquired in two very different modes (photon event vs analog) show the same overall features.

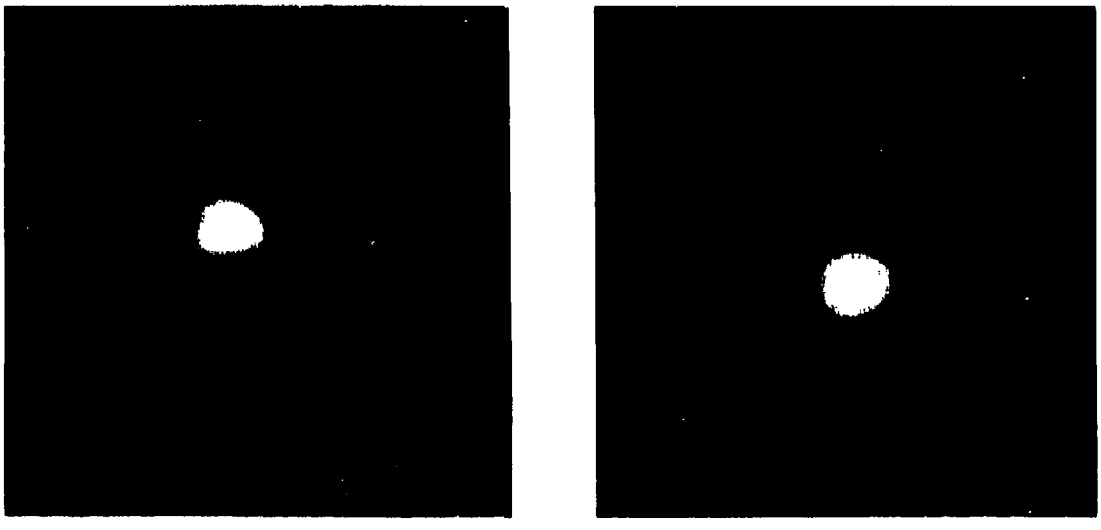

Figure 7.3 Reconstructed (Fienup) images for Alpha Orionis. Left - 656.3 nm. Right 854.2 nm.

The 24 Nov 1980 data can be compared well with data taken at nearly the same time by Roddier (1983). Figure 7.4 presents two power spectra. Spectrum (a) is from data taken by us at the 2.3m telescope, and (b) was prepared by Roddier from data acquired by means of his shearing interferometer about a week earlier at the 3.8m CFH telescope. The two power spectra are strikingly similar, giving yet a third cross check on our measurements.

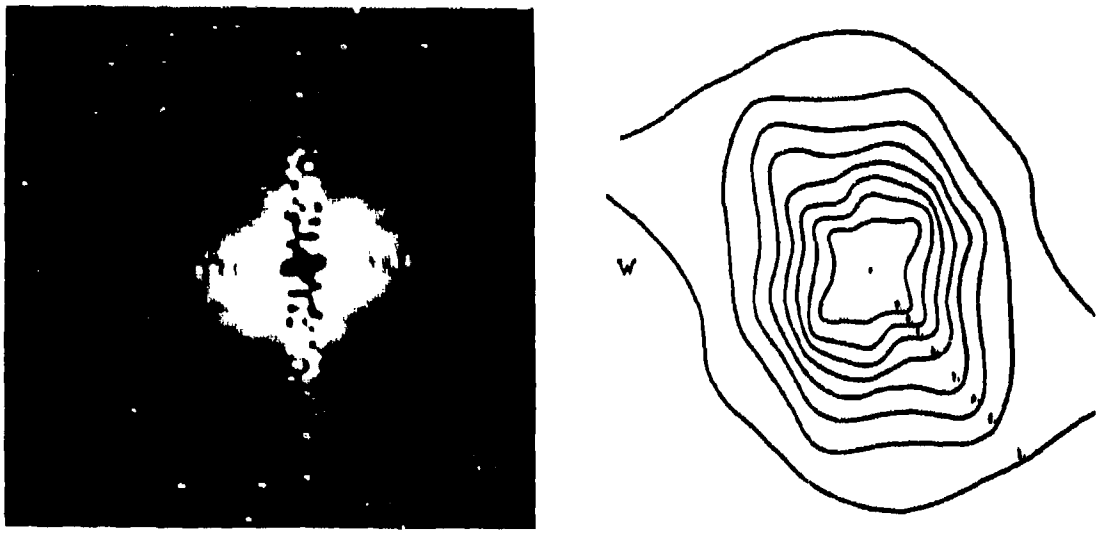

Figure 7.4 Alpha Orionis power spectra. Left - our result. Right - Roddier (1983).

Thus we see that the results of our speckle observations pass some crucial tests: The measurements give values for sizes and orientations that do not depend much on resolution or on acquisition mode, and totally different observing systems yield results that are quite similar.

7.2.2.2 Speckle Spectroscopy

Low resolution speckle spectroscopic observations of Gamma Cassiopeiae, Alpha and Beta Ceti, Rho Persei and Alpha and 119 Tauri were carried out at the MMT on the night of 6 Dec 82 using the speckle spectrograph configuration described above. The 20 μm slit was chosen so that the seeing distribution is sampled over a scale width corresponding approximately to the width of the single mirror speckles, and the slit was oriented perpendicular to the interferometer fringes. The slit was then imaged through the zero mean deviation prism onto the photocathode of the Steward Observatory intensified video speckle camera (Hege, et al., 1980) using the 45x microscope. The analogue video data was recorded on 3/4inch video cassettes. Later in the laboratory the taped video data was digitized 8-bits deep, 128 pixels per line and stored as 240 line frames on 9-track digital magnetic tape. The Fourier transform and square modulus of each line of each of

3600 frames of digitized data was computed and the transformed data was coadded line by line and frame by frame. The result for each observation is a 64 pixel per line by 240 line spectral density array.

The MMT speckle spectrograms for an unresolved source are characterized by a low frequency domain, corresponding to single mirror speckles and by a high frequency domain characterized by fringes corresponding to the two-mirror baseline which, as expected, curve to higher frequencies with decreasing wavelength. A typical line of the spectral density distribution is shown in Figure 7.5. These one-dimensional spectral densities for each wavelength interval result from a convolution of the atmospheric "seeing" and the telescope optical transfer function with the object in the direction perpendicular to the slit at the wavelength corresponding to that line. Each line also includes an additive noise bias corresponding to the mean number of photons detected per frame and multiplied by the detector transfer function corresponding to the point spread function for photon detection.

The power spectral density $PS(u,\lambda)$ can be written as

$$PS(u,\lambda) = \{\langle|O(u,\lambda)|^2\rangle\langle|A(u,\lambda)|^2\rangle + n(\lambda)\}\langle|D(u,\lambda)|^2\rangle \quad (7.3)$$

where

$|O(u,\lambda)|^2$ = square modulus of the FT of the object intensity function at wavelength

$|A(u,\lambda)|^2$ = square modulus of the FT of the atmospheric optical transfer function convolved with the telescope optical transfer function

$$= |At(u,\lambda)|^2 \, |Te(u,\lambda)|^2 \quad (7.4)$$

$n(\lambda)$ = average number of photons detected per frame

$\langle \ldots \rangle$ = time average, i.e. average over many frames

as discussed in Hege, et al. (1982a).

If we had a perfect detector, photons would be detected as delta functions thus making $\langle|D(u,\lambda)|^2\rangle$ a spatially constant term. Perfect detectors do not exist, however, and photons are detected as splotches of small but finite size. Thus the FT of the detected photon spots appears in the PS as a nearly gaussian curve (see Figure 7.5).

Since the telescope modulation transfer function $|T(u,\lambda)|^2$ has a finite cutoff frequency $u_c(\lambda)$ determined by the maximum baseline in the aperture, for frequencies greater the $u_c(\lambda)$ the measured spectral density $PS(u,\lambda;u>u_c(\lambda)) = n(\lambda)\,\langle|D(u)|^2\rangle$ containing only information about $n(\lambda)$, the number of photons, and $\langle|D(u)|^2\rangle$ the detector transfer function. This is true at any

other frequencies for which $T(u,\lambda) = 0$ such as the intermediate frequencies not transmitted by the two-mirror MMT interferometer aperture. If the detector plane is sufficiently over-sampled, i.e. if there are sufficiently more than 2 pixels per diffraction limited resolution element, then a gaussian curve fit to $PS(u,\lambda;u>u_c)$ provides an estimate $G(u,\lambda)$ of $n(\lambda)\langle|D(u)|^2\rangle$ as shown by the broken-line curve in Figure 7.5. Thus, we form the debiased estimate

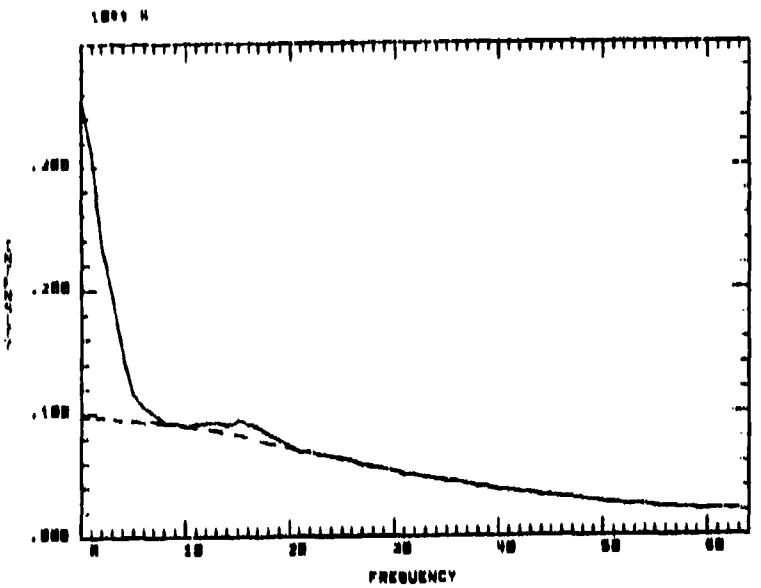

Figure 7.5. Average power spectral density along a typical speckle specklegram raster line. MMT opposite mirror pair.

$$\frac{PS(u,\lambda)}{G(u,\lambda)} - 1 = |O(u,\lambda)|^2 \langle|M'(u,\lambda)|^2\rangle \qquad (7.5)$$

$$\text{where } \langle|M'(u,\lambda)|^2\rangle = \frac{\langle|A(u,\lambda)|^2\rangle\ |T(u,\lambda)|^2}{n(\lambda)\ |D(u)|^2} \qquad (7.6)$$

with the reasonable assumption that the object intensity distribution and the telescope and detector transfer functions are not (significantly) time dependent.

The reduced modulation transfer function $\langle|M'(u,\lambda)|^2\rangle$ is estimated by similarly reducing a set of observations of an unresolvable star acquired under similar circumstances. The deconvolved object visibility (squared) is then estimated by

$$|O(u,\lambda)|^2 = n(\lambda)\ \frac{\{PS_O(u,\lambda)/G_O(u,\lambda)\} - 1}{\{PS_*(u,\lambda)/G_*(u,\lambda)\} - 1} \qquad (7.7)$$

where the subscripts o and * refer to measurements of the object and an unresolved star respectively. The factor $n'(\lambda) = n_*(\lambda)/n_o(\lambda)$ is not determined by this method, but this is only a scaling factor which does not affect the size determination, as it is the ratio of the two wavelength spectra. Particularly, it does not affect the value of u at which $|O(u,\lambda)|^2$ becomes zero for a resolved object.

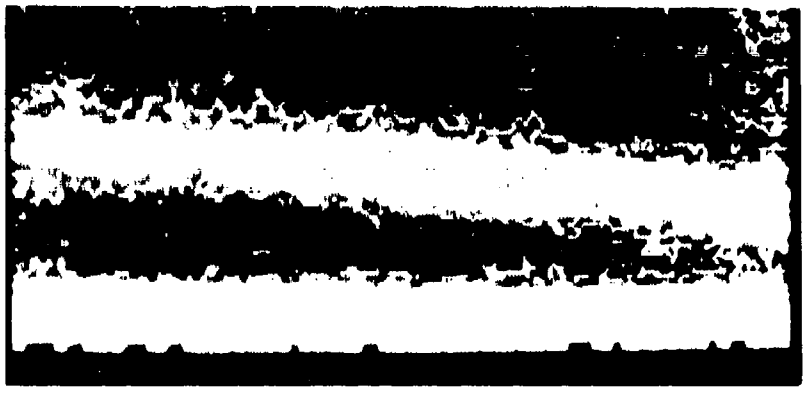

Figure 7.6 Gamma Cas. Debiased one-dimensional power spectra as a function of wavelength.

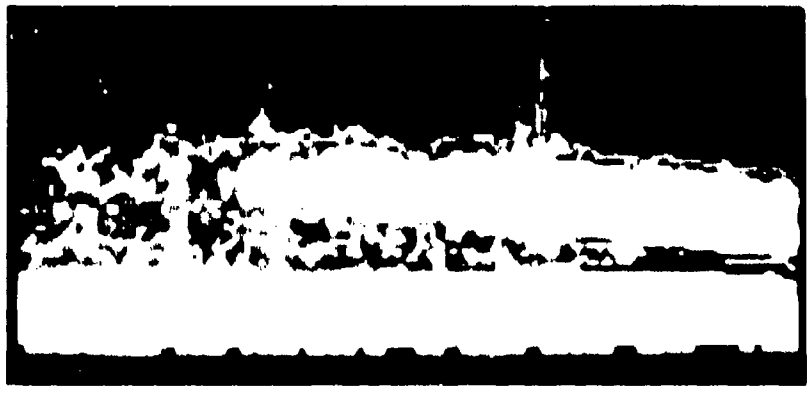

Figure 7.7 Speckle Spectroscopy of α Tau. The star is resolved at a mean diameter of 22 msa. There is evidence for a larger diameter (about 24 msa) at the 616 nm TiO band.

The debiased estimates for α Tau, and for the unresolvable star γ Cas are shown in Figure 7.6 and the quotient representing the (squared) visibility estimate for α Tau for frequencies sampled by the MMT interferometer is shown in Figure 7.7.

7.2.3 Seyfert Nuclei

The only significant result from our active galactic nuclei project is a continuum measurement at 550 nm for NGC 1068 showing it to be unresolved at the 2.3 m telescope (upper bound 15mas). The N-S and E-W autocorrelation profiles are shown superimposed in figure 7.8. The artifacts at small radii are due to difficulties with the photon PSF (noise bias) calibration, again evidence for our need for better event-detecting systems and methods.

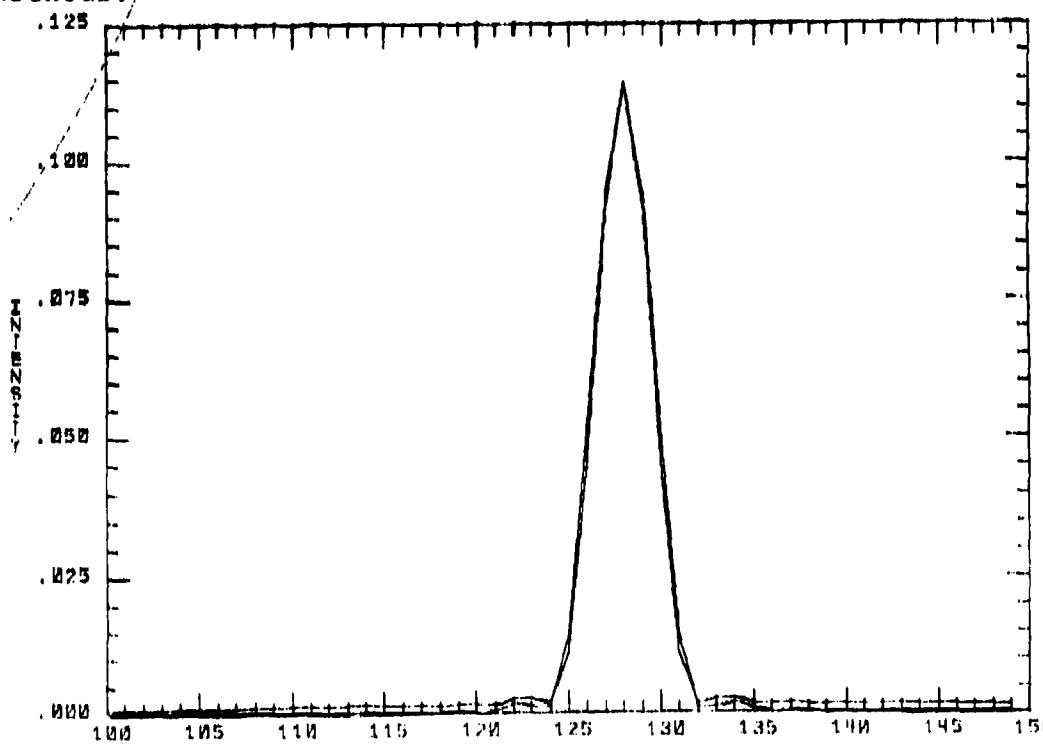

Figure 7.8 Central region of NGC 1068 autocorrelation (seeing corrected) - unresolved at 550 nm, 0".0092/pixel.

7.2.4 Isoplanicity Studies and Seeing Phenomena

Two aspects of the seeing problem are currently under investigation. The first, primarily the work of Christou (1983), concerns the effects of intrinsic atmospheric phenomena on the speckle imaging process. The second, Woolf and Ulich (1983b), concerns the effects of site, and especially winds, on the general image quality.

7.2.4.1 Isoplanicity Measurements

A study of the effect of non-isoplaniticity upon speckle interferometric data is being carried out as part of a doctoral dissertation. This non-isoplanaticity affects the instantaneous Point Spread Function (P.S.F.) of the telescope/atmosphere combination as a function of position in the object plane. For example, the two components of a close binary star can have different P.S.F.'s associated with them. In the speckle process, i.e. time averaged power spectra, the effect of the differing P.S.F.'s is to reduce the fringe modulation in the power spectrum of the binary star. Thus the computed intensity ratio of the two components is increased over its actual value unless non-isoplanatism is taken into account.

For any wide-field imaging problem non-isoplanaticity is an important consideration. One of the aims of this project is to determine, in a quantitative manner, the limitations upon interpretation of reduced speckle data (power spectra) due to non-isplanatic effects. These quantitative measurements take the form of time averaged cross spectra between the instantaneous speckle patterns of the components of binary systems of differing separations. The relationship of the cross spectra to the Fried seeing parameter, r_o, is to be investigated and r_o is determined from the actual specklegrams. An offshoot of these measurements of r_o is to be able to bin the specklegrams so that deconvolutions between program object power spectra and point source power spectra are performed for similar seeing conditions in order to improve the precision with which visibility functions may be calibrated.

This analysis also enables statistical measurements of the seeing variations to be made for a given data set. Such measurements could then lead to possible wind driven models and therefore provide atmospheric information. Because of this a number of sites and telescope aperture sizes and geometries are being used for the data acquisition.

7.2.4.2 Seeing Phenomena

Most large telescope science output is critically dependent on the degree of blurring of the image. Two pernicious effects are liable to blur a telescope image beyond the limits set by the instruments optical quality. Many astronomers still believe that most "seeing" is caused outside the telescope facility, and that telescope "sailing" can be prevented by the use of windscreens. It is our thesis that most seeing for most large telescopes is self-induced, and is in part caused by an attempt to shield them from the wind.

The route to this conclusion is painful, since many millions of dollars have been poured into giant telescopes which produce mediocre images. It is likely we would still be building

telescopes with poor images but for the novel character of the MMT. Aided by good luck, and driven by a shortage of funds, the design of the MMT facility allowed a reduction of facility seeing below the level of that produced by the remainder of the atmosphere. This then revealed that other lage telescopes were not routinely reaching the limits permitted by the atmosphere.

This surprising result has still not been used to full advantage. At this time, the MMT primary mirrors still have an inadequate figure that was meant to match the average seeing anticipated (1-2"). Nontheless, it has been possible to explore the reduction of facility induced seeing, and to confirm that a necessary part of the strategy is to expose the telescope to the wind.

The MMT is very rigid, and winds at Mt. Hopkins are low, but despite this the vibration of the MMT is just marginally permissible. Scaling this result to larger sizes suggests that wind vibration will be a major problem with giant lightweight telescopes, and a major task of both telescope design and site selection is to keep sharp images from being lost and "Gone With The Wind".

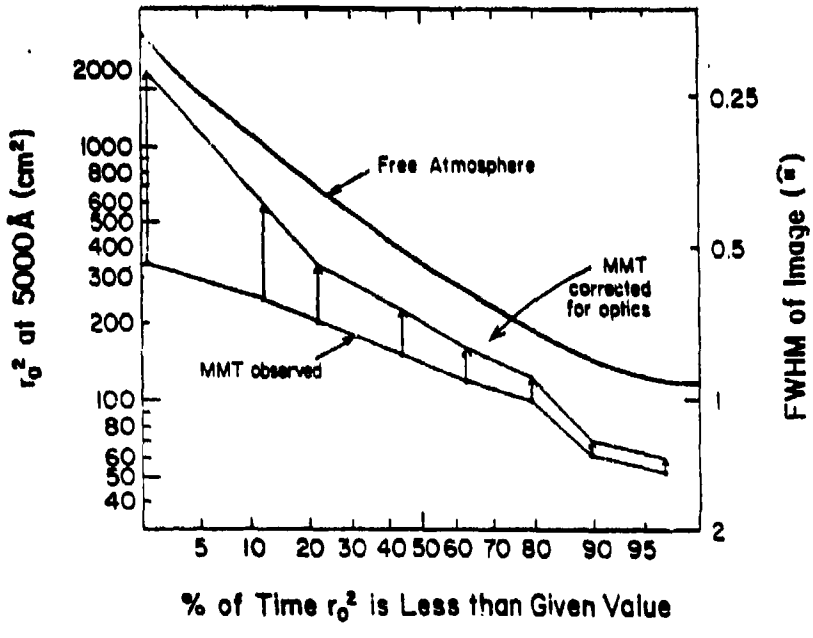

Figure 7.9 Free atmosphere seeing compared to actual seeing at the MMT.

Overall site performance may be expressed as a single figure by Fried's parameter $\langle r_o^2 \rangle$, at a standard wavelength such as 500 nm, which is a measure of the reciprocal of the image area (Woolf 1982). The seeing of the free atmosphere has been measured by balloon soundings (Barletti et al. 1976), and is plotted in

Figure 7.9. Beckers (1982c) has observed the instantaneous FWHM at the MMT on 91 nights, and has published his observed distribution function. In Figure 7.9 we have plotted the distribution function for his results by converting the FWHM to r_o with the relation $\Theta = 0.995\ \lambda / r_o$, appropriate to a seeing image. Also shown in Figure 7.9 are the results corrected for the interferometrically measured optical imperfection of the telescope (Beckers and Williams, 1982d). From the figure, the MMT seeing measured by image area is about 30% poorer than the free atmosphere alone, and the seeing is better that 1" some 85% of the time. It is possible for instantaneous images to be far better that average, and indeed from the 2.3 m telescope we have recorded an instantaneous image of Arcturus with a 0".2 FWHM, when the mean value of r_o was 12 cm. Fortunately, there are some other types of seeing measure that check and confirm these results.

Forbes and Woolf (1983) show that image motion can be used to measure seeing, even for giant telescopes. They published one such measure of MMT seeing. Woolf, McCarthy and Angel (1982) have published a further five such measures. Unfortunately, one measure was taken on a night when the telescope was opened at midnight with a 4°C temperature difference from inside to outside, and with appropriately awful seeing. For the other five nights with good measures, the computed values of r_o are consistent with the results in Figure 7.9. From the Beckers data, the mean value of $\langle r_o^2 \rangle$ is 320 cm^2 whereas from the image motion the value is 350 cm^2. The corresponding value for the free atmosphere is about 500 cm^2.

Details of this study are published as Woolf and Ulich (1983b).

7.2.5 Interferometer Design Studies

In an effort related to this project, Woolf and his collaborators have been studying designs for high resolution, interferometric imaging systems, including both ground based and deployable configurations.

7.2.5.1 The Versatile Array

The surge of interesting observational results encourages the design of higher resolution and sensitivity imaging systems . The very large change in quality of interferometric data, with modest changes in observing conditions, suggests that interferometry makes a poor sole justifier for a giant facility at optical and IR wavelengths. An optimum facility would exploit extraordinary conditions for interferometry and yet facilitate high interest conventional work when conditions are more ordinary.

A study of the optimum use of collecting area in a visible

or IR interferometer shows that greatest sensitivity is obtained by dividing the area into two equal apertures, and moving one so as to sequentially explore the U-V plane. For a practical interferometer, there is a benefit from reducing the types of motion needed for a large aperture, and in keeping the moved apertures to manageable dimensions. We have chosen to balance these needs by considering an array of four 8m mirrors, in which the exploration of the U-V plane is done by an azimuth motion of the array, coupled with the diurnal apparent motion of the sky.

The concept welds together four main ideas. First, due to Low (1980), is the idea that a linear array which points at right angles to the array line, and which rotates on a track for azimuth pointing is a very convenient form of interferometer. Second is an idea from Traub and Gursky (1980) that an optimum form for a small number of telescopes in a line is as a non-degenerate array. Third, originating with the 200-inch telescope, and picked up by Angel (1983), is the idea that lightweighted castings of borosilicate glass make good inexpensive telescope mirrors. Indeed, though we now know how to get them into better thermal equilibrium with the air and themselves, the performance of the 200-inch is itself the clearest indication that this is a good route. Fourth, arising from Beckers' and Hege's work (see section 3) with the MMT, is the realization that an MMT-like focus can, by careful choice of geometry, be operated as a phased focus over the field width for which the atmosphere allows isoplanatism.

Figure 7.10 shows an optical scheme for a Versatile Array, when used in non-degenerate array form. Details of this concept have been published by Woolf, et al. (1983a). In the non-degenerate configuration, the center to center separation of the outside mirrors is 72 m. If one of the mirrors is brought to the other side of center, this separation is increased to 108 m, and is therefore useful for obtaining the highest possible resolution. However, such observations would leave a gap in the U-V plane. The third configuration is to use the system as three separate telescopes (non-interferometrically).

Figure 7.11 shows the MTF for the array at 2.2 microns, in the direction of highest resolution. At right angles to this direction the pattern is like that of a single 8 m disk. The resolution in the pattern is somewhat poorer than if the two outer mirrors were used alone as an interferometer. The two-mirror 108 m spaced mirrors gives better resolution.

Because the diffraction pattern of the array only produces high angular resolution in one direction, reconstruction of a picture requires combined use of the apparent diurnal rotation of the sky, and the rotation of the array. Observations in a least 14 different position angles are needed to specify the U-V plane.

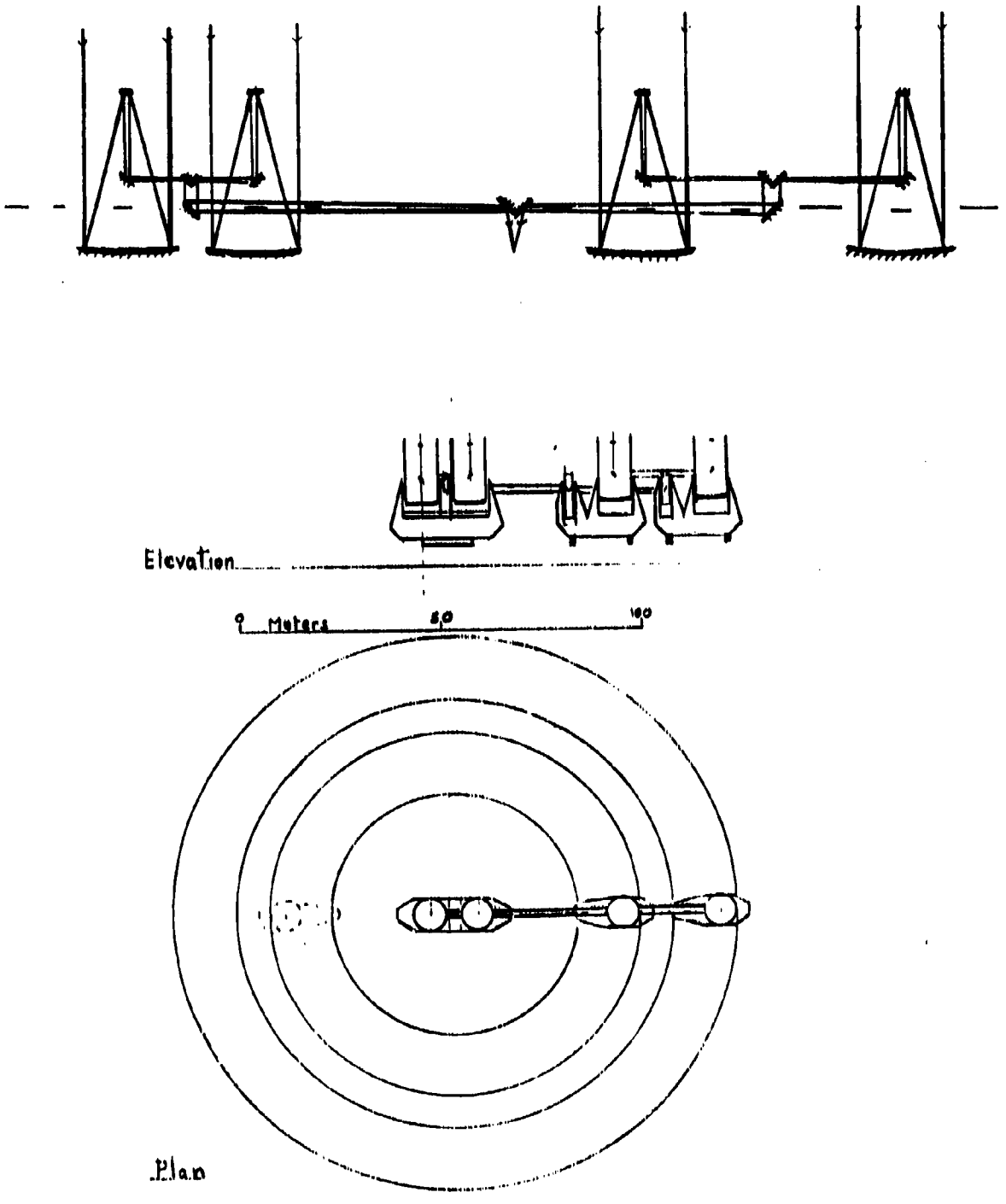

Figure 7.10 Optical schematic (above) and plan (below) for a Versatile Array.

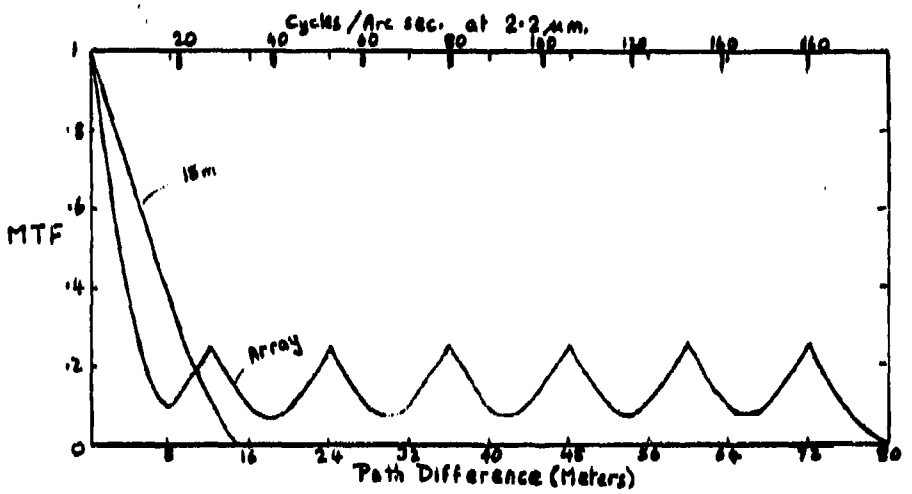

Figure 7.11 MTF for the Versatile Array at 2.2 um.

The use of a system like the Versatile Array for high angular resolution mapping would need the systematic errors of individual visibility measures to be brought down to a level where they do not dominate picture noise. This level is about 1%, and is far better than has been accomplished with speckle to date. In order to achieve this precision, a systematic measure of seeing correct to about 0.5% is required. Lena (1982) has suggested that visible seeing should be monitored during IR speckle measures. Since the instantaneous wavefront disturbances are unlikely to match the Kolmogorov spectrum of the average, this may be inadequate for most telescopes. For the Versatile Array it is definitely incorrect. When adaptive optics is used on the separate 8m telescopes, the long wavelength wavefront corrugations are substantially smoothed, but the short wavelength corrugations remain. Thus the visible and IR seeing become decoupled. It is recommended that monitoring the seeing should be performed at the same wavelength as the speckle observations. Indeed, there is a possibility that a variant of the Welter and Worden (1978) method in conjunction with frequent reference to a nearby star may be the best method of correcting for seeing.

In addition to seeing modifying the speckle transfer function, it is also modified by the exposure time, if that becomes comparable with, or longer than, the speckle change time. This effect can inject random differences in transfer function between the reference star and the object. The use of TV frame

rates for visible speckle observations may be one reason why visible region speckle results tend (consistently) to be less precise than IR measures (especially at high spatial frequencies). This again emphasizes the need for a discrete event photon-detecting system such as that of Papaliolios and Mertz (1982, cf section 4.2.2) or other advanced technology scheme such as the MEPSICHRON (Firmani et al., 1983).

7.2.5.2 Deployable Configurations

Experience with the MMT and with radio telescopes seems to show that there is a relatively easy approach to aligning and to phasing multiple optics telescopes by means of astronomical sources, using astronomical observing equipment. After extensive review of the existing and proposed methods for coaligning and cophasing not only the MMT but a wide range of existing and proposed telescope configurations, from optical to radio wavelengths, Woolf and Ulich (1983b) and Meinel, Meinel and Woolf (1983) conclude that large deployable arrays, with panel geometry scale set by the size of the Space Shuttle instrument bay, are feasible.

It is beyond the scope of the present work to review these papers here.

8. ACKNOWLEDGEMENTS

Because of the extensive nature of this work, it is impractical, if not impossible, to separate clearly that which was specifically supported by AFGL from that which constitutes the total high-resolution imaging program at Steward Observatory. Just the optical, not to mention IR, thermal-IR and sub-millimeter, work is funded by several additional sources and benefits from the contributions of many additional personnel.

Additional support for this work comes principally from:

(i) AFOSR (82-0020) Speckle Interferometry and High Resolution Imaging.

(ii) NSF (AST-8113212) Experiments in Differential Speckle Interferometry. This grant funded the MMT interferometer development without which, e.g. the satellite observation could not have been made.

(iii) NASA (NAGW-224) Speckle Interferometry Applied to Asteroids and Other Solar System Objects. The work on model development and power spectrum and autocorrelation function interpretation was aided by this support.

(iv) E.M.Hege and C.B.Mashburn (to EKH) for purchase of microprocessor system for Event Data reductions.

(v) KPNO for extensive use of the Cyber 175 for reductions of speckle observations taken with the 4 m telescope.

Among those who, in addition to the principal investigators, made major contributions to this work are:

(i) J.M.Beckers, Director of the MMTO during the interval of this work, was a strong supporter of and contributor to the development of the MMT for use in speckle interferometry, being the co-developer of the current scheme for coherent cophasing of the telescope and developer of the scheme and instrumentation for differential speckle interferometry.

(ii) D.W.McCarthy, for contributions to the coherent beamcombiner engineering and development.

(ii) W.J.Cocke, for major contributions to the development and implementation of image reconstruction techniques.

(iii) J.D.Drummond, for turning speckle interferometric measurements into interpreted scientific results (asteroid program).

(iv) Graduate students J.Christou, J.Freeman, and A.Cheng, for major contributions to the development and implementation of data reductions algorithms and for theoretical investigations.

(v) Undergraduate students S.Shaklan, A.Szumilo, W.Wisniewski and I.Singer for computer programming, instrument development, assistance with observations and especially with the laborious grunge work of data reductions.

(vi) R.Macklin and J.Rill, for implementation and maintenance of the Grinnell-based video event detector and for general improvements to the Grinnell analog digitizer.

(vii) A.Koski and the computer support group for "solving all the really tough problems".

(viii) D.Young, for mechanical design and unfailing support and assistance in fabrication of instrumentation.

(ix) D.Mitchell, and the technical support group and telescope operators for invaluable assistance.

9. REFERENCES

Angel, J.R.P. (1983) SPIE Proceedings 383, 52.

Bagnuolo, W.G. (1982) Mon. Not. R. Astron. Soc. 200, 1113.

Bagnuolo, W.G. (1983) IAU Colloquium 62, Lowell Observatory Bulletin 9,181.

Bagnuolo, W.G. (1984) Optics Lett. 9,65.

Barletti,R., G. Cepatelli, L. Paterno, A. Richini, N. Speroni (1976) J. Opt. Soc. Am. 66, 1380.

Bates, R.H.T., and F.M. Cady (1980) Opt. Commun. 32, 365.

Bates, R.H.T., and W.R. Fright (1983) J. Opt. Soc. Am. 73, 358.

Beckers, J.M. (1982a) Optica Acta 29, 361.

Beckers, J.M., F. Roddier, and C. Roddier (1982b) MMTO Observers'Report, May 1982.

Beckers, J.M. (1982c) MMTO Technical Memorandum 82-9, 82-14.

Beckers, J.M., and J.T. Williams (1982d) SPIE Proceedings 332, 16.

Beckers, J.M., E.K. Hege and H.P. Murphy (1983a) SPIE Proceedings 445, 462.

Beckers, J.M., E.K. Hege, F.J. Low, D.W. McCarthy and P.A. Strittmatter (1983b) SPIE Proceedings 440, 136.

Beckers, J.M., E.K. Hege and P.A. Strittmatter (1983c) SPIE Proceedings 444, 85.

Christou, J. (1983) (Unpublished communication)

Cocke, W.J. (1980) SPIE Proceedings 231, 99.

Cocke, W.J. (1983) Optics Lett. (Submitted)

Cromwell, R.H., H.W. Funk, K. Frank, P.A. Strittmatter, R.G. Allen, E.K. Hege, and H. Kuhr, (1983) Eighth Symposium on Photoelectronic Image Devices, London, September 1983.

Dainty, J.C. and A.H. Greenaway (1979) J. Opt. Soc. Am. 69, 786.

Davis, J. (1983) NZ J. Science 22, 451.

Drummond, J.D., W.J. Cocke, E.K. Hege, P.A. Strittmatter and J.V. Lambert (1984) Icarus (Submitted)

Fienup, J.R. (1978) Optics Lett. 3, 27.

Fienup, J.R. (1979) Opt. Enging. 18, 529.

Firmani, C., L. Gutierrez, E. Ruiz, G.F.Bisiacchi and L. Salas (1983) SPIE Proceedings 445, 192.

Forbes, F.F., and N.J. Woolf (1983) SPIE Proceedings 444, 175.

Freeman, J.D., (1984) (Unpublished communication)

Goldberg, L., E.K.Hege, E.N. Hubbard, P.A. Strittmatter, and W.J. Cocke (1982) SAO Special Reports 392, 131.

Hege, E.K., E.N. Hubbard, and P.A. Strittmatter (1980) SPIE Proceedings 264, 29.

Hege, E.K., E.N. Hubbard, P.A. Strittmatter, and S.P. Worden (1981) Astrophys. J. (Lett.) 248, L1.

Hege, E.K., E.N. Hubbard, P.A. Strittmatter, and W.J. Cocke (1982a) Optica Acta 29, 70.

Hege, E.K., E. N. Hubbard, J.D. Drummond, P.A. Strittmatter, S.P. Worden, and T. Lauer (1982b) Icarus 50, 72.

Hege, E.K., W.J. Cocke, P.A. Strittmatter, S.P. Worden, and W.C. Booth (1983) SPIE Proceedings 445, 469.

Hubbard, G., E.K. Hege, M. Reed, P.A. Strittmatter, and N. Woolf (1979) Astron. J. 84,1437.

Hunt, B.R., W.R. Fright and R.H.T. Bates (1982) J. Opt. Soc. Am. 73, 456.

Jefferys, W.H. (1980) Astron. J. 85, 177.
" " (1981) Astron. J. 86, 144.

Knox, K.T., and B.J. Thompson (1974) Astrophys. J. (Lett.) 193, L45.

Labeyrie, A. (1970) Astron. and Astrophys. 6, 85.

Labeyrie, A. (1972) Auxilliary Instrumentation for Large Telescopes, ESO/CERN, May 1972.

Labeyrie, A. (1977) Opcital Telescopes of the Future, ESO/CERN.

Labeyrie, A. (1978) Ann. Rev. Astron. Astrophys. 16, 77.

Lena, P., (1982) Second ESO IR Workshop, Garching, 1982.

Low, F.J. (1980) Optical and IR Telescopes for the 1990's, KPNO, p825.

Lynds, C.R., S.P. Worden and J.W. Harvey (1976) Astrophys. J. 207, 174.

Macklin, R.H., E.K. Hege and P.A. Strittmatter (1982) SPIE Proceedings 359, 135.

Mariotti, J.M., A. Chelli, R. Foy, P. Lena, F. Sibille, and G. Tchountonov (1983) Astron. Astrophys. 120, 237.

McAlister, H.A. (1981) Astron. J. 86, 795.

McCarthy, D.W. Proceedings of IAU Colloquium 76.
" " (1982a) Astrophys. J. (Lett.) 257, L7, L75, L93.

McCarthy, D.W., P.A. Strittmatter, E.K. Hege, and F.J. Low (1982b) SPIE Proceedings 332, 57.

Meinel, A.B., M.P. Meinel and N.J. Woolf (1983) SPIE Proceedings 383, 2.

Nisenson, P., R. Statchnik, C. Papaliolios, and P. Horowitz (1980) SPIE Proceedings 243, 88.

Nisenson, P., and C. Papaliolios (1983a) Opt. Commun. 47, 91.

Nisenson, P., J. Apt, R. Goody, and C. Papaliolios (1983b) Icarus 53, 465.

Papaliolios, C. and L. Mertz (1982) SPIE Proceedings 331, 360.

Shaklan, S.B., E.K. Hege and J.M. Beckers (1983) MMTO Technical Memorandum 83-15.

Traub, W., and H. Gurskey (1980) Optical and IR Telescopes for the 1990's, KPNO, p280.

Ulich, B.L., C.J. Lada, N.R. Erickson, P.F. Goldsmith, and G.R. Huguenin (1982) SPIE Proceedings 332, 72.

Walker, J.G. (1982) Appl. Opt. 21, 3132.

Weigelt, G.P. (1978) Appl Opt. 17, 2660.

Welter, G.L. and S.P. Worden (1978) J. Opt. Soc. Am. 68, 1271.

Welter, G.L. and S.P. Worden (1980) Astrophys. J. 242, 673.

Woolf, N.J., D.W. McCarthy ad J.R.P. Angel (1982) SPIE Proceedings 332, 57.

Woolf, N.J., J.R.P. Angel, and D.W. McCarthy (1983a) SPIE Proceedings 444, 78.

Woolf, N.J. and B.L. Ulich (1983b) ESO Workshop on Site Selection for Very Large Telescopes, November, 1983.

Woolf, N.J. and B.L. Ulich (1983c) SPIE Proceedings 383, 11.

10. LIST OF PUBLICATIONS

In this section we list the titles, authors, publications and abstracts of work partially supported by and directly relating to this AFGL contract work.

A REAL-TIME PHOTOELECTRON EVENT-DETECTING VIDEO SYSTEM

R.H. Macklin, E.K. Hege and P.A. Strittmatter
SPIE Proceedings 359, 135 (1982)

We describe a system for localization of photoelectron events utilizing an intensified Plumbicon camera and a Grinnell video digitizer. The Grinnell digitizer, arithmetic unit and memory are used to produce a real-time video difference between current pixel value and previous pixel value thereby suppressing multiple detection of the same event. A master clock provides synchronization with the camera in operation at 60Hz in 240 lines/field, repeat field mode. Our event-localization scheme provides double-buffered line-address and event-amplitude for up to 32 events along a 512 pixel video line. A software algorithm allows localization of multiple detections of the same event, and provides a unique address interpolated with 1/2 line resolution by the host minicomputer in a 480 x 512 format.

COMBINING THE SIX MMT BEAMS COHERENTLY WITH MINIMUM EFFORT

J.M. Beckers and E.K. Hege
MMTO Technical Memorandum 82-10 (1982)

A coherent, phased focus can be achieved with tilted focal planes if the tilt angle is chosen so that the internal phase differences exactly compensate the external phase differences. This amounts to a slight change in configuration such that the beams are brought together at f/8.39 rather than the present f/9.

THE USE OF THE MULTIPLE MIRROR TELESCOPE AS A PHASED ARRAY

J.M. Beckers, E.K. Hege, F.J. Low, D.W. McCarthy, and P.A. Strittmatter
SPIE Proceedings 440, 136 (1983)

We summarize the experiments which have used the Multiple Mirror Telescope (MMT) sub-apertures as a phased array in the optical, infrared, and sub-millimeter spectrum regions. Those experiments exploit the unique, very high angular resolution of the MMT being equivalent to that of a conventional telescope 686cm in diameter. The operation of the MMT as a phased array is not only important for obtaining high angular resolution, but also for obtaining the higher detection sensitivity which results from the better discrimination against the sky emission

background for infrared diffraction limited images. We describe future plans to make the MMT into a phased telescope.

OPTICAL INTERFEROMETRY WITH THE MMT

J.M. Beckers and E.K. Hege
SPIE Proceedings 444, 85 (1983)

By adjustment of the optical pathlengths of the MMT telescopes, it is possible to make the MMT into a phased array with a 686cm baseline. We will describe experiments in speckle interferometry and spectroscopy which have been done this way unsing 2 and 3 of the MMT telescopes. We will describe planned adjustments of the optical configuration of the MMT to achieve coherent operation over a large field of view with all six telescopes phased simultaeously.

THE DIFFERENTIAL SPECKLE INTERFEROMETER

J.M. Beckers, E.K. Hege and H.P. Murphy
SPIE Proceedings 445 462 (1983)

We describe a new technique called "Differential Speckle Interferometry" (DSI) which uses simultaneous narrow band images of astronomical objects to study their structure. Simultaneous specklegrams of red supergiant and giant stars taken in the hydrogen lines and in the nearby continuum allow us to reconstruct the image of the extended chromospheres of these stars at resolutions of 100 nanoradians and better. We describe the instrumentation, analysis techniques, and results related to DSI.

HIGH-SPEED DIGITIAL SIGNAL PROCESSING FOR SPECKLE INTERFEROMETRY

E.K. Hege, W.J. Cocke, P.A. Strittmatter, S.P. Worden and W.C. Booth
SPIE Proceedings 445, 469 (1983)

Speckle Interferometry has now been shown capable of yielding diffraction limited information on objects as faint as visual magnitude 16. Research in progress at Steward Observatory is aimed at improving (a) the resolution, (by using the Multiple Mirror Telescope with its 6.9 meter baseline), (b) the accuracy of the derived results (by implementing better recording devices and reduction algorithms), and (c) the efficiency and speed with which the information can be provided (by means of high-speed digital signal-processing hardware).

CAUCHY'S INEQUALITY IN IMAGE RECONSTRUCTAION AND POWER SPECTRUM ANALYSIS

W. J. Cocke
Optics Lett. (Submitted) (1983)

Cauchy's inequality is applied to image reconstruction and power spectrum analysis in the case where the image or autocorrelation in question is assumed to be non-negative. The inequality is a restriction on the Fourier transform and is shown to be a useful diagnostic in phaseless multidimensional image reconstruction and power spectrum analysis.

RESEARCH AT THE UNIVERSITY OF ARIZONA IN LARGE OPTIC FABRICATION AND THE PHASING AND TRACKING OF LARGE MULTI-ELEMENT OPTICAL SYSTEMS

J.R.P. Angel, E.K. Hege, F.A. Strittmatter, and R. Parks
A Report Prepared for the Defense Technologies Study Team (1983)

The University of Arizona has a strong and practical interest in large and multi-element optical systems. Our multiple-mirror telescope, shared with the Smithsonian Astrophysical Observatory, is the first large scale realization of such a device, with six 1.8m mirrors operated together coherently or as an interferometer. The success of this instrument has stimlated our development of technology for much larger successors. While our motivaion is to make large telescopes for astronomy, the research and technology we are developing is highly relevant to problems of surveillance, acquisition and tracking, and to directed energy.

FRINGE CONTRAST MEASUREMENTS FOR TELESCOPE PHASING

S.B. Shaklan, E.K. Hege and J.M. Beckers
MMTO Technical Memorandum 83-15 (1983)

We demonstrate here the capability of measuring the contrast and position of interferometric fringes produced by two phased mirrors of the MMT. The goal of this experiment was to give a preliminary indication of whether or not an automatic mirror phasing system using one of the MMT Point-4 computers would be feasible. We conclude that 10 seconds is sufficient time for phasing a given pair of mirrors (hence, about 1 minute to phase the entire telescope) using stars up to 6th magnitude given a modest hardware FFT device.

SPECKLE INTERFEROMETRY OF ASTEROIDS. I. 433 EROS

J.D. Drummond, W.J. Cokce, E.K. Hege, P.A. Strittmatter and J.V. Lambert
Icarus (Submitted) (1984)

We derive analytic expressions for the semimajor and semiminor axes and an orientation angle of the ellipse projected by a triaxial ellipsoid (an asteroid) and of the ellipse segment cast by a terminator across the ellipsoid as functions of the dimensions and pole of the body and the asterocenteric position of the Earth and Sun. Applying these formulae to observations of the Earth-approaching asteroid 433 Eros obtained with the speckle interferometry system of Steward Observatory on December 17,18 1981 and January 17,18 1982, we derived the following dimensions: (42 ± 2.6 km) x (15.5 ± 2.0 km) x (14.0 ± 2.4 km). We find Eros' north pole to lie within 9° of RA = 359°, Dec = +45° (ecliptic longitude 21°, latitude +41°). Other than knowing the rotation period of Eros, these results are completely independent of any other data, and in the main confirm the results obtained in the 1974-75 apparition by other methods. Our dimensions, together with a lightcurve from December 18, 1981, lead to a geometric albedo of 0.14 ± .02. We include a series of two-dimensional power spectra and autocorrelation functions for the resolved asteroid that clearly shows it spinning in space.

GONE WITH THE WIND, OR SAILING AND SEEING WITH A GIANT TELESCOPE

N.J. Woolf and B.L. Ulich
ESO Workshop on Site Selection for Very Large Telescopes (1983)

Both anecdotal and quantitative information on seeing and wind shake at the MMT are used to discuss the problem of site selection for a giant telescope. An adequately isolated mountain peak is defined, and such peaks are not rare. It is shown that at such a peak, the site contribution to seeing will, in general, be much less than the contribution of the remainder of the atmosphere. In contrast, the typical seeing at a large observatory is usually dominated by the contribution of the facility. Because seeing is mainly a problem of facility design, site selection criteria can strongly weight the major problem of wind shake. Wind oscillatory torques are a major problem for a facility designed for excellent seeing. These torques increase with the square of wind speed. It is not yet clear how the responsibility for these torques should be apportioned between the site and the facility. Extreme care in all relevant factors, but particularly in site selection, will be needed to ensure that excellent telescope images are not spoiled by wind shake.

THE VERSATILE ARRAY

N.J. Woolf, J.R.P. Angel and D.W. McCarthy
SPIE Proceedings 444, 78 (1983)

We discuss a four element non-degenerate array telescope-interferometer for ground use. The elements are 8 meter mirrors, and the maximum array spacing and two element spacing are 75m and 108m respectively. The array may be used as three separate telescopes, one 11.3m and two 8m for work not requiring highest angular resolution. We discuss the problems of making speckle measures to high enough precision for synthetic images to be produced. We conclude by showing that the high resolution presents opportunities to make types of observations that are neither possible with VLBA nor NNTT.

ALIGNMENT AND PHASING OF DEPLOYABLE TELESCOPES

N.J. Woolf and B.L. Ulich
SPIE Proceedings 383, 11 (1983)

We describe the experiences in coaligning and phasing the MMT, together with studies in setting up radio telescopes. We discuss these experiences and on the basis of them, we suggest schemes for coaligning and phasing four large future telescopes with complex primary mirror systems. These telescopes are MT2, a 15m equivalent MMT, The University of California Ten Meter Telescope, the 10m sub-mm wave telescope of the University of Arizona and the Max Planck Institute for Radioastronomy, and the Large Deployable Reflector, a future space telescope for far IR and sub-mm waves.

DEPLOYABLE REFLECTOR CONFIGURATIONS

A.B. Meinel, M.P. Meinel and N.J. Woolf
SPIE Proceedings 383, 2 (1983)

We discuss both the theoretical reasons for considering a non-circular format for the Large Deployable Reflector, and a potentially realizable concept for such a device. The optimum systems for diffraction limited telescopes with incoherent detection have either a single filled aperture, or two such apertures as an interferometer to systhesize a larger aperture. For a single aperture of limited area, a reflector in the form of a slot can be used to give increased angular resolution. We show how a 20 x 8 meter telescope can be configured to fit the space shuttle bay, and deployed with relatively simple operations. We discuss the relationship between the sunshield design and the inclination of the orbit. We conclude by discussing the possible use of the LDR as a basic module to permit the construction of supergiant space telescopes and interferometers both for IR/submm studies and for the entire untraviolet through mm wave spectral region.